On the application of the FENE-L and FENE-LS closure approximations to turbulence in dilute polymer solutions.

Auteur : Goffin, Pierre-Yves
Promoteur(s) : Terrapon, Vincent
Faculté : Faculté des Sciences appliquées
Diplôme : Master en ingénieur civil physicien, à finalité approfondie
Année académique : 2022-2023
URI/URL : http://hdl.handle.net/2268.2/17858

UNIVERSITY OF LIÈGE
FACULTY OF APPLIED SCIENCES

On the application of the FENE-L and FENE-LS closure approximations to turbulence in dilute polymer solutions.

Master's thesis conducted in order to obtain the
Master degree in Physics Engineering,
by Pierre–Yves GOFFIN.

ACADEMIC YEAR 2022–2023

Advisor
Vincent E. TERRAPON

Abstract

Numerical simulations of dilute polymer solutions are considered through the FENE constitutive model. More advanced closure approximations than the well-known FENE-P model are investigated in order to close the polymer stress term: the FENE-L and the FENE-LS. From an in-depth study of the properties of such closures, better suited variations are proposed. The center-of-mass diffusion term is added to the Fokker-Planck equation and the corresponding term in the polymers equations is derived as it may be useful for solving the Eulerian problem. It however seems to brings complexity in this case and a modified diffusion term is proposed to overcome such problems, but has not already been tested in practice. Finally, an Eulerian Newtonian turbulent channel at $\mathrm{Re}_\tau \approx 300$ is simulated and the history of the velocity gradients experienced by 100 tracked particles are recorded. The passive response of the polymers is then computed and the different constitutive models are compared. The most significant differences between the FENE-P and the more complex models appear in regions where the dumbbells are suddenly stretched after having been in their coiled configuration for a sufficient amount of time. These differences thus occur in highly transient flows.

Contents

Introduction

Dilute polymer solutions are known for their interesting viscoelastic properties. Among other things, the addition of polymers to a Newtonian solvent can have strong and surprising effects on the flow turbulent behavior, even for fairly small polymer concentrations (of the order of a few ppm). In particular, a significant interest has been shown for the effects of Elastic Turbulence (ET), Elasto-Inertial Turbulence (EIT) and Drag Reduction (DR) or even Maximum Drag Reduction (MDR) during the last decades. In fact, such phenomena are very interesting and still not yet fully understood as the polymers seem to have antagonist effects on the flow properties depending on its turbulent regime: it can trigger and enhance the chaotic motion of initially laminar flows on the one hand (EIT) and it can damp the fluctuations of more turbulent flows on the other hand (DR). The specific case of MDR, constituting a fundamental limit of the DR, is also still an interesting open question as the mechanism of this limit is not yet understood, even though several theories exist to explain the phenomenon.

In order to gain a better comprehension of the different dynamics of the physical problem, numerical simulations can be a useful tool as they offer a wider access to the data of the flow considered, compared to experimental studies. As always, the difficulty is however to derive meaningful models that accurately describe the interesting physics and that can be simulated in reasonable amount of time, whereas experiments benefit from the exact physical behavior of the system but suffer from the often poor data accessibility, sometimes necessary to understand the intrinsic mechanisms of the problem.

Since the impact of each single polymer on the fluid cannot reasonably be considered numerically, it is important to rely on the theories of continuum mechanics and micro-rheology to derive macroscopic constitutive models that take into account the microscopic effect of the polymer molecules on the surrounding fluid. Such effect is taken into account in practice through an extra stress term added to the classical Newtonian stress.

However, in order to derive such term, it is necessary to have access to the expression of the impact of a polymer molecule on the fluid. But again, this would be unfeasible to derive the analytical expression of such influence for a general real polymer according to the complexity of such molecule. Several conceptual levels of approximation can thus be introduced in order to simply the description of a polymer and derive analytical expressions of the forces it exerts on the fluid. The most widely used approximation is the dumbbell model, which describes a polymer chain as two massive beads interacting with the flow through hydrodynamic drag and Brownian forces and connected between each other by a spring of given rigidity. The dumbbell model combined with a specific

non-linear spring law yields the well known FENE (Finitely Extensible Non-linear Elastic) model. The difficulty of such a model lies is the fact that the system of equations that can be obtained is not closed. One of the methods to overcome this problem is to try to close the system by introducing closure approximations. The most widely used closure rely on the well-known Peterlin approximation yielding the FENE-P constitutive model for the polymer stress, but such approximation is quite crude from a physical and statistical point of view. The similarity between the results of the FENE-P and higher fidelity results (of the general FENE model) are thus limited to some specific configurations: mainly steady flows and high polymer extensions.

The motivation is thus to be able to yield more accurate results (than the FENE-P) in more realistic flow configurations that are similar to the EIT or DR regimes, by investigating more advanced and physically meaningful closure approximations. The models that are considered here for that purpose have originally been derived by Lielens *et al.* [6, 7].

The present work starts by deriving the classical FENE dynamics in Chap. 1. The more advanced closure approximations are then presented in Chap. 2 and an in-depth analysis is performed to better understand some of their inherent limitations in Chap. 3. Chapter 4 focuses on the comprehension of a specific problem occurring when center-of-mass diffusion of the polymers is considered. Finally, an application of the models to a turbulent channel flow is performed in Chap. 5.

Chapter 1

Polymer modeling

The contribution of the polymers on the solvent are modeled through an additional term in the expression of the stress. More precisely, the stress of the fluid writes

$$\hat{\sigma}_{ij} = -\hat{p}\delta_{ij} + 2\mu\hat{E}_{ij} + \hat{\tau}_{ij}^{\mathrm{p}}, \tag{1.0.1}$$

where $\hat{p}$ is the pressure, μ the dynamic viscosity of the Newtonian solvent, $\hat{\boldsymbol{E}}$ is the strain rate tensor and $\hat{\boldsymbol{\tau}}^{\mathrm{p}}$ the polymer stress tensor. The momentum equation of the fluid then writes

$$\frac{\partial \hat{u}_i}{\partial \hat{t}} + \hat{u}_j \frac{\partial \hat{u}_i}{\partial \hat{x}_j} = -\frac{1}{\rho}\frac{\partial \hat{p}}{\partial \hat{x}_i} + \nu \frac{\partial^2 \hat{u}_i}{\partial \hat{x}_j \partial \hat{x}_j} + \frac{1}{\rho}\frac{\partial \hat{\tau}_{ij}^{\mathrm{p}}}{\partial \hat{x}_j}, \tag{1.0.2}$$

where ν is the kinematic viscosity of the solvent. Since incompressible fluid flows are considered here, the momentum equation should be complemented by the continuity equation:

$$\frac{\partial \hat{u}_i}{\partial \hat{x}_i} = 0. \tag{1.0.3}$$

Note that in the following of this work, when confusion is possible, the notation $\hat{\cdot}$ refers to dimensional quantities.

In order to compute the polymer stress tensor and be able to solve the fluid equations, it is necessary to have access to the elementary forces that the polymers exert on the solvent. Such information is however only accessible on average as one cannot take into account each and every molecule in the solution. Still, it is required to have access to the different polymer forces that come into play. Unfortunately, polymers are characterized as very long flexible molecules composed of many monomers and it is therefore not realistic to take into account the precise effect of all the molecule. Different conceptual levels of approximations exist for describing the polymer dynamics.

1.1 Freely jointed chain

First, note that the focus is here on long flexible linear polymers only. The first approximation is to consider each monomer as a rigid rod and that the joints that attach the monomers between each other are perfectly flexible. This is called the freely jointed chain model. The hypothesis on the perfectly flexible joints is however not valid in

practice. In fact, the angles between two joints cannot take any value in reality as these are not perfectly flexible and also because the polymers need to avoid self interaction (e.g. the joint cannot have an angle of 180° as it means that the monomers would be superposed on each other). This can nonetheless be accommodated by considering a greater polymer size than it is in reality, since the angle restrictions lead to more extended chains.

Considering a polymer molecule at equilibrium, all the bonds are agitated by the Brownian forces, such that the polymer configuration is constantly evolving. One can still define a time-averaged mean-square distance $\langle \hat{Q}^2 \rangle_0$ between the two very ends of the chain. It is then possible to introduce the Kuhn step size b_K and the number of Kuhn steps in the chain N_K such that

$$\langle \hat{Q}^2 \rangle_0 = N_\mathrm{K} b_\mathrm{K}^2. \tag{1.1.1}$$

Finally, note that even if the joints are not perfectly flexible in practice, the influence of the orientation of two rods (between each other) decreases exponentially as the number of rods that separate them increases. As an approximation, one can thus consider each rod as a random step, in the sense that two steps are independent of each other (not valid in practice between two adjacent rods, but becomes overall satisfying as the length of the chain increases).

1.1.1 Random walks

At equilibrium, neglecting the excluded volume effect, one can start from one end of the polymer and progressively build up the hole chain by adding N_K successive random walks of step size b_K. Since the N_K random walks are considered uncorrelated between each other, if the number of rods is sufficiently large, the sum of the random walks (each of them being a three-dimensional vector) can be considered as a normal random variable. In fact, considering the connector or end-to-end vector $\hat{\boldsymbol{Q}}$ with norm $\hat{Q}$ that connects both ends of the chain, if one end is fixed at the origin, the probability that the other end lies between $\hat{\boldsymbol{Q}}$ and $\hat{\boldsymbol{Q}} + d\hat{\boldsymbol{Q}}$ is $\hat{\psi}_0(\hat{\boldsymbol{Q}})\mathrm{d}\hat{\boldsymbol{Q}}$, where $\hat{\psi}_0$ is called the equilibrium configurational probability distribution and follows a Gaussian distribution:

$$\hat{\psi}_0(\hat{\boldsymbol{Q}}) = \left(\frac{1}{\sqrt{2\pi}\sigma} \right)^3 e^{-\frac{\hat{Q}^2}{2\sigma^2}}, \tag{1.1.2}$$

where σ^2 is the general variance of the distribution.

Note that this expression does not prevent any end-to-end polymer extension. In fact, any positive $\hat{Q}$ is associated with a non-vanishing probability density distribution. The polymer cannot however extents to an infinite length in practice and one then understands that the expression of $\hat{\psi}_0$ is not valid anymore for too large $\hat{Q}$.

Considering that the polymer end-to-end vector follows $\hat{\psi}_0$, it is possible to relate σ^2 to $\langle \hat{Q}^2 \rangle_0$ (from Eq. 1.1.1) through the expression of the equilibrium probability density distribution:

$$\langle \hat{Q}^2 \rangle_0 = \int \hat{Q}^2 \hat{\psi}_0(\hat{\boldsymbol{Q}})\mathrm{d}\hat{\boldsymbol{Q}} = 3\sigma^2 = N_\mathrm{K} b_\mathrm{K}^2. \tag{1.1.3}$$

However, in the literature one rather considers β^2, such that $\beta^2 \equiv 1/(2\sigma^2)$ and it yields

$$\left\langle \hat{Q}^2 \right\rangle_0 = N_K b_K^2 = \frac{3}{2} \frac{1}{\beta^2}. \tag{1.1.4}$$

1.1.2   Entropic spring force

Considering now that the polymeric chain is stretched to a prescribed and fixed end-to-end vector $\hat{Q}$, the likelihood of that configuration can be accessed through $\hat{\psi}_0$. According to the theory of statistical mechanics, the fact that a configuration is more probable than another is directly linked to the number of microstates of each macrostate[1]. In this case, the microstates are the precise orientation of each of the monomers and the macrostate is the end-to-end vector. One knows that the number of microstates, noted Ω, is directly proportional to the probability density distribution of $\hat{Q}$, such that $\Omega(\hat{Q}) = c\hat{\psi}_0(\hat{Q})$, with c a proportionality constant. From the statistical definition of entropy S, the entropy of any macrostate writes

$$S = k_B \ln \Omega = k_B \ln \left(c\hat{\psi}_0 \right) = k_B \left(\ln c + 3 \ln \left(\frac{\beta}{\sqrt{\pi}} \right) - \beta^2 \hat{Q}^2 \right), \tag{1.1.5}$$

with k_B the Boltzmann constant.

If the enthalpy of the chain does not depend on its configuration, its free energy W becomes $W = -TS$, with T the absolute temperature. The work needed to stretch the chain from $\hat{Q}$ to $\hat{Q} + d\hat{Q}$ is then

$$\begin{aligned}
\hat{\mathcal{F}}_i^{\text{sp}} d\hat{Q}_i &= \frac{\partial W}{\partial \hat{Q}_i} d\hat{Q}_i = -T \frac{\partial S}{\partial \hat{Q}_i} d\hat{Q}_i = k_B T \beta^2 \frac{\partial \hat{Q}^2}{\partial \hat{Q}_i} d\hat{Q}_i = 2k_B T \beta^2 \hat{Q} \frac{\partial \hat{Q}}{\partial \hat{Q}_i} d\hat{Q}_i \\
&= 2k_B T \beta^2 \hat{Q} \frac{\hat{Q}_i}{\hat{Q}} d\hat{Q}_i = 2k_B T \beta^2 \hat{Q}_i d\hat{Q}_i,
\end{aligned} \tag{1.1.6}$$

where $\hat{\mathcal{F}}^{\text{sp}} = 2k_B T \beta^2 \hat{Q}$ is the force needed to stretch the chain. Alternatively, the restoring force of the chain is $\hat{F}^{\text{sp}} = -2k_B T \beta^2 \hat{Q}$. Using Eq. 1.1.4:

$$\hat{F}^{\text{sp}} = -2k_B T \beta^2 \hat{Q} = -\frac{3k_B T}{N_K b_K^2} \hat{Q} = -\hat{H}\hat{Q}, \tag{1.1.7}$$

with $\hat{H} \equiv 2k_B T \beta^2 = (3k_B T)/(N_K b_K^2)$, the spring constant.

This interesting result points out the fact that a polymer chain at equilibrium behaves as a linear (or Hookean) spring as $\hat{H}$ does not depend on the end-to-end vector. Note that the expression of the restoring force does not prevent the polymer to extend beyond any maximal extension. This is in accordance with what was already noted for Eq. 1.1.2. One can thus anticipate the fact that this kind of linear force will only be valid for small polymer extensions.

---

[1]The macrostate denotes the macroscopic configuration (the end-to-end vector $\hat{Q}$ in this case) and the microstate denotes the microscopic configuration (the precise orientation of each random step in this case). In fact, several microstates are possible for obtaining a single macrostate (here several combinations of rods orientation can lead to the same end-to-end vector $\hat{Q}$).
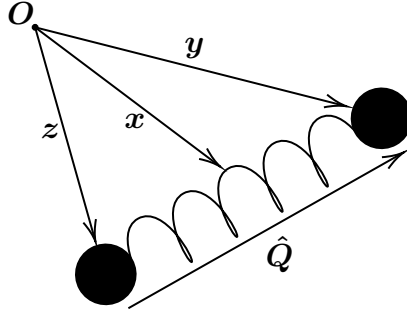
Figure 1.2.1: Schematic of a dumbbell.

1.2 Coarse graining

The entropic spring force discussed in the previous section is a polymer property in the sense that it only depends on the nature of the polymer. The goal is now to analyze the impact of the flow on these chains. Neglecting the interactions between the polymers themselves, one can consider two main contributions of the flow on the polymer dynamics: the Brownian forces exerted by the fluid particles on the polymers (this comes from the internal energy of the fluid) and the drag force of the flow which makes the polymers follow the flow, stretch and rotate with it. One will thus have to consider the impact of these different forces on the polymers in addition to the restoring entropic force.

Starting from the exact flexible linear polymer, different conceptual levels of idealization are possible, starting with the already mentioned freely jointed chain. However, it would be impossible to account for the flow forces at each of the joints of the hole chain. The first idea is then to split the freely jointed chain in N segments that are attached at each other by the ends. Each segment i of the chain can be modeled by a spring of extension $\hat{Q}_i$ and the effect of the flow is considered at the ends of the spring. In such a configuration, the Brownian and drag forces are only taken into account at $N + 1$ specific points, called the beads. This approximation is called the bead-spring chain model. Finally, the coarser model is called the dumbbell model. It assumes that the freely jointed chain behaves as a spring and that the applied forces are only taken into account at the spring ends. It is equivalent to the bead-spring chain model with $N = 1$. A schematic of the dumbbell representation is shown in Fig. 1.2.1. Note that in these models (bead-spring chain and dumbbell), the mass of the polymer is assumed to be concentrated at the beads and the springs are assumed massless. Finally note that only the dumbbell model will be considered in the following.

1.2.1 Dumbbell dynamics

Defining the position vectors $\hat{y}$ and $\hat{z}$ of each of the dumbbell beads as in Fig. 1.2.1, one can define the position of the center of mass $\hat{x}$. Since the dumbbell only possesses two massive beads, the center of mass corresponds to the geometric center, such that

$$\hat{x} = \frac{\hat{y} + \hat{z}}{2}. \tag{1.2.1}$$

Figure 1.2.2: Forces acting on each bead, with $\hat{\boldsymbol{F}}^{\mathrm{d}}$ the drag force, $\hat{\boldsymbol{F}}^{\mathrm{B}}$ the Brownian force and $\hat{\boldsymbol{F}}^{\mathrm{sp}}$ the spring force.

Finally, the end-to-end or connector vector $\hat{\boldsymbol{Q}}$ is related to the bead position vectors:

$$\hat{\boldsymbol{Q}} = \hat{\boldsymbol{y}} - \hat{\boldsymbol{z}}. \tag{1.2.2}$$

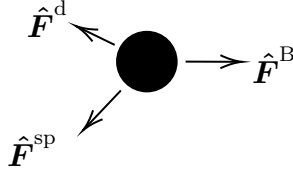The configuration of a dumbbell is then fully defined by either the position of its two beads or the position of its center of mass and its connector vector. One can thus associate a probability density to each configuration and define the total probability density distribution $\hat{\Psi} = \hat{\Psi}(\hat{\boldsymbol{x}}, \hat{\boldsymbol{Q}}, \hat{t})$.

In order to understand the motion of the bead, one has to do a force balance. The different forces applied on the beads are schematized in Fig. 1.2.2. For a bead located at $\hat{\boldsymbol{y}}$ their expressions are (it can also be derived for a bead located at $\hat{\boldsymbol{z}}$)

$$\begin{cases} \hat{\boldsymbol{F}}^{\mathrm{d}} = \zeta \left(\boldsymbol{u}^{\infty}(\hat{\boldsymbol{y}}) - \dfrac{\mathrm{d}\hat{\boldsymbol{y}}}{\mathrm{d}\hat{t}} \right), \\[2mm] \hat{\boldsymbol{F}}^{\mathrm{B}} = -k_{\mathrm{B}} T \boldsymbol{\nabla}_{\hat{\boldsymbol{x}}} \ln \hat{\Psi}, \\[2mm] \hat{\boldsymbol{F}}^{\mathrm{sp}} = -\hat{H}(\hat{Q}) \hat{\boldsymbol{Q}} = -\hat{H} \mathcal{H}(\hat{Q}) \hat{\boldsymbol{Q}}, \end{cases} \tag{1.2.3}$$

with ζ the drag coefficient of the bead and $\boldsymbol{u}^{\infty}$ the freestream velocity of the flow[2]. In order to stay general, the spring constant is expressed as a function of the dumbbell end-to-end distance. Indeed, as was anticipated in Sec. 1.1.2, this linear force will only be valid for small polymer extensions, such that a more sophisticated spring force will have to be considered at some point. Note that $\hat{H}(\hat{Q})$ is decomposed into a constant dimensional part $\hat{H}$ and a non-dimensional function of the end-to-end distance $\mathcal{H}(\hat{Q})$. One understands that in the simple case of a linear spring force, $\mathcal{H} = 1$.

Eventually, for a bead at position $\hat{\boldsymbol{y}}$ Newton's law writes

$$m \frac{\mathrm{d}^2 \hat{\boldsymbol{y}}}{\mathrm{d}\hat{t}^2} = \hat{\boldsymbol{F}}^{\mathrm{d}} + \hat{\boldsymbol{F}}^{\mathrm{B}} + \hat{\boldsymbol{F}}^{\mathrm{sp}}, \tag{1.2.4}$$

with m the mass of the bead. However, the inertia of the polymers can be considered small with respect to the other terms. This is equivalent to saying that the polymers perfectly follow the flow. The equation of motion then reduces to

$$\hat{\boldsymbol{F}}^{\mathrm{d}} + \hat{\boldsymbol{F}}^{\mathrm{B}} + \hat{\boldsymbol{F}}^{\mathrm{sp}} = 0. \tag{1.2.5}$$

---

[2]Note that hydrodynamic interaction is not taken into account here as the drag force exerted on a bead of a dumbbell is not influenced by the other bead. In more realistic models, additional terms may be considered in the expression of the drag force in order to take such influence into account [8]. Note also that the influence of the other dumbbells are not taken into account as well as they are considered sufficiently far apart from each other. This constitutes the dilute polymer solution assumption.

Using the expressions of the forces and rearranging the terms, it yields.

$$\begin{cases} \dfrac{\mathrm{d}\hat{y}_i}{\mathrm{d}\hat{t}} = u_i^{\infty}(\hat{\boldsymbol{y}}) - \dfrac{k_{\mathrm{B}}T}{\zeta}\dfrac{\partial \ln \hat{\Psi}}{\partial \hat{y}_i} - \dfrac{\hat{H}}{\zeta}\mathcal{H}(\hat{Q})\hat{Q}_i, \\[3mm] \dfrac{\mathrm{d}\hat{z}_i}{\mathrm{d}\hat{t}} = u_i^{\infty}(\hat{\boldsymbol{z}}) - \dfrac{k_{\mathrm{B}}T}{\zeta}\dfrac{\partial \ln \hat{\Psi}}{\partial \hat{z}_i} + \dfrac{\hat{H}}{\zeta}\mathcal{H}(\hat{Q})\hat{Q}_i. \end{cases} \tag{1.2.6}$$

Computing the average of the two above equations and subtracting them gives one equation for the center of mass and one equation for the connector vector[3]:

$$\begin{cases} \dfrac{\mathrm{d}\hat{x}_i}{\mathrm{d}\hat{t}} = \dfrac{u_i^{\infty}(\hat{\boldsymbol{y}}) + u_i^{\infty}(\hat{\boldsymbol{z}})}{2} - \dfrac{k_{\mathrm{B}}T}{2\zeta}\dfrac{\partial \ln \hat{\Psi}}{\partial \hat{x}_i}, \\[3mm] \dfrac{\mathrm{d}\hat{Q}_i}{\mathrm{d}\hat{t}} = (u_i^{\infty}(\hat{\boldsymbol{y}}) - u_i^{\infty}(\hat{\boldsymbol{z}})) - \dfrac{2k_{\mathrm{B}}T}{\zeta}\dfrac{\partial \ln \hat{\Psi}}{\partial \hat{Q}_i} - \dfrac{2\hat{H}}{\zeta}\mathcal{H}(\hat{Q})\hat{Q}_i. \end{cases} \tag{1.2.8}$$

If the polymer characteristic size is small enough compared to the characteristic scale of the flow[4], the flow velocity at the beads may be approximated as a linear variation of the velocity at the center of mass:

$$\begin{cases} u_i^{\infty}(\hat{\boldsymbol{y}}) \approx u_i^{\infty}(\hat{\boldsymbol{x}}) + \dfrac{\hat{Q}_j}{2}\left.\dfrac{\partial u_i^{\infty}}{\partial \hat{x}_j}\right|_{\hat{\boldsymbol{x}}}, \\[3mm] u_i^{\infty}(\hat{\boldsymbol{z}}) \approx u_i^{\infty}(\hat{\boldsymbol{x}}) - \dfrac{\hat{Q}_j}{2}\left.\dfrac{\partial u_i^{\infty}}{\partial \hat{x}_j}\right|_{\hat{\boldsymbol{x}}}. \end{cases} \tag{1.2.9}$$

Injecting this in the previous system yields

$$\begin{cases} \dfrac{\mathrm{d}\hat{x}_i}{\mathrm{d}\hat{t}} = u_i^{\infty}(\hat{\boldsymbol{x}}) - d\dfrac{\partial \ln \hat{\Psi}}{\partial \hat{x}_i}, \\[3mm] \dfrac{\mathrm{d}\hat{Q}_i}{\mathrm{d}\hat{t}} = \hat{Q}_j \underbrace{\left.\dfrac{\partial u_i^{\infty}}{\partial \hat{x}_j}\right|_{\hat{\boldsymbol{x}}}}_{\hat{\dot{\gamma}}_{ij}} - D\dfrac{\partial \ln \hat{\Psi}}{\partial \hat{Q}_i} - \dfrac{1}{2\lambda_{\mathrm{H}}}\mathcal{H}(\hat{Q})\hat{Q}_i, \end{cases} \tag{1.2.10}$$

where d is the center-of-mass diffusivity, $\hat{\dot{\gamma}}$ is the velocity gradient tensor, D is the configurational diffusivity and λ_{H} is the Rouse relaxation time scale[5]. These parameters are thus defined as

$$d \equiv \dfrac{k_{\mathrm{B}}T}{2\zeta}, \quad D \equiv \dfrac{2k_{\mathrm{B}}T}{\zeta}, \quad \lambda_{\mathrm{H}} \equiv \dfrac{\zeta}{4\hat{H}}. \tag{1.2.11}$$

---

[3]Using Eq. 1.2.1–1.2.2 and applying the chain rule, one can show that

$$\begin{cases} \dfrac{\partial}{\partial \hat{y}_i} + \dfrac{\partial}{\partial \hat{z}_i} = \dfrac{\partial}{\partial \hat{x}_i}, \\[3mm] \dfrac{\partial}{\partial \hat{y}_i} - \dfrac{\partial}{\partial \hat{z}_i} = 2\dfrac{\partial}{\partial \hat{Q}_i}. \end{cases} \tag{1.2.7}$$

[4]The validity of this assumption may be questionable in cases where the characteristic scales of the flow are very small and the typical elongation of the polymers are large. This could arise in microchannels or even in highly turbulent flows.

[5]Further analysis shows that in the case of a fluid at rest (polymer relaxation) and considering a linear spring approximation ($\mathcal{H} = 1$), the dumbbells exponentially return toward their equilibrium configuration in a characteristic time λ_{H}.

Considering now the general Fokker-Planck equation for the total probability density distribution

$$\frac{\partial \hat{\Psi}}{\partial \hat{t}} + \frac{\partial}{\partial \hat{x}_i}\left(\frac{\mathrm{d}\hat{x}_i}{\mathrm{d}\hat{t}}\hat{\Psi}\right) + \frac{\partial}{\partial \hat{Q}_i}\left(\frac{\mathrm{d}\hat{Q}_i}{\mathrm{d}\hat{t}}\hat{\Psi}\right) = 0 \qquad (1.2.12)$$

and injecting the results of Eq. 1.2.10, it yields

$$\frac{\partial \hat{\Psi}}{\partial \hat{t}} + \frac{\partial}{\partial \hat{x}_i}\left(u_i^\infty \hat{\Psi}\right) - d\frac{\partial^2 \hat{\Psi}}{\partial \hat{x}_k \partial \hat{x}_k} + \frac{\partial}{\partial \hat{Q}_i}\left(\hat{\dot{\gamma}}_{ij}\hat{Q}_j \hat{\Psi}\right) - D\frac{\partial^2 \hat{\Psi}}{\partial \hat{Q}_k \partial \hat{Q}_k} - \frac{1}{2\lambda_\mathrm{H}}\frac{\partial}{\partial \hat{Q}_i}\left(\mathcal{H}(\hat{Q})\hat{Q}_i \hat{\Psi}\right) = 0$$
$$(1.2.13)$$

and considering an incompressible flow:

$$\frac{\partial \hat{\Psi}}{\partial \hat{t}} + u_i^\infty \frac{\partial \hat{\Psi}}{\partial \hat{x}_i} - d\frac{\partial^2 \hat{\Psi}}{\partial \hat{x}_k \partial \hat{x}_k} + \frac{\partial}{\partial \hat{Q}_i}\left(\hat{\dot{\gamma}}_{ij}\hat{Q}_j \hat{\Psi}\right) - D\frac{\partial^2 \hat{\Psi}}{\partial \hat{Q}_k \partial \hat{Q}_k} - \frac{1}{2\lambda_\mathrm{H}}\frac{\partial}{\partial \hat{Q}_i}\left(\mathcal{H}(\hat{Q})\hat{Q}_i \hat{\Psi}\right) = 0. \quad (1.2.14)$$

The role of the diffusion coefficients that were introduced in Eq. 1.2.10 is now clear. However in practice, the center-of-mass diffusion of polymers is often small and could be neglected. In order to stay general, this term is kept in the following developments. Note also that this term is often kept and even amplified numerically is order to add numerical diffusion to the problem which stabilizes the advective term.

In many cases, the dumbbells density at a specific point and their configurations are unrelated to each other. The total probability density function $\hat{\Psi}$ can then be decoupled between a polymer density $\hat{n}_\mathrm{p}$ and a configurational probability density function $\hat{\psi}$, where the spatial dependency is explicitly taken into account in $\hat{n}_\mathrm{p}$, but is only considered as a parameter in $\hat{\psi}$. It writes

$$\hat{\Psi}(\hat{\boldsymbol{x}}, \hat{\boldsymbol{Q}}; \hat{t}) = \hat{n}_\mathrm{p}(\hat{\boldsymbol{x}}; \hat{t})\hat{\psi}(\hat{\boldsymbol{Q}}; \hat{t}, \hat{\boldsymbol{x}}). \qquad (1.2.15)$$

Moreover, it is common to assume that the density of dumbbells is constant in space, such that

$$\hat{\Psi}(\hat{\boldsymbol{Q}}; \hat{t}, \hat{\boldsymbol{x}}) = \hat{n}_\mathrm{p}\hat{\psi}(\hat{\boldsymbol{Q}}; \hat{t}, \hat{\boldsymbol{x}}). \qquad (1.2.16)$$

Injecting this result in Eq. 1.2.14 gives

$$\frac{\partial \hat{\psi}}{\partial \hat{t}} + u_i^\infty \frac{\partial \hat{\psi}}{\partial \hat{x}_i} + \frac{\partial}{\partial \hat{Q}_i}\left(\hat{\dot{\gamma}}_{ij}\hat{Q}_j \hat{\psi}\right) - d\frac{\partial^2 \hat{\psi}}{\partial \hat{x}_k \partial \hat{x}_k} - D\frac{\partial^2 \hat{\psi}}{\partial \hat{Q}_k \partial \hat{Q}_k} - \frac{1}{2\lambda_\mathrm{H}}\frac{\partial}{\partial \hat{Q}_i}\left(\mathcal{H}(\hat{Q})\hat{Q}_i \hat{\psi}\right) = 0. \quad (1.2.17)$$

For the following developments, it is important to define the configurational average of a quantity. It is noted $\langle \cdot \rangle$ and consists in integrating the product of this quantity with the total probability density distribution $\hat{\Psi}$ on the configuration space noted Ω, which is the space of all admissible connector vectors $\hat{\boldsymbol{Q}}$:

$$\langle \cdot \rangle = \int_\Omega \cdot \; \hat{\Psi}(\hat{\boldsymbol{x}}, \hat{\boldsymbol{Q}}; \hat{t})\,\mathrm{d}\hat{\boldsymbol{Q}} \qquad (1.2.18)$$

and using the homogeneous fluid assumption

$$\langle \cdot \rangle = \hat{n}_\mathrm{p} \int_\Omega \cdot \; \hat{\psi}(\hat{\boldsymbol{Q}}; \hat{t}, \hat{\boldsymbol{x}})\,\mathrm{d}\hat{\boldsymbol{Q}}. \qquad (1.2.19)$$

1.2.2 Extra stress

The dumbbells dynamics affects the flow through the total stress tensor. In fact, the total stress of a dilute solution of non-interacting particles into a Newtonian solvent can be computed as the sum of the classical Newtonian stress and the extra stress, coming from the particles. In this case, the extra stress can be divided into two contributions: the contributions from the Brownian forces and the drag force.

First, it is possible to show that the extra stress coming from the Brownian forces only adds a constant isotropic term (which seems quite logical). More precisely, the contribution of the Brownian forces to the total stress tensor is $-2\hat{n}_{\mathrm{p}}k_{\mathrm{B}}T\delta_{ij}$. Being constant and isotropic, this term is commonly integrated into the pressure term. In fact, since the pressure term is defined within a constant, it can be redefined by taking this term into account.

Then, the extra stress coming from the drag forces takes the form

$$-\frac{\hat{n}_{\mathrm{p}}}{2}\left(\langle\hat{Q}_i\hat{F}_j^{\mathrm{sp}}\rangle + \langle\hat{Q}_j\hat{F}_i^{\mathrm{sp}}\rangle\right) - \hat{n}_{\mathrm{p}}k_{\mathrm{B}}T\delta_{ij}. \tag{1.2.20}$$

Summing all the contributions, the total stress writes

$$\hat{\sigma}_{ij} = -\hat{p}\delta_{ij} - 2\hat{n}_{\mathrm{p}}k_{\mathrm{B}}T\delta_{ij} + 2\mu\hat{E}_{ij} + -\frac{\hat{n}_{\mathrm{p}}}{2}\left(\langle\hat{Q}_i\hat{F}_j^{\mathrm{sp}}\rangle + \langle\hat{Q}_j\hat{F}_i^{\mathrm{sp}}\rangle\right) - \hat{n}_{\mathrm{p}}k_{\mathrm{B}}T\delta_{ij}. \tag{1.2.21}$$

Integrating the Brownian constant isotropic contribution into the pressure, the extra stress is exclusively composed of the drag force contribution and the total stress writes

$$\begin{cases} \hat{\sigma}_{ij} = -\hat{p}\delta_{ij} + 2\mu\hat{E}_{ij} + \hat{\tau}_{ij}^{\mathrm{p}}, \\ \hat{\tau}_{ij}^{\mathrm{p}} = -\frac{\hat{n}_{\mathrm{p}}}{2}\left(\langle\hat{Q}_i\hat{F}_j^{\mathrm{sp}}\rangle + \langle\hat{Q}_j\hat{F}_i^{\mathrm{sp}}\rangle\right) - \hat{n}_{\mathrm{p}}k_{\mathrm{B}}T\delta_{ij}. \end{cases} \tag{1.2.22}$$

Note that using the general expression of the spring force defined in Eq. 1.2.3, the extra stress or polymer stress takes the form

$$\hat{\tau}_{ij}^{\mathrm{p}} = \hat{n}_{\mathrm{p}}\left(\hat{H}\left\langle\mathcal{H}(\hat{Q})\hat{Q}_i\hat{Q}_j\right\rangle - k_{\mathrm{B}}T\delta_{ij}\right). \tag{1.2.23}$$

In order to compute the polymer stress, one then needs to compute the term $\left\langle\mathcal{H}(\hat{Q})\hat{Q}_i\hat{Q}_j\right\rangle$ which is unknown. It is however possible to derive an equation where it appears by multiplying the Fokker-Planck equation (Eq. 1.2.17) by $\hat{Q}_i\hat{Q}_j$ and integrating over the configurational space. It gives

$$\frac{\partial}{\partial\hat{t}}\left\langle\hat{Q}_i\hat{Q}_j\right\rangle + u_i^{\infty}\frac{\partial}{\partial\hat{x}_i}\left\langle\hat{Q}_i\hat{Q}_j\right\rangle - \hat{\dot{\gamma}}_{ik}\left\langle\hat{Q}_j\hat{Q}_k\right\rangle - \hat{\dot{\gamma}}_{jk}\left\langle\hat{Q}_i\hat{Q}_k\right\rangle$$
$$= 2D\delta_{ij} + -\frac{1}{\lambda_{\mathrm{H}}}\left\langle\mathcal{H}(\hat{Q})\hat{Q}_i\hat{Q}_j\right\rangle + d\frac{\partial^2}{\partial\hat{x}_k\partial\hat{x}_k}\left\langle\hat{Q}_i\hat{Q}_j\right\rangle, \quad (1.2.24)$$

where integration by parts has been used with the fact that the configurational probability density function $\hat{\psi}$ quickly tends toward 0 as $\hat{\boldsymbol{Q}}$ approaches the boundary of the configurational space Ω, as well as for the gradient of $\hat{\psi}$ (with respect to $\hat{\boldsymbol{Q}}$).

Note that the polymer stress term needed in the momentum equation is generally unclosed. In fact, an equation for $\left\langle\hat{Q}_i\hat{Q}_j\right\rangle$ has now been derived, but it still depends on this unknown polymer stress tensor. The goal will then be to find appropriate closure approximations to close this problem.

1.3 Non-dimensionalization

The particularity of the physical problem considered is the fact that there exists fundamentally two different length scales: the typical flow length scale and the polymer length scale. This is often the case for non-Newtonian fluid flows which are composed of particles immersed in a Newtonian solvent since the length scale of the particles is often smaller than the length scale of the flow. One should however recall that this is generally not always the case and that it is an assumption that has been made previously in Sec. 1.2.1. Some quantities will thus have to be non-dimensionalized differently considering whether they refer to the flow or the polymer. However, some other quantities such as the characteristic time scale could be defined from flow quantities and polymer quantities as well.

In this work, the equations are non-dimensionalized by a flow characteristic length $\mathcal{L}$, a flow characteristic velocity $\mathcal{U}$ and a polymer characteristic length $\mathcal{Q}$. All the quantities will be non-dimensionalized by the flow characteristic length and velocity, apart from the explicitly polymer related variables, such as the connector vector or the configurational probability density function. Note that the chosen time scale is thus a flow time scale and not a polymer time scale. The non-dimensionalization from a polymer time scale is done in App. A.

The non-dimensionalization of the independent variables then leads to

$$
\begin{cases}
x_i = \dfrac{\hat{x}_i}{\mathcal{L}}, \\[2mm]
Q_i = \dfrac{\hat{Q}_i}{\mathcal{Q}}, \\[2mm]
t = \dfrac{\mathcal{U}}{\mathcal{L}}\hat{t},
\end{cases}
\Rightarrow
\begin{cases}
\dfrac{\partial}{\partial \hat{x}_i} = \dfrac{1}{\mathcal{L}}\dfrac{\partial}{\partial x_i}, \\[2mm]
\dfrac{\partial}{\partial \hat{Q}_i} = \dfrac{1}{\mathcal{Q}}\dfrac{\partial}{\partial Q_i}, \\[2mm]
\dfrac{\partial}{\partial \hat{t}} = \dfrac{\mathcal{U}}{\mathcal{L}}\dfrac{\partial}{\partial t}.
\end{cases}
\tag{1.3.1}
$$

Other quantities are non-dimensionalized as follows

$$
\begin{cases}
\hat{\dot{\gamma}}_{ij} = \dfrac{\mathcal{U}}{\mathcal{L}}\dot{\gamma}_{ij}, \\[2mm]
\hat{\psi} = \mathcal{Q}^3 \psi, \\[2mm]
\hat{\tau}^{\mathrm{p}}_{ij} = \dfrac{\tau^{\mathrm{p}}_{ij}}{\hat{n}_{\mathrm{p}} k_{\mathrm{B}} T}.
\end{cases}
\tag{1.3.2}
$$

Using the above results, Eq. 1.2.17 becomes

$$
\frac{\mathrm{D}\psi}{\mathrm{D}t} + \frac{\partial}{\partial Q_i}\left(\dot{\gamma}_{ij}Q_j\psi\right) - \frac{d}{\mathcal{U}\mathcal{L}}\frac{\partial^2 \psi}{\partial x_k \partial x_k} - \frac{D\mathcal{L}}{\mathcal{U}\mathcal{Q}^2}\frac{\partial^2 \psi}{\partial Q_k \partial Q_k} - \frac{\mathcal{L}}{2\lambda_{\mathrm{H}}\mathcal{U}}\frac{\partial}{\partial Q_i}\left(\mathcal{H}(Q)Q_i\psi\right) = 0. \tag{1.3.3}
$$

Rearranging the terms and using the expressions of the configurational diffusivity, the Rouse relaxation time scale and the spring constant from Eq. 1.2.11, the above equation

becomes

$$\frac{\mathrm{D}\psi}{\mathrm{D}t} + \frac{\partial}{\partial Q_i}\left(\dot{\gamma}_{ij}Q_j\psi\right) - \underbrace{\frac{d}{\mathcal{UL}}}_{\equiv 1/\mathrm{Pe}} \frac{\partial^2\psi}{\partial x_k \partial x_k}$$

$$- \frac{1}{2}\underbrace{\frac{\mathcal{L}}{\lambda_{\mathrm{H}}\mathcal{U}}}_{\equiv 1/\mathrm{Wi}}\left(\frac{\left\langle\hat{Q}^2\right\rangle_0}{3\mathcal{Q}^2}\frac{\partial^2\psi}{\partial Q_k \partial Q_k} + \frac{\partial}{\partial Q_i}\left(\mathcal{H}(Q)Q_i\psi\right)\right) = 0. \quad (1.3.4)$$

The Peclet number is noted Pe and defined as $\mathrm{Pe} = \mathcal{UL}/d$. It represents the relative importance of the momentum diffusion of the flow with respect to the center-of-mass diffusion of the particles. Note that as was already mentioned, the center-of-mass diffusivity is usually very small. In practice it manifests itself by a very large Peclet number: $\mathrm{Pe} \gg 1$. The Weissenberg number is noted Wi and defined as $\mathrm{Wi} = \lambda_{\mathrm{H}}\mathcal{U}/\mathcal{L}$. It measures the relative importance of the characteristic polymer time scale with respect to the characteristic flow time scale.

The next step is to choose the precise values of $\mathcal{L}, \mathcal{U}$ and $\mathcal{Q}$. The flow characteristic quantities depend on the specific flow configuration, so that it will be specified later, depending on the exact problem considered. The polymer characteristic size can however be fixed. There are multiple choices, but in the non-dimensional Fokker-Planck equation, one term suggests that

$$\mathcal{Q}^2 = \frac{N_{\mathrm{K}}b_{\mathrm{K}}^2}{3} = \frac{\left\langle\hat{Q}^2\right\rangle_0}{3} \quad\Leftrightarrow\quad \mathcal{Q} = \sqrt{\frac{\left\langle\hat{Q}^2\right\rangle_0}{3}}, \quad (1.3.5)$$

which seems appropriate. The Fokker-Planck equation then rewrites

$$\frac{\mathrm{D}\psi}{\mathrm{D}t} + \frac{\partial}{\partial Q_i}\left(\dot{\gamma}_{ij}Q_j\psi\right) - \frac{1}{\mathrm{Pe}}\frac{\partial^2\psi}{\partial x_k \partial x_k} - \frac{1}{2\mathrm{Wi}}\left(\frac{\partial^2\psi}{\partial Q_k \partial Q_k} + \frac{\partial}{\partial Q_i}\left(\mathcal{H}(Q)Q_i\psi\right)\right) = 0. \quad (1.3.6)$$

Finally, from Eq. 1.2.23, the expression of the non-dimensional polymer stress is

$$\tau_{ij}^{\mathrm{p}} = \left\langle\mathcal{H}(Q)Q_iQ_j\right\rangle - \delta_{ij} \quad (1.3.7)$$

and following the same procedure as for the Fokker-Planck equation, Eq. 1.2.24 rewrites

$$\underbrace{\frac{\mathrm{D}\left\langle Q_iQ_j\right\rangle}{\mathrm{D}t} - \dot{\gamma}_{ik}\left\langle Q_jQ_k\right\rangle - \dot{\gamma}_{jk}\left\langle Q_iQ_k\right\rangle}_{\left\langle\overset{\triangledown}{Q_iQ_j}\right\rangle} = \frac{1}{\mathrm{Wi}}\underbrace{\left(\delta_{ij} - \left\langle\mathcal{H}(Q)Q_iQ_j\right\rangle\right)}_{-\tau_{ij}^{\mathrm{p}}} + \frac{1}{\mathrm{Pe}}\frac{\partial^2\left\langle Q_iQ_j\right\rangle}{\partial x_k \partial x_k}. \quad (1.3.8)$$

Notice that the first three terms constitute the upper-convected derivative of the term $\left\langle Q_iQ_j\right\rangle$ (the upper-convected derivative is noted $\overset{\triangledown}{}$) and that the fourth term is directly proportional to the polymer stress tensor.

The equations of the flow can also be non-dimensionalized similarly. From Eq. 1.0.2–1.0.3:

$$\frac{\partial u_i}{\partial t} + u_j\frac{\partial u_i}{\partial x_j} = -\frac{1}{\rho\mathcal{U}^2}\frac{\partial\hat{p}}{\partial x_i} + \frac{\nu}{\mathcal{LU}}\frac{\partial^2 u_i}{\partial x_j \partial x_j} + \frac{\hat{n}_{\mathrm{p}}k_{\mathrm{B}}T}{\rho\mathcal{U}^2}\frac{\partial\tau_{ij}^{\mathrm{p}}}{\partial x_j}. \quad (1.3.9)$$

The pressure is then naturally non-dimensionalized as

$$p = \frac{\hat{p}}{\rho \mathcal{U}^2}. \tag{1.3.10}$$

The non-dimensional number in front of the viscous term is similar to the Reynolds number (to its inverse), but one has to keep in mind that ν is the kinematic viscosity of the solvent and not of the dilute polymer solution. The Reynolds number writes

$$\text{Re} = \frac{\rho \mathcal{U} \mathcal{L}}{\eta_{\text{T}}}, \tag{1.3.11}$$

where η_{T} is the solution dynamic viscosity and is defined as the sum of the solvent dynamic viscosity μ and the polymers zero-shear viscosity $\eta_{\text{P}} = \hat{n}_{\text{p}} k_{\text{B}} T \lambda^{\text{p}}$. Defining a concentration parameter ε that takes into account the influence of the polymer viscosity on the solution:

$$\varepsilon = \mu / \eta_{\text{T}}, \tag{1.3.12}$$

the Reynolds number rewrites

$$\text{Re} = \frac{\varepsilon \mathcal{U} \mathcal{L}}{\nu} \tag{1.3.13}$$

and the non-dimensional number in front of the viscous term takes the form ε/Re.

Using the expression of the zero-shear polymer viscosity, the non-dimensional number in front of the divergence of the polymer stress can be written as

$$\frac{\eta_{\text{P}}}{\rho \lambda^{\text{p}} \mathcal{U}^2} = \frac{(1-\varepsilon)\eta_{\text{T}}}{\rho \lambda^{\text{p}} \mathcal{U}^2} = \frac{(1-\varepsilon)\nu}{\mathcal{U}} \frac{1}{\lambda^{\text{p}} \mathcal{U}} = \frac{(1-\varepsilon)\nu}{\mathcal{U} \mathcal{L}} \frac{\mathcal{L}}{\lambda^{\text{p}} \mathcal{U}} = \frac{1-\varepsilon}{\text{ReWi}}. \tag{1.3.14}$$

The non-dimensional momentum equation takes the form

$$\frac{\partial u_i}{\partial t} + u_j \frac{\partial u_i}{\partial x_j} = -\frac{\partial p}{\partial x_i} + \frac{\varepsilon}{\text{Re}} \frac{\partial^2 u_i}{\partial x_j \partial x_j} + \frac{1-\varepsilon}{\text{ReWi}} \frac{\partial \tau_{ij}^{\text{p}}}{\partial x_j}. \tag{1.3.15}$$

It is very clear that the concentration parameter control the intensity of the influence of the polymers on the flow. In fact, if $\varepsilon = 1$, the problem is said to be *one-way coupled* as the momentum equation reduces to the Newtonian case, however the polymers equations can still be solved knowing the solution of the fluid. In this case, the polymers do not influence the fluid. Another extreme case is when $\varepsilon = 0$. In that case, the fluid is entirely composed of polymers and thus represents a polymer melt (the dilute solution hypothesis is however not valid anymore).

The continuity equation trivially becomes

$$\frac{\partial u_i}{\partial x_i} = 0. \tag{1.3.16}$$

1.4 Spring function

Different spring functions will lead to different macroscopic models. In fact, the general framework exposed in the previous sections can be particularized to specific spring functions, starting with the simpler linear spring force that yields $\mathcal{H} = 1$. A more sophisticated spring function is exposed in Sec. 1.4.2.

1.4.1   Oldroyd-B model

Considering now a Hookean spring force, such that $\mathcal{H}(\hat{Q}) = 1$, Eq. 1.3.7–1.3.8 rewrite

$$
\begin{cases}
\tau_{ij}^{\mathrm{p}} = \langle Q_i Q_j \rangle - \delta_{ij}, \\
\dfrac{\mathrm{D}\langle Q_i Q_j \rangle}{\mathrm{D}t} - \dot{\gamma}_{ik}\langle Q_j Q_k \rangle - \dot{\gamma}_{jk}\langle Q_i Q_k \rangle = \dfrac{1}{\mathrm{Wi}}\left(\delta_{ij} - \langle Q_i Q_j \rangle\right) + \dfrac{1}{\mathrm{Pe}}\dfrac{\partial^2 \langle Q_i Q_j \rangle}{\partial x_k \partial x_k}.
\end{cases}
\tag{1.4.1}
$$

Ones realizes that the second equation provides an equation for $\langle Q_i Q_j \rangle$, such that the polymer stress is closed and the contribution of the polymers to the fluid can be computed. Also, one can define the non-dimensional conformation tensor as $A_{ij} \equiv \langle Q_i Q_j \rangle$, such that the above system rewrites

$$
\begin{cases}
\tau_{ij}^{\mathrm{p}} = A_{ij} - \delta_{ij}, \\
\dfrac{\mathrm{D}A_{ij}}{\mathrm{D}t} - \dot{\gamma}_{ik}A_{jk} - \dot{\gamma}_{jk}A_{ik} = \dfrac{1}{\mathrm{Wi}}\left(\delta_{ij} - A_{ij}\right) + \dfrac{1}{\mathrm{Pe}}\dfrac{\partial^2 A_{ij}}{\partial x_k \partial x_k}.
\end{cases}
\tag{1.4.2}
$$

Alternatively, for this simple model, rather than solving the equation for the conformation tensor and then computing the polymer stress one can easily directly derive an equation for the polymer stress tensor:

$$
\frac{\mathrm{D}\tau_{ij}^{\mathrm{p}}}{\mathrm{D}t} - \dot{\gamma}_{ik}\tau_{jk}^{\mathrm{p}} - \dot{\gamma}_{jk}\tau_{ik}^{\mathrm{p}} + \frac{\tau_{ij}^{\mathrm{p}}}{\mathrm{Wi}} - \frac{1}{\mathrm{Pe}}\frac{\partial^2 \tau_{ij}^{\mathrm{p}}}{\partial x_k \partial x_k} = 2E_{ij}.
\tag{1.4.3}
$$

Neglecting the center-of-mass diffusivity, this provides a constitutive equation called the Oldroyd-B model:

$$
\overset{\triangledown}{\tau}_{ij}^{\mathrm{p}} + \frac{\tau_{ij}^{\mathrm{p}}}{\mathrm{Wi}} = 2E_{ij}.
\tag{1.4.4}
$$

An interesting particular case is the one of a steady uniaxial extensional flow. For this academic flow configuration, the velocity gradient writes

$$
\dot{\boldsymbol{\gamma}} = \boldsymbol{E} = \dot{\varepsilon}\begin{pmatrix} 1 & 0 & 0 \\ 0 & -\frac{1}{2} & 0 \\ 0 & 0 & -\frac{1}{2} \end{pmatrix},
\tag{1.4.5}
$$

where $\dot{\varepsilon}$ is the non-dimensional strain rate. Note that the velocity gradient tensor is symmetric in this case such that it is equal to the strain rate tensor. Injecting the above result in Eq. 1.4.4, a steady solution can be found for the polymer stress:

$$
\boldsymbol{\tau}^{\mathrm{p}} = \begin{pmatrix} \frac{2\dot{\varepsilon}\mathrm{Wi}}{1-2\dot{\varepsilon}\mathrm{Wi}} & 0 & 0 \\ 0 & -\frac{\dot{\varepsilon}\mathrm{Wi}}{1+\dot{\varepsilon}\mathrm{Wi}} & 0 \\ 0 & 0 & -\frac{\dot{\varepsilon}\mathrm{Wi}}{1+\dot{\varepsilon}\mathrm{Wi}} \end{pmatrix}.
\tag{1.4.6}
$$

As can be seen, for the particular value $\dot{\varepsilon} = (2\mathrm{Wi})^{-1}$, the polymer stress (τ_{11}^{p}) grows unbounded, which has no sense from a physical point of view. This is a practical consequence of the linear spring force that does not prevent any elongation.

1.4.2 Warner spring and FENE model

As already discussed several times, assuming a linear spring law does not impose any bounds on the polymer extension and more generally, it is similar for any spring law that has an infinite domain. As already mentioned, this infinite extensibility makes no sense from a physical point of view as each polymer chain possesses a finite maximum extension. Considering again the freely jointed chain approximation, the maximal extension of the chain is the sum of the length of each rod. Taking this into account, it is possible to write the expression of the average end-to-end distance as a function of the applied force and this is known as the Langevin function. The inverse of that function then yields the spring force (as a function of the polymer extension). The Langevin function is however not analytically invertible, but it is possible to find an analytical approximation to the inverse Langevin function. A typical approximation is the Warner spring force, yielding the Warner spring function

$$\mathcal{H}(\hat{Q}) = \frac{1}{1 - \hat{Q}^2/\hat{Q}_{\max}^2}, \tag{1.4.7}$$

where $\hat{Q}_{\max}^2$ is the square of the maximum extension that a dumbbell can take. The dumbbell model complemented with the Warner spring force is referred to as the FENE (Finite Extensible Nonlinear Elastic) model. In practice, the Warner spring force then presents a singularity at $\hat{Q} = \hat{Q}_{\max}$, such that the force needed to extends a dumbbell to its maximal extension is infinite, or inversely, an infinite force would yield a finite extension $\hat{Q}_{\max}$.

Considering the non-dimensionalization used before naturally yields

$$\mathcal{H}(Q) = \frac{1}{1 - Q^2/b}, \quad \text{with} \quad b = \frac{\hat{Q}_{\max}^2}{\mathcal{Q}} = \frac{3\hat{Q}_{\max}^2}{\langle \hat{Q}^2 \rangle_0}, \tag{1.4.8}$$

where b is the non-dimensional polymer maximum square extension, also called the non-dimensional extensibility parameter. In this context, Eq. 1.3.8 rewrites

$$\frac{\mathrm{D} \langle Q_i Q_j \rangle}{\mathrm{D}t} - \dot{\gamma}_{ik} \langle Q_j Q_k \rangle - \dot{\gamma}_{jk} \langle Q_i Q_k \rangle = \frac{1}{\mathrm{Wi}} \left(\delta_{ij} - \left\langle \frac{Q_i Q_j}{1 - Q^2/b} \right\rangle \right) + \frac{1}{\mathrm{Pe}} \frac{\partial^2 \langle Q_i Q_j \rangle}{\partial x_k \partial x_k}, \tag{1.4.9}$$

with the polymer stress tensor

$$\tau_{ij}^{\mathrm{p}} = \left\langle \frac{Q_i Q_j}{1 - Q^2/b} \right\rangle - \delta_{ij}. \tag{1.4.10}$$

The difficulty is that now, the spring force term is unclosed as it cannot generally be expressed as a function of the conformation tensor. This is due to the non-linearity of the spring force (or the fact that the spring function is not a constant with respect to Q). The consequence is that there is no closed form expression for the polymer stress tensor and one will have to find alternatives in order to compute it anyway.

The first option is to directly solve for the configurational probability distribution function ψ in the Fokker-Planck equation. The problem of this approach is the high dimensionality because of the positional and configurational dependency of ψ. Indeed

if one is interested in a three-dimensional flow, the problem is six-dimensional. This makes it a very computationally intensive method, unsuited to real flow applications but high fidelity.

The second method is to use Brownian dynamics simulations to follow the dumbbells through the dumbbells equations of motion (Eq. 1.2.5) where the Brownian force term is modeled as a stochastic force, using Wiener processes. The main limitation of this method is the convergence rate of the statistics, which is quite low. This can however also constitutes a high fidelity solution of the FENE equations.

Finally, the method that is used in this work is to derive closure approximations to try to express the average of the non-linear term as a function of the known quantities. The difficulty is then to find good closure approximations.

1.4.3 FENE-P closure approximation

The first proposed and simpler closure approximation of the unclosed term

$$\left\langle \frac{Q_i Q_j}{1 - Q^2/b} \right\rangle \tag{1.4.11}$$

is known as the Peterlin approximation, leading to the FENE-P model. It consists in considering a pre-averaged spring function $\mathcal{H}_{\mathrm{P}}(Q) = \mathcal{H}(\langle Q \rangle)$, such that the spring force becomes

$$\boldsymbol{F}_{\mathrm{P}}^{\mathrm{sp}}(\boldsymbol{Q}) = -\mathcal{H}_{\mathrm{P}}(Q)\boldsymbol{Q} = -\frac{\boldsymbol{Q}}{1 - \langle Q^2 \rangle /b}, \tag{1.4.12}$$

where the P subscript denotes the Peterlin approximation. The unclosed term thus becomes

$$\langle \mathcal{H}(Q)Q_iQ_i \rangle \approx \langle \mathcal{H}_{\mathrm{P}}(Q)Q_iQ_j \rangle = \left\langle \frac{Q_iQ_j}{1 - \langle Q^2 \rangle /b} \right\rangle = \frac{\langle Q_iQ_j \rangle}{1 - \langle Q^2 \rangle /b} = \frac{\langle Q_iQ_j \rangle}{1 - \langle Q_iQ_i \rangle /b}, \tag{1.4.13}$$

which is an explicit function of the conformation tensor. Using the Peterlin approximation and the non-dimensional conformation tensor notation, the equation for the conformation tensor then writes

$$\frac{\mathrm{D}A_{ij}}{\mathrm{D}t} - \dot{\gamma}_{ik}A_{jk} - \dot{\gamma}_{jk}A_{ik} = \frac{1}{\mathrm{Wi}}\left(\delta_{ij} - \frac{A_{ij}}{1 - A_{kk}/b}\right) + \frac{1}{\mathrm{Pe}}\frac{\partial^2 A_{ij}}{\partial x_k \partial x_k}, \tag{1.4.14}$$

with the polymer stress tensor

$$\tau_{ij}^{\mathrm{P}} = \frac{A_{ij}}{1 - A_{kk}/b} - \delta_{ij}. \tag{1.4.15}$$

The conformation tensor equation is then closed and and the polymer stress is expressed as a function the conformation tensor, such that one can solve for $\boldsymbol{A}$ and then computes $\boldsymbol{\tau}^{\mathrm{P}}$. Note that in the following, the notation A will be used to denote the trace of the conformation tensor: $A \equiv A_{kk} = \mathrm{tr}\,(\boldsymbol{A})$.

The FENE-P closure model has been used quite a lot to model dilute polymer solution fluids in complex flow configurations. In particular this model has been used extensively for Eulerian simulations of drag reduction and elasto-inertial turbulence.

The Peterlin approximation however introduces strong deviations from the actual FENE dynamics. In fact, the pre-averaged square extension has some impact on the polymer statistics and this has already been extensively studied by Keunings [5].

The first thing to realize is the fact that through the pre-averaging approximation, only the mean square extension $\langle Q^2 \rangle$ is bounded, but it is generally not the case for the dumbbells extension Q (nor square extension Q^2). In fact, considering a fluid volume element that contains many dumbbells, it is equivalent to saying that for the FENE model, all the dumbbells (non-dimensional) extension cannot exceed $\sqrt{b}$, while for the FENE-P model, the dumbbells can do so as long as the averaged square extension is bounded.

Another limitation lies in the fact that the polymer stress tensor is directly expressed as a function of the conformation tensor, meaning that for any conformation tensor $\boldsymbol{A}$, there exists only one polymer stress tensor $\boldsymbol{\tau}^{\mathrm{p}}$. This is however not the case for the general FENE model[6] as shown extensively in one-dimensional problems by Keunings [5]. In fact, the FENE dynamics presents an hysteretic behavior between the conformation tensor and the polymer stress tensor, coming from the fact that the later is not expressed as a direct function of the former. The consequence is that any model expressing $\boldsymbol{\tau}^{\mathrm{p}} = \boldsymbol{\tau}^{\mathrm{p}}(\boldsymbol{A})$ (as the FENE-P does) is not able to show the hysteretic behavior.

Finally, it has been shown that the results of the FENE-P are in good accordance with the FENE results for steady flows. However, for highly transient flows, the results are often quite wrong. Since the objective is to derive good closure approximations in order to solve turbulent flows, where the velocity gradients are very chaotic and unpredictable, it is of paramount importance to find closure approximations that are able to represent the hysteresis and if possible, that are qualitatively correct in transient flows.

---

[6]From Sec. 1.4.2, recall that there exists different ways of computing the polymer stress. The method employed here consists in closure approximation but more elaborate and higher fidelity methods exist (though more computationally intensive) which enable assessment of the accuracy of any closure model.

Chapter 2

FENE-L and FENE-LS closure approximations

Before diving into the development of more advanced models, note that the derivations of the models presented in this section were introduced by Lielens *et al.* [6, 7]. These articles are considered as a reference for the developments made in this chapter.

In the previous chapter, the Fokker-Planck equation has been multiplied by Q_iQ_j before being integrated on the configuration space, in order to derive a transport equation for the conformation tensor $\boldsymbol{A}$. The goal of this section is to apply the same procedure for another quantity, in order to derive a second transport equation, which will also eventually exhibit unclosed terms.

The quantity that will be considered here is Q^4. Multiplying Eq. 1.3.6 by Q^4 and integrating over Ω gives

$$\frac{\mathrm{D}\langle Q^4\rangle}{\mathrm{D}t} - 4\dot{\gamma}_{ij}\langle Q_iQ_jQ^2\rangle = \frac{1}{\mathrm{Wi}}\left(10\langle Q^2\rangle - 2\langle\mathcal{H}(Q)Q^4\rangle\right) + \frac{1}{\mathrm{Pe}}\frac{\partial^2\langle Q^4\rangle}{\partial x_k\partial x_k}. \tag{2.0.1}$$

It is then possible to define the radial dispersion of dumbbells $B \equiv \langle Q^4\rangle$ and using the notation of the conformation tensor:

$$\frac{\mathrm{D}B}{\mathrm{D}t} - 4\dot{\gamma}_{ij}\langle Q_iQ_jQ^2\rangle = \frac{1}{\mathrm{Wi}}\left(10A - 2\langle\mathcal{H}(Q)Q^4\rangle\right) + \frac{1}{\mathrm{Pe}}\frac{\partial^2 B}{\partial x_k\partial x_k}. \tag{2.0.2}$$

Considering the transport equations for $\boldsymbol{A}$ and B, there are now several unclosed terms and in order to make the distinction between all of them, one introduces the following notations:

$$\begin{cases} \dfrac{\mathrm{D}A_{ij}}{\mathrm{D}t} - \dot{\gamma}_{ik}A_{jk} - \dot{\gamma}_{jk}A_{ik} = \dfrac{1}{\mathrm{Wi}}\left(\delta_{ij} - A_{ij}^{\mathrm{sp}}\right) + \dfrac{1}{\mathrm{Pe}}\dfrac{\partial^2 A_{ij}}{\partial x_k\partial x_k}, \\[2ex] \dfrac{\mathrm{D}B}{\mathrm{D}t} - 4\dot{\gamma}_{ij}B_{ij}^{\mathrm{d}} = \dfrac{1}{\mathrm{Wi}}\left(10A - 2B^{\mathrm{sp}}\right) + \dfrac{1}{\mathrm{Pe}}\dfrac{\partial^2 B}{\partial x_k\partial x_k}, \end{cases} \tag{2.0.3}$$

where

$$\begin{cases} A_{ij}^{\mathrm{sp}} = \langle\mathcal{H}(Q)Q_iQ_j\rangle = \left\langle\dfrac{Q_iQ_j}{1 - Q^2/b}\right\rangle, \\[2ex] B_{ij}^{\mathrm{d}} = \langle Q_iQ_jQ^2\rangle, \\[2ex] B^{\mathrm{sp}} = \langle\mathcal{H}(Q)Q^4\rangle = \left\langle\dfrac{Q^4}{1 - Q^2/b}\right\rangle \end{cases} \tag{2.0.4}$$

and the *sp* and *d* notations respectively refer to the spring force and drag force terms. Injecting the above results in Eq. 1.4.10 also yields

$$\tau_{ij}^{\mathrm{p}} = A_{ij}^{\mathrm{sp}} - \delta_{ij}. \tag{2.0.5}$$

As was done for the FENE-P with the Peterlin approximation, one then needs to find appropriate closure approximations to express the unclosed terms as functions of the known quantities. This kind of developments have been studied in details by Lielens *et al.* [6, 7] using a very general framework. Only the essential explanations are kept here in order to remain clear and concise.

2.1 Decoupled canonical subspace

Before considering more complex closure approximations (than the classical Peterlin approximation) it is useful to enumerate the different properties and restrictions of the configurational probability distribution function ψ. In order to do so, one can define the space of admissible configurational probability distributions, noted Φ. The three properties of ψ are the positivity, a normalization condition and a symmetry condition[1]. More mathematically:

$$\forall \boldsymbol{Q} \in \Omega, \forall \psi \in \Phi : \begin{cases} \psi(\boldsymbol{Q}) \geq 0, \\ \displaystyle\int_{\Omega} \psi(\boldsymbol{Q}) \mathrm{d}\boldsymbol{Q} = 1, \\ \psi(-\boldsymbol{Q}) = \psi(\boldsymbol{Q}), \end{cases} \tag{2.1.1}$$

where Ω is the configurational space, or the space of admissible connector vector $\boldsymbol{Q}$. Considering now a finite maximal extension of the dumbbells, Ω is defined as

$$\forall \boldsymbol{Q} \in \Omega : \boldsymbol{Q} \cdot \boldsymbol{Q} \leq b, \tag{2.1.2}$$

which describes a centered ball of radius $\sqrt{b}$.

The set of admissible distributions Φ is of infinite dimension, but one can consider only a subset of Φ noted Φ^{c} ($\Phi^{\mathrm{c}} \subset \Phi$) of finite dimension. This is called the canonical subspace and its dimension is noted m. One can then choose a set $p = \{\alpha, \beta, ...\}$ of m parameters and write a parameterized distribution, called canonical configurational distribution with this set. The distribution belongs to the canonical subspace and is noted ψ_p^{c}. The goal is to approximate the general configurational distribution function ψ by restricting its number of degree of freedom. Of course, the choice of the parameters and of the expression of ψ_p^{c} is crucial in obtaining a good approximation. A very important point is that, depending on the parameterization of the canonical probability density distribution, it may not stay inside its canonical subspace under the FENE dynamics described by the Fokker-Planck equation.

---

[1]The symmetry condition is there to take into account the fact that the probability of finding a dumbbell with a given configuration (at a given position) is the same as finding the same dumbbell in the opposite configuration. In fact, since both beads of a dumbbells are the same and its center of mass is also its geometrical center, inverting both beads should not be noticeable.

More concretely, the way the configurational distribution function ψ comes into account is through the configurational space average $\langle \cdot \rangle$. One can thus approximate this average by the canonical configurational space average noted $\langle \cdot \rangle_c$:

$$\langle \cdot \rangle = \int_\Omega \cdot \; \psi(\boldsymbol{Q})\mathrm{d}\boldsymbol{Q} \approx \int_\Omega \cdot \; \psi_p^c(\boldsymbol{Q})\mathrm{d}\boldsymbol{Q} = \langle \cdot \rangle_c \,. \tag{2.1.3}$$

Note that the canonical distribution should still satisfy the properties of the distribution functions belonging to Φ (Eq. 2.1.1) since $\Phi^c \subset \Phi$.

The difficulty here is to deal with multivariate distributions ($\boldsymbol{Q}$ is of dimension three). In fact, it is especially hard to derive good and meaningful parameterized canonical distribution functions in such a *high* dimensional space. One way to alleviate this problem is to introduce another layer of approximation, which yields the decoupled canonical subspace. It consists in assuming a decoupled influence of the extension and orientation of the dumbbells by the mean of two decoupled distributions:

$$\psi_p^c(\boldsymbol{Q}) = \psi_p^Q(Q)\psi_p^{\boldsymbol{u}}(\boldsymbol{u}), \tag{2.1.4}$$

where $\boldsymbol{u} = \boldsymbol{Q}/Q$ is the dumbbell orientation, ψ_p^Q is called the canonical extension probability distribution and $\psi_p^{\boldsymbol{u}}$ is called the canonical orientation probability distribution. The integral over the configurational space can then be decomposed as

$$\begin{aligned} \int_\Omega \cdot \; \psi_p^c(\boldsymbol{Q})\mathrm{d}\boldsymbol{Q} &= \int_0^{\sqrt{b}} \oiint \cdot \; \psi_p^Q(Q)\psi_p^{\boldsymbol{u}}(\boldsymbol{u})Q^2\mathrm{d}Q\mathrm{d}\boldsymbol{u} \\ &= \int_0^{\sqrt{b}} Q^2\psi_p^Q(Q)\left(\oiint \cdot \; \psi_p^{\boldsymbol{u}}(\boldsymbol{u})\mathrm{d}\boldsymbol{u} \right)\mathrm{d}Q, \end{aligned} \tag{2.1.5}$$

where the volume element $\mathrm{d}\boldsymbol{Q}$ transforms into $\mathrm{d}Q\mathrm{d}S = \mathrm{d}QQ^2\mathrm{d}\boldsymbol{u}$, where $\mathrm{d}S$ is the surface element (for a given Q) and $\mathrm{d}\boldsymbol{u}$ the infinitesimal solid angle. The closed double integral $\oiint$ is computed over the unit sphere.

The properties (Eq. 2.1.1) of the decoupled canonical distribution function still need to be satisfied. One imposes $\psi_p^Q \geq 0$ and $\psi_p^{\boldsymbol{u}} \geq 0$ and in order to make ψ_p^c even, one needs to consider an even orientation distribution $\psi_p^{\boldsymbol{u}}$, that is $\psi_p^{\boldsymbol{u}}(\boldsymbol{u}) = \psi_p^{\boldsymbol{u}}(-\boldsymbol{u})$. Moreover, one could want to choose a normalized orientation distribution function $\psi_p^{\boldsymbol{u}}$ such that

$$\oiint \psi_p^{\boldsymbol{u}}(\boldsymbol{u})\mathrm{d}\boldsymbol{u} = 1. \tag{2.1.6}$$

Using Eq. 2.1.5–2.1.6,

$$\int_\Omega \psi_p^c(\boldsymbol{Q})\mathrm{d}\boldsymbol{Q} = \int_0^{\sqrt{b}} Q^2\psi_p^Q(Q)\mathrm{d}Q, \tag{2.1.7}$$

and using the normalization property of the canonical configuration distribution,

$$\int_0^{\sqrt{b}} Q^2\psi_p^Q(Q)\mathrm{d}Q = 1. \tag{2.1.8}$$

Finally, one can define a canonical radial probability distribution $\rho_p^c(Q) \equiv Q^2\psi_p^Q(Q)$.

It is then possible to compute the different averaged quantities using the decoupled canonical approximation:

$$
\begin{cases}
A_{ij} \approx \left(\int_0^{\sqrt{b}} Q^2 \rho_p^c(Q)\mathrm{d}Q \right) \underbrace{\left(\oiint u_i u_j \psi_p^{\boldsymbol{u}}(\boldsymbol{u})\mathrm{d}\boldsymbol{u} \right)}_{A_{ij}/A}, \\[4mm]
A \approx \int_0^{\sqrt{b}} Q^2 \rho_p^c(Q)\mathrm{d}Q, \\[4mm]
B \approx \int_0^{\sqrt{b}} Q^4 \rho_p^c(Q)\mathrm{d}Q,
\end{cases}
\qquad
\begin{cases}
A_{ij}^{\mathrm{sp}} \approx \left(\int_0^{\sqrt{b}} \dfrac{Q^2}{1 - Q^2/b} \rho_p^c(Q)\mathrm{d}Q \right) \dfrac{A_{ij}}{A}, \\[4mm]
B_{ij}^{\mathrm{d}} \approx B \dfrac{A_{ij}}{A}, \\[4mm]
B^{\mathrm{sp}} \approx \int_0^{\sqrt{b}} \dfrac{Q^4}{1 - Q^2/b} \rho_p^c(Q)\mathrm{d}Q.
\end{cases}
$$

$$(2.1.9)$$

From the above results, several interesting observations can be made. First, the drag term for B is closed and expressed as a combination of the conformation tensor and the radial dispersion. Moreover, the spring unclosed tensor for the conformation tensor equation has been simplified such that it is directly proportional to $\boldsymbol{A}$. The only remaining unclosed terms of the system are thus scalars which greatly simplifies the closure problem. As was done for the conformation tensor, one notes $\mathrm{tr}\left(\boldsymbol{A}^{\mathrm{sp}}\right)$ as

$$
A^{\mathrm{sp}} \approx \int_0^{\sqrt{b}} \frac{Q^2}{1 - Q^2/b} \rho_p^c(Q)\mathrm{d}Q. \tag{2.1.10}
$$

Finally, one realizes that only the radial probability distribution function has to be restricted to a canonical subset. In fact, the orientation probability distribution function is left unspecified. This also greatly simplifies the parameterization work as the distribution is simply one-dimensional rather being a trivariate distribution. The benefits of the decoupling approximation are now clear.

The above results can be injected in Eq. 2.0.3 and 2.0.5:

$$
\begin{cases}
\dfrac{\mathrm{D}A_{ij}}{\mathrm{D}t} - \dot{\gamma}_{ik}A_{jk} - \dot{\gamma}_{jk}A_{ik} = \dfrac{1}{\mathrm{Wi}}\left(\delta_{ij} - \dfrac{A^{\mathrm{sp}}}{A}A_{ij} \right) + \dfrac{1}{\mathrm{Pe}}\dfrac{\partial^2 A_{ij}}{\partial x_k \partial x_k}, \\[4mm]
\dfrac{\mathrm{D}B}{\mathrm{D}t} - \dfrac{4B}{A}\dot{\gamma}_{ij}A_{ij} = \dfrac{1}{\mathrm{Wi}}\left(10A - 2B^{\mathrm{sp}}\right) + \dfrac{1}{\mathrm{Pe}}\dfrac{\partial^2 B}{\partial x_k \partial x_k}
\end{cases}
\tag{2.1.11}
$$

with

$$
\tau_{ij}^{\mathrm{p}} = \frac{A^{\mathrm{sp}}}{A}A_{ij} - \delta_{ij}. \tag{2.1.12}
$$

Note that the condition for a model to show the hysteretic behavior is that A^{sp} is not only a function of $\boldsymbol{A}$.

2.2 Parameterization of ρ^{c}

The goal is now to restrict the number of degrees of freedom for the radial probability density distribution. Note first that since there are two unclosed terms, two parameters are needed and these are denoted α and β respectively, such that the radial probability density distribution is noted $\rho_{\alpha,\beta}^c$. The challenge is now to come up with a meaningful and proper parameterization so that $\rho_{\alpha,\beta}^c$ exhibits the right behavior. In order to do so,

one can refer to higher fidelity simulations (solution of the discretized Fokker-Planck equation or stochastic Brownian dynamics) that can have access to such distributions for specific flows in order to visualize the different possible shapes that it can take. The specific evolution of the configurational probability distribution is studied in details for one-dimensional flows (and three-dimensional extensional flows) in the work of Keunings [5] and Lielens *et al.* [6]. From there, for different kind of flows, the configurational probability density distribution seems to show a plateau at low to moderate polymer extensions, but exhibits a large peak at high extensions. This is however not true at equilibrium since the configurational probability density distribution locally takes the form of a Gaussian distribution (as discussed in Sec. 1.1.1).

Finally, one should keep in mind that since the goal is to express the unclosed terms as a function of the known quantities, the more complex the expression of $\rho^{\mathrm{c}}_{\alpha,\beta}$ is, the more complex the developments will be (this is not a general rule). Also for too complex expressions, the analytical analysis of the properties of the closure could become difficult. By extension, for too complex $\rho^{\mathrm{c}}_{\alpha,\beta}$, it could be impossible to write analytical expressions for the unclosed terms.

2.2.1 FENE-L

In order to approximate the higher fidelity results described above, $\rho^{\mathrm{c}}_{\alpha,\beta}$ takes the shape of a uniform distribution followed by a Dirac. The position of the Dirac is fixed at $Q = \alpha$ whereas the relative importance of the uniform distribution over the Dirac is controlled by the β parameter. The expression of the radial probability distribution function is then

$$\rho^{\mathrm{c}}_{\alpha,\beta}(Q) = \frac{1-\beta}{\alpha}\left[1 - H_\alpha(Q)\right] + \beta\delta_\alpha(Q), \tag{2.2.1}$$

where H_α and δ_α are the Heavyside and Dirac distribution respectively, located at $Q = \alpha$. $\rho^{\mathrm{c}}_{\alpha,\beta}$ should satisfy the properties mentioned in Sec. 2.1 such that it should be normalized (which is the case here) and positive. Also the maximal dumbbell extension should be $Q = \sqrt{b}$ such that the support of $\rho^{\mathrm{c}}_{\alpha,\beta}$ is $[0, \sqrt{b}]$. This implies that $(\alpha, \beta) \in [0, \sqrt{b}] \times [0, 1]$. A graphical representation of $\rho^{\mathrm{c}}_{\alpha,\beta}$ is shown in Fig. 2.2.1. The name of the model is taken from the L-shaped radial probability distribution function.

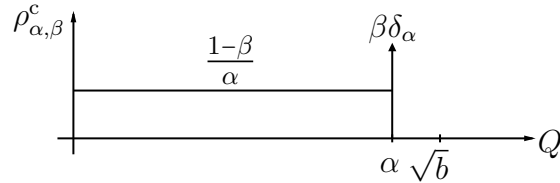Figure 2.2.1: Representation of the FENE-L radial probability distribution function $\rho^{\mathrm{c}}_{\alpha,\beta}$.

The quantities A, B, A^{sp} and B^{sp} can be computed using the FENE-L canonical

radial distribution. Their expressions are

$$
\begin{cases}
A \approx \beta\alpha^2 + \dfrac{(1-\beta)\alpha^2}{3}, \\[2mm]
B \approx \beta\alpha^4 + \dfrac{(1-\beta)\alpha^4}{5},
\end{cases}
\quad
\begin{cases}
A^{\mathrm{sp}} \approx \dfrac{\beta\alpha^2}{1-\alpha^2/b} + (1-\beta)b\left(\dfrac{\sqrt{b}}{2\alpha}\ln\left(\dfrac{\sqrt{b}+\alpha}{\sqrt{b}-\alpha}\right)-1\right), \\[3mm]
B^{\mathrm{sp}} \approx \dfrac{\beta\alpha^4}{1-\alpha^2/b} + (1-\beta)b^2\left(\dfrac{\sqrt{b}}{2\alpha}\ln\left(\dfrac{\sqrt{b}+\alpha}{\sqrt{b}-\alpha}\right)-1-\dfrac{\alpha^2}{3b}\right).
\end{cases}
\tag{2.2.2}
$$

At this point, note that the precise analytical expressions of A^{sp} and B^{sp} coming from definite integrals differ from the original articles of Lielens *et al.* [6, 7]. After careful mathematical investigation, it seems to be an error (developments available in App. B). In the following, the present (considered correct) expressions are used to derive the different results. Note that this suspected error will result in significant changes in the properties of the model.

The goal is then to invert the expressions of A and B in order to express α and β as functions of A and B, so that it can be injected in the expressions of A^{sp} and B^{sp}. Both unclosed terms will then be expressed as functions of the known quantities. The inversion of the first two equations can be done an gives the relations

$$
\begin{cases}
\alpha^2 = \dfrac{5B}{3A \pm \sqrt{9A^2 - 5B}}, \\[3mm]
\beta = \dfrac{(9A^2 - 5B) \pm \sqrt{(9A^2 - 5B)9A^2}}{10B}.
\end{cases}
\tag{2.2.3}
$$

Note that since it would not add any value, these results are not injected in the expression of A^{sp} and B^{sp}.

The above expressions present a surprising result as the same couple (A, B) can give rise to two different couples (α, β). The change of variable is therefore not bijective. Depending on the sign chosen in Eq. 2.2.3, the solution will be noted $(\overline{\alpha}, \overline{\beta})$ for the '+' sign and $(\tilde{\alpha}, \tilde{\beta})$ for the '−' sign. Also, the '+' solution will be called the *natural* solution, while the '−' will be called the *ghost* solution. Note also that $A^{\mathrm{sp}}(\overline{\alpha}, \overline{\beta}) \neq A^{\mathrm{sp}}(\tilde{\alpha}, \tilde{\beta})$ and the same holds for B^{sp}. At first, there seems to be an intrinsic problem with the model. In fact, when solving the problem in the (A, B) space, both natural and ghost solutions a priori exist and one could not know which one to choose. Only the natural solution will be considered at first and this will be justified later.

Another technical difficulty is the square root in the expression of α^2. In fact, in order for (α, β) to remain real, the argument of the square root should be positive, which adds the condition

$$
B \leq \frac{9}{5}A^2,
\tag{2.2.4}
$$

that is not satisfied a priori. Such conditions are sometimes complex to deal with numerically, depending on the kind of solver used.

2.2.2 FENE-LS

The closure expressions of the FENE-L model being quite complex analytically, it is difficult to really understand the behavior of the model. Also, the complexity of the closure expressions can slow down the numerical solver as evaluating these expressions

is expensive. This is thus the motivation to mathematically simplify the expression of $\rho^c_{\alpha,\beta}$ and derive a new model which is called the FENE-LS and stands for *simplified FENE-L*. The choice is to approximate the uniform distribution of the FENE-L by a Dirac at some location $Q = \alpha/R$ where R is a constant whose value will be specified later. The expression of the radial probability distribution is then

$$\rho^c_{\alpha,\beta}(Q) = (1 - \beta)\delta_{\alpha/R} + \beta\delta_\alpha, \tag{2.2.5}$$

and the parameters lie in the same parameter space as for the FENE-L model: $(\alpha, \beta) \in [0, \sqrt{b}] \times [0, 1]$. A graphical representation of $\rho^c_{\alpha,\beta}$ is shown in Fig. 2.2.2.
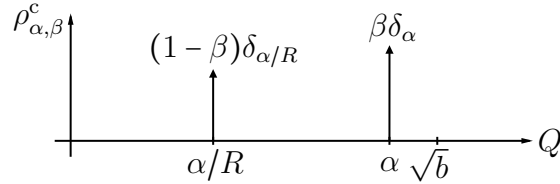

Figure 2.2.2: Representation of the FENE-LS radial probability distribution function $\rho^c_{\alpha,\beta}$.

The same developments as for the FENE-L can be made here. The expressions of the quantities of interest are thus

$$\begin{cases} A \approx \alpha^2 \left(\beta + \dfrac{1-\beta}{R^2} \right), \\ B \approx \alpha^4 \left(\beta + \dfrac{1-\beta}{R^4} \right), \end{cases} \begin{cases} A^{\mathrm{sp}} \approx \alpha^2 \left(\beta \dfrac{1}{1 - \alpha^2/b} + \dfrac{1-\beta}{R^2} \dfrac{1}{1 - \alpha^2/(R^2 b)} \right), \\ B^{\mathrm{sp}} \approx \alpha^4 \left(\beta \dfrac{1}{1 - \alpha^2/b} + \dfrac{1-\beta}{R^4} \dfrac{1}{1 - \alpha^2/(R^2 b)} \right) \end{cases} \tag{2.2.6}$$

and inverting the two first equations yields

$$\begin{cases} \alpha^2 = \dfrac{2R^2 B}{A(R^2 + 1)} \dfrac{1}{1 \pm \sqrt{1 - \frac{4R^2 B}{A^2(R^2+1)^2}}}, \\ \beta = \dfrac{\frac{AR^2}{\alpha^2} - 1}{R^2 - 1}. \end{cases} \tag{2.2.7}$$

The same comment about the non-bijectivity of the mapping $(A, B) \to (\alpha, \beta)$ holds, but note that only the natural solution will again be used (this will be justified later). The argument of the square root also needs to be positive such that

$$B \le \frac{(R^2 + 1)^2}{4R^2} A^2 \tag{2.2.8}$$

should be imposed. Note that this has the exact same form as the equivalent condition for the FENE-L (Eq. 2.2.4). In fact, one notices that if $R^2 = 5$, the condition is exactly the same. The R constant is thus fixed to $\sqrt{5}$ in order to obtain similar results than for the FENE-L with the hope that the Dirac distribution at α/R well approximates the uniform distribution.

In order to simplify even further this simplified model, it is possible to approximate the square root by a linear expression, such that the above condition disappears. Since the argument of the square root can a priori vary between 0 and 1, it is difficult to apply a rigorous Taylor expansion. The square root is thus approximated as

$$\sqrt{1 - \frac{4R^2 B}{A^2(R^2+1)^2}} \approx 1 - \gamma \frac{4R^2 B}{A^2(R^2+1)^2}, \tag{2.2.9}$$

where γ is a constant that needs to be fixed in order to obtain a meaningful approximation. It can be showed that $B = A^2$ corresponds to a Dirac distribution. This distribution can be achieved in the FENE-LS model for $\beta = 1$ and from Eq. 2.2.7, $\beta = 1$ implies that $\alpha^2 = A$. All these results are illustrated in the next section (Sec. 2.2.3).

Injecting Eq. 2.2.9 into Eq. 2.2.7 and using $B = A^2$, $A = \alpha^2$ and $\beta = 1$, it is possible to show that $\gamma = (R^2 + 1)/(2R^2)$. Injecting the square root approximation with the value of γ in the natural expression of (α, β) yields

$$\begin{cases} \overline{\alpha}^2 = \dfrac{AR^2}{\frac{A^2(R^2+1)}{B} - 1}, \\ \overline{\beta} = \dfrac{\frac{A^2(R^2+1)}{B} - 2}{R^2 - 1}. \end{cases} \tag{2.2.10}$$

One last approximation is to consider that the second term in the expressions of A^{sp} and B^{sp} can be approximated as

$$\frac{1}{1 - \alpha^2/(R^2 b)} \approx 1, \tag{2.2.11}$$

such that the final approximated closure expressions are

$$\begin{cases} A^{\mathrm{sp}} = \overline{\alpha}^2 \left(\overline{\beta} \dfrac{1}{1 - \overline{\alpha}^2/b} + \dfrac{1 - \overline{\beta}}{R^2} \right), \\ B^{\mathrm{sp}} = \overline{\alpha}^4 \left(\overline{\beta} \dfrac{1}{1 - \overline{\alpha}^2/b} + \dfrac{1 - \overline{\beta}}{R^4} \right), \end{cases} \tag{2.2.12}$$

where only the natural solution has been considered. Again, in order to obtain the explicit expressions of A^{sp} and B^{sp} in terms of A and B, one can inject Eq. 2.2.10 in the above expressions, but this is not done here.

As several mathematical simplifications were introduced in the FENE-LS model, it may be useful to distinguish between two submodels. The FENE-LS$_0$ model denotes the FENE-LS model without any mathematical approximation whereas the FENE-LS$_1$ model denotes the FENE-LS model taking into account the approximations of both the square root in the expressions of α^2 and β and the fraction in the expressions of A^{sp} and B^{sp}. The version of the FENE-LS model that is used in the reference article [7] is the FENE-LS$_1$ (simply called FENE-LS).

Finally, note that the different approximations present in the FENE-LS$_1$ model makes it deviate from the radial probability distribution originally presented. In fact, the unclosed terms are not exactly defined anymore through the integral of $\rho^{\mathrm{c}}_{\alpha,\beta}$ because of the different approximations. It would thus be wrong to try to understand the solution in terms of $\rho^{\mathrm{c}}_{\alpha,\beta}$.

2.2.3 FENE-P

It is interesting to understand that it is also possible to derive the well known FENE-P model through this general formalism. In fact, considering only one parameter α and the simple canonical radial distribution

$$\rho_\alpha^c = \delta_\alpha(Q), \tag{2.2.13}$$

A and A^{sp} are expressed as

$$A = \alpha^2, \quad A^{\mathrm{sp}} = \frac{\alpha^2}{1 - \alpha^2/b}, \tag{2.2.14}$$

such that

$$A^{\mathrm{sp}} = \frac{A}{1 - A/b}. \tag{2.2.15}$$

From Eq. 2.1.12, the polymer stress tensor then write

$$\tau_{ij}^{\mathrm{p}} = \frac{A_{ij}}{1 - A/b} - \delta_{ij}, \tag{2.2.16}$$

which is the expression of the polymer stress tensor of the FENE-P constitutive model. It is now clear, from the distribution of ρ_α^c, that the FENE-P model corresponds to the case where all the dumbbells in an infinitesimal volume element have the same extension.

Note that, using the same expression of the canonical radial probability density distribution, the radial dispersion of the dumbbells B can also be computed: $B = \alpha^4 = A^2$. The evolution equation for B is however useless as it is directly expressed as a function of A. Note also that the FENE-P model can be seen as a degenerate case of the FENE-P and FENE-LS$_0$ models where $\beta = 1$.

2.3 First numerical implementation

It is interesting to analyze the polymer response to simple flow configurations and in order to compute such a response, the polymer equations can be solved numerically. But before diving into more advanced numerical experiments, it is interesting to verify the implementation of the equations by comparing it with the same numerical results of the reference articles.

Two different kinds of flows are considered: a simple shear flow and a biaxial extensional flow. Note that in both configurations, the velocity gradient tensor is constant in space such that the problem is considered zero-dimensional. In fact, the different polymer variables only depend on time. Note also that in this case, the advective term disappear. Center-of-mass diffusion is thus not considered here since the problem has no spatial extent. Equation 2.0.3 becomes

$$\begin{cases} \dfrac{\partial A_{ij}}{\partial t} = \dot{\gamma}_{ik} A_{jk} + \dot{\gamma}_{jk} A_{ik} - \dfrac{1}{\mathrm{Wi}} \left(\dfrac{A^{\mathrm{sp}}}{A} A_{ij} - \delta_{ij} \right), \\ \dfrac{\partial B}{\partial t} = \dfrac{4B}{A} \dot{\gamma}_{ij} A_{ij} + \dfrac{1}{\mathrm{Wi}} \left(10A - 2B^{\mathrm{sp}} \right). \end{cases} \tag{2.3.1}$$

29

For obtaining the steady solution, the above equations are particularized by considering vanishing time derivatives and the system is solved numerically (for the FENE-L and FENE-LS only since an analytical solution is quite easy to derive for the FENE-P model). Alternatively, an explicit Runge-Kutta 4th order method have been implemented for integrating the above system of equations in time and obtaining the transient solution.

Note that the described numerical setup (system of equations and algorithm) is quite general an may be applied to any zero-dimensional Eulerian simulation (where the velocity gradient is constant in space but can vary in time) or to any Lagrangian simulation (since the advection term also disappear) as long as the center-of-mass diffusion is neglected. In fact, the only different inputs that will particularize this problem are: the kind of closure approximation chosen (to compute A^{sp} and B^{sp}), the different polymer parameters (Wi and b) and the imposed (time varying) velocity gradient tensor.

In order to compare the results with the ones of the reference article, it is important to mention that the non-dimensionalization performed in the reference is different from the one considered here, since the time and the velocity gradients are non-dimensionalized through the polymer time scale and not the flow time scale (as done in this work). The results will thus have to be adapted in order to be comparable and these adaptations are explained in App. A. One of the practical implication is that the shear (or elongation) rate of the reference plays the role of the Weissenberg number while the shear (or elongation) rate considered here is fixed to 1 (or 0 in relaxation). In the following of this section, the shear (or elongation) rate non-dimensionalized by the polymer time scale will thus be treated as the Weissenberg number Wi.

2.3.1   Simple shear flow

For the simple shear flow configuration, the velocity gradient is of the form

$$\dot{\boldsymbol{\gamma}} = \begin{bmatrix} 0 & \dot{\gamma} & 0 \\ 0 & 0 & 0 \\ 0 & 0 & 0 \end{bmatrix}, \tag{2.3.2}$$

where $\dot{\gamma}$ is the shear rate. The results are compared for the steady and transient cases (where the steady results are computed for various Wi). For the steady case, the quantities of interest are the shear viscosity and the first normal stress coefficient, noted η and N_1 respectively. Using the transformation from the appendix and the definitions of N_1 and η from the reference article, these may be expressed as

$$\begin{cases} N_1 = \dfrac{\tau_{11}^{\text{p}} - \tau_{22}^{\text{p}}}{\text{Wi}}, \\ \eta = \dfrac{\tau_{12}^{\text{p}}}{\text{Wi}^2}. \end{cases} \tag{2.3.3}$$

The results of the steady computations are shown in Fig. 2.3.1. As can be seen, these are very similar with the ones of the article, which gives confidence in the implementation of the different models. Note that the results of the FENE-L and FENE-LS$_1$

are confounded in practice such that the results of the FENE-LS$_1$ are not shown for readability.
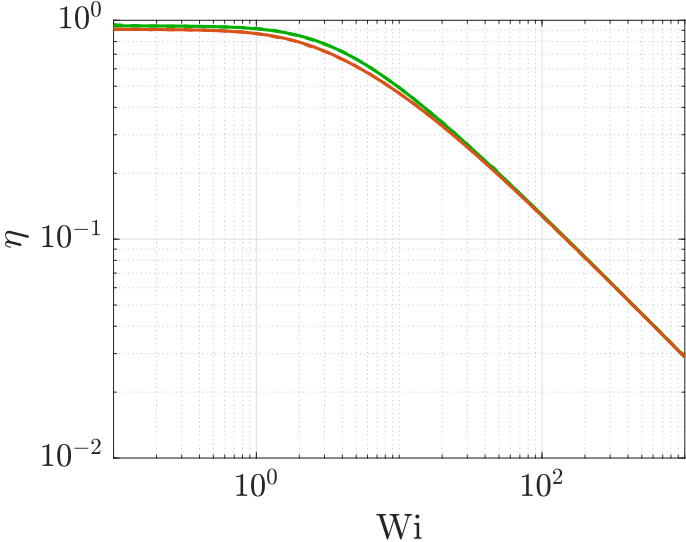
(a) Non-dimensional viscosity η.
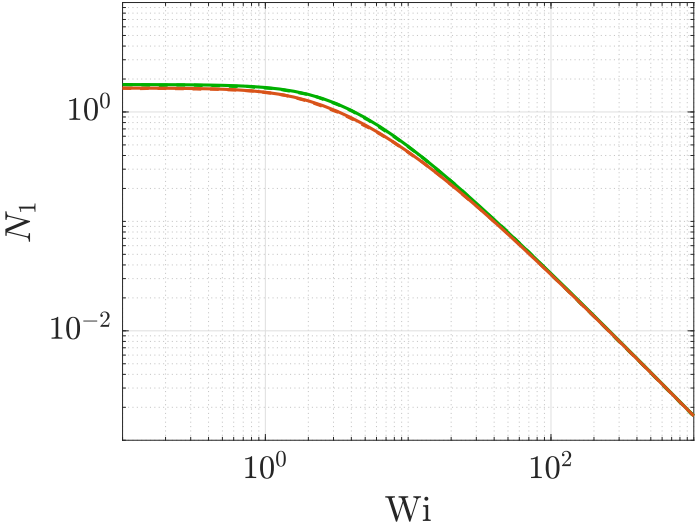
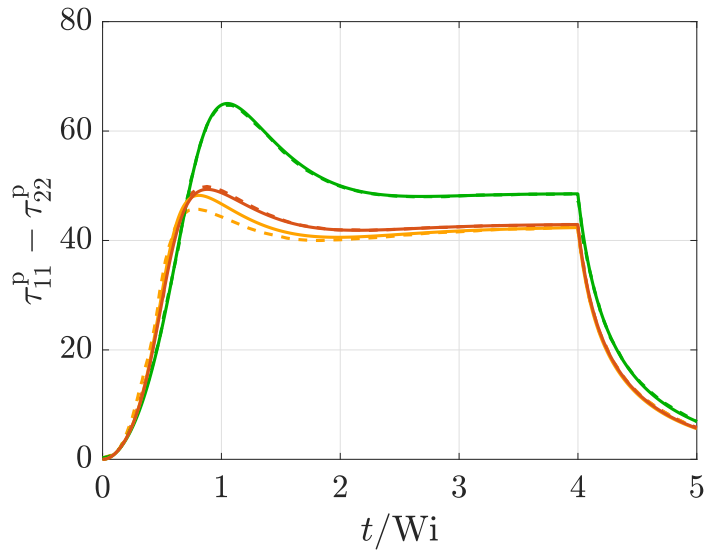(b) Non-dimensional first normal stress coefficient N_1.

Figure 2.3.1: Steady verification of the implementation. The results are visualized as a function of Wi, with $b = 50$. The results issued from the reference article are represented by dashed curves, while the results obtained from this work are shown as continuous curves. Both styles of curve are barely differentiable in the figures. FENE-P, green; FENE-L, red.

For the transient simulation, the system starts from the equilibrium and is then submitted to a constant shear rate ($\dot{\gamma} = 1$) from $t = 0$ to $t = 4$Wi, after which the system relaxes ($\dot{\gamma} = 0$) until $t = 5$Wi. The Weissenberg number is set to Wi = 10 (as the velocity gradient in the reference) and the numerical time step is set to 10^{-3}Wi. The results are

presented in Fig. 2.3.2 and as can be seen, these are still in good agreement with the ones of the reference article. Small differences have to be noted, but could potentially be explained by graphical errors introduced through the digitization process of the reference results. The present implementation thus seems quite correct. Note however that for the result of the first normal stress difference, a bigger difference is noticeable for the FENE-LS$_1$ at the stress overshoot. This difference could not be explained.
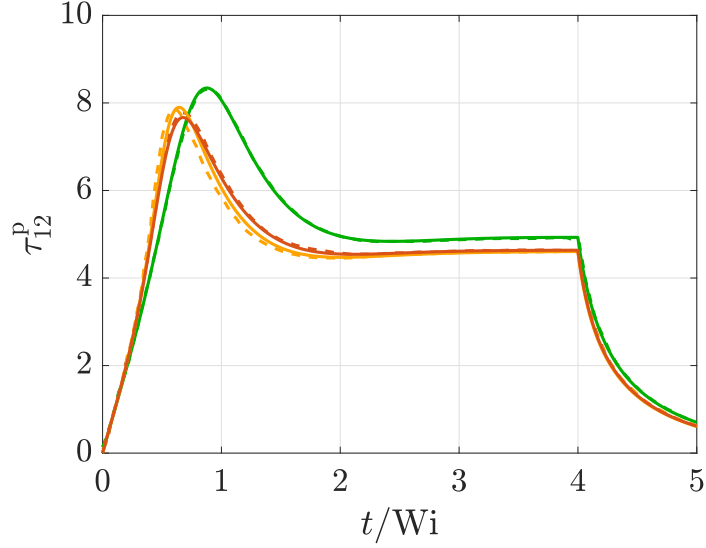
(a) Shear stress τ_{12}^{p}.

(b) First normal stress difference $\tau_{11}^{\mathrm{p}} - \tau_{22}^{\mathrm{p}}$.

Figure 2.3.2: Transient verification of the implementation. The shear stress τ_{12}^{p} and the first normal stress difference $\tau_{11}^{\mathrm{p}} - \tau_{22}^{\mathrm{p}}$ are visualized as a function of time (non-dimensionalized with the polymer time scale), with $b = 50$ and Wi $= 10$. The results issued from the reference article are represented by dashed curves, while the results obtained in the present work are shown as continuous curves. FENE-P, green; FENE-LS$_1$, orange; FENE-L, red.

However it is surprising to see that the results of the FENE-L seem to be in good agreement with the one of the reference article. In fact, as explained earlier, the expression of the closure approximation of the FENE-L appears to be false in the reference, such that the solution should be different than the one obtained here. In order to verify this, Fig. 2.3.3 illustrates the same transient experiment where the expression of the FENE-L was taken from the reference article. As can be seen, the result of the FENE-L model is now very different from the one of the article. This illustrates the fact that Lielens *et al.* did apparently not use the same expression as the one presented in the reference [7] for simulating this small numerical problem. Differences are noticeable as well for the steady simulation and for the first normal stress difference, but are not shown since it would not add any valuable information.
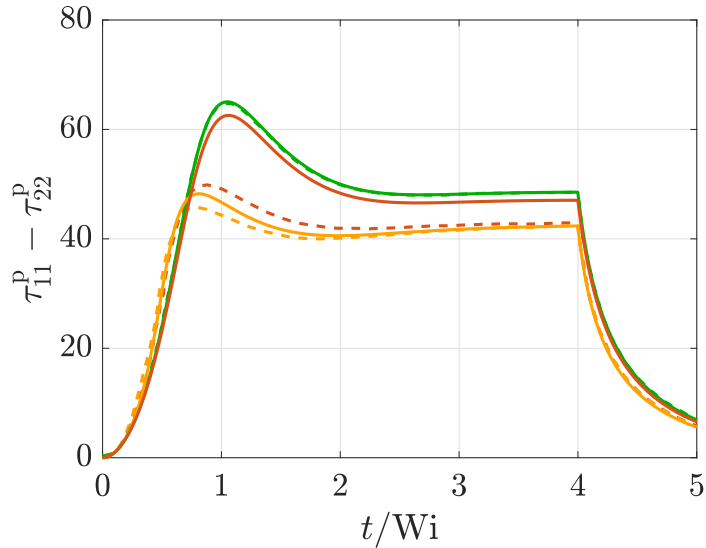
Figure 2.3.3: Same simulation as in Fig. 2.3.2b, by considering the expressions of the closure approximation of the reference article for the FENE-L model (see App. B for the precise expressions).

2.3.2 Biaxial extensional flow

For the biaxial extensional flow configuration, the velocity gradient is of the form

$$
\dot{\boldsymbol{\gamma}} = \begin{bmatrix} \dot{\varepsilon} & 0 & 0 \\ 0 & \dot{\varepsilon} & 0 \\ 0 & 0 & -2\dot{\varepsilon} \end{bmatrix}, \tag{2.3.4}
$$

where $\dot{\varepsilon}$ is the elongation rate.
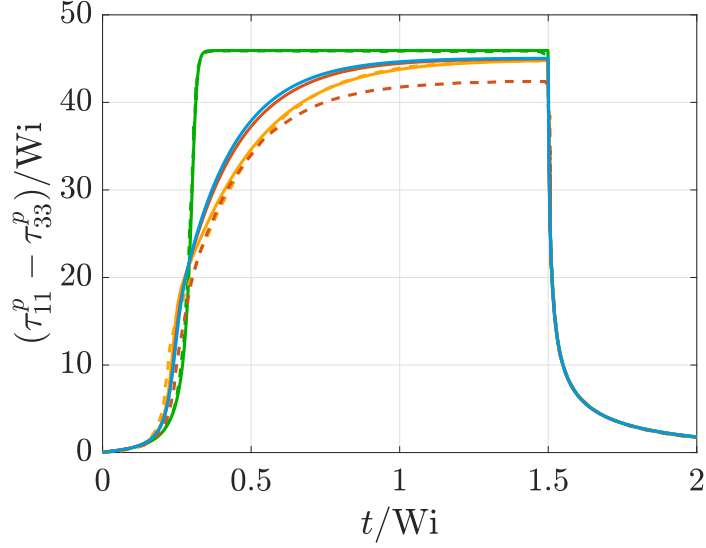
(a) Second normal stress difference $(\tau_{11}^{p} - \tau_{33}^{p})/\mathrm{Wi}$.

(b) Trace of the conformation tensor A.

Figure 2.3.4: Transient verification of the implementation. The second normal stress difference (divided by Wi) $(\tau_{11}^{p} - \tau_{33}^{p})/\mathrm{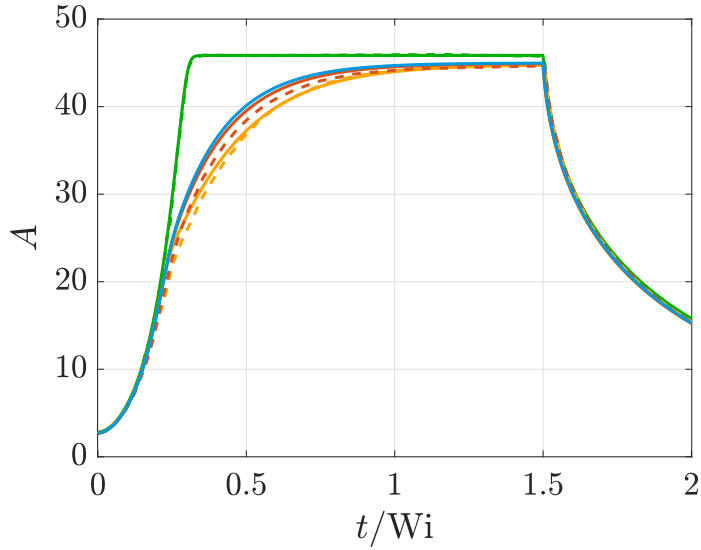Wi}$ and the mean square extension A are visualized as a function of time (non-dimensionalized with the polymer time scale), with $b = 50$ and $\mathrm{Wi} = 6$. The results issued from the reference article are represented by dashed curves, while the results obtained in the present work are shown as continuous curves. FENE-P, green; FENE-LS$_0$, blue; FENE-LS$_1$, orange; FENE-L, red.

Only the transient simulation is shown for this specific configuration. Again, the system starts from the equilibrium and is then submitted to a constant elongation rate ($\dot{\varepsilon} = 1$) from $t = 0$ to $t = 1.5\mathrm{Wi}$, after which the system relaxes ($\dot{\varepsilon} = 0$) until $t = 2\mathrm{Wi}$. The Weissenberg number is set to $\mathrm{Wi} = 6$ and the numerical time step to $10^{-4}\mathrm{Wi}$. The results are presented in Fig. 2.3.4 and as can be seen, these are again in quite good general agreements. Note however, that this is now the results of the FENE-L that seem

to deviate from the reference and this difference is more pronounced for the shear stress than for the mean square extension. Note that again, using the closure expression of the FENE-L presented in the reference yields to even more different results (not shown). This is again a very strange result that could not be explained. Still, even if it does not constitute a flawless justification, all the results obtained in this work seem to yield quite the same steady state value for all more advanced models (both for the simple shear and the biaxial extension), whereas the results obtained for the steady state value of the shear stress with the FENE-L in Fig. 2.3.4a significantly differ from the one of the FENE-LS$_1$ (and of the FENE-LS$_0$ that is shown here as a justification).

2.3.3 Larger b

The extensibility parameter b is quite small in the above simulations compared to the typical values it can takes for EIT or MDR simulations ($\mathcal{O}(10^2)$ bigger). The simple shear transient simulation is again performed for a larger value of b and the results are shown in Fig. 2.3.5. The evolution of the polymer stress is surprising for the FENE-LS$_1$ model as both results diverges during the relaxation period, while the other models seem to behave quite ordinarily[2]. Note moreover the similarity between the FENE-L and the FENE-LS$_0$ results, such that the advantage of distinguishing both FENE-LS submodels is now clear. This diverging behavior cannot be explained for now and thus motivates the need for a more detailed analysis of the properties of the different closure approximations.

---

[2]This phenomenon can also be observed for a biaxial extensional flow, but for different values of the parameters: Wi = 1, b = 450, with a period of extension of 4Wi. The results are not shown.
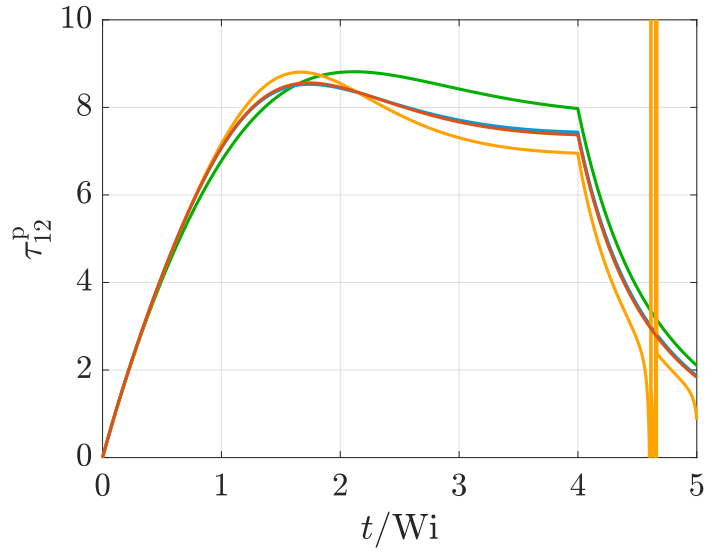
(a) Shear stress τ_{12}^{p}.
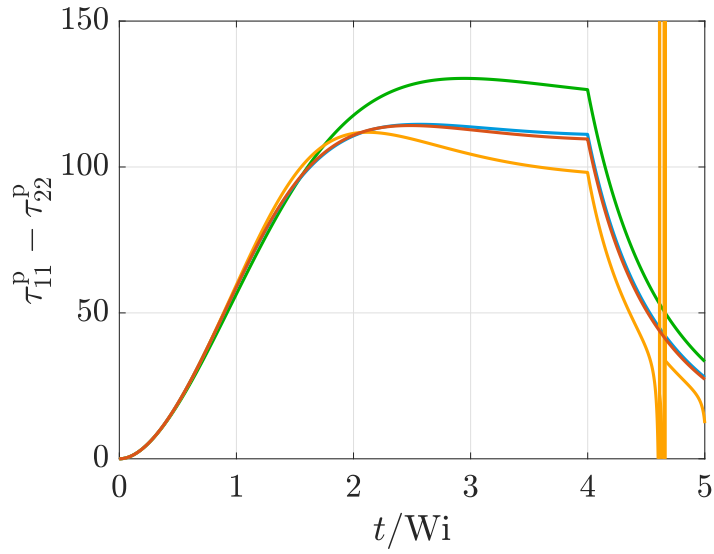
(b) First normal stress difference $\tau_{11}^{\mathrm{p}} - \tau_{22}^{\mathrm{p}}$.

Figure 2.3.5: Transient simulation of simple shear followed by relaxation for a larger b. The results are visualized as a function of the non-dimensional time t, with $b = 450$ and $\mathrm{Wi} = 10$. FENE-P, green; FENE-LS$_0$, blue; FENE-LS$_1$, orange; FENE-L, red.

Chapter 3

In-depth understanding of the FENE-L and FENE-LS models

The complexity of the present closure problem is that it typically involves two different spaces: the (α, β)-space and the (A, B)-space. In fact, the interesting physical interpretations mainly lie in the (α, β)-space as it gives direct insights on the radial probability distribution of the dumbbells $\rho^c_{\alpha,\beta}$. However, the problem is typically solved in the (A, B)-space which makes the mathematical developments sometimes easier in that space. In the end, both way of thinking and visualizing the data are useful and will be used throughout the following of this work. Note however that, as stated in the previous section, it makes no sense to try to understand the behavior of the FENE-LS$_1$ model in the (α, β)-space, such that its analysis will be limited to the (A, B)-space.

3.1 Boundaries of the domains and bijectivity

Since A and B are expressed as functions of α and β and that such parameters are restricted to a specific domain, it is obvious that A and B will also be restricted to some domain. The first step is then to determine the boundaries of the problem in the (A, B)-space but it is important to define some notations first. Fig. 3.1.1 represents the (α, β)-space with its different boundaries named b$_1$ ($\beta = 0$), b$_2$ ($\alpha = \sqrt{b}$), b$_3$ ($\beta = 1$) and b$_4$ ($\alpha = 0$). Note also the specific limit b$_\star$ at $\beta = 1/(R^2 + 1)$ which is not a boundary of the (α, β)-space, but will play a particular role.
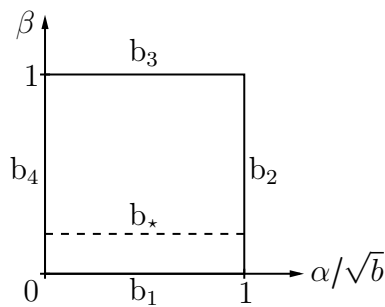

Figure 3.1.1: Representation of the boundaries in the (α, β)-space.

For each of the closure approximations, it is possible to consider the expressions $A = A(\alpha, \beta)$ and $B = B(\alpha, \beta)$ and eliminate α (resp. β) so that B can be expressed as a function of A and β (resp. α): $B = B(A, \beta)$ (resp. $B = B(A, \alpha)$). Then, since $\alpha \in [0, \sqrt{b}]$ and $\beta \in [0, 1]$, to each A can be associated a minimal and maximal B, which then forms the boundaries of the (A, B)-domain. This can be computed analytically and the expressions of the boundaries of each model are presented in App. C. These are also shown graphically in Fig. 3.1.2 in order to visualize them.

One can see that the boundary b_4 is degenerated into a single point in the (A, B)-space[1]. Also, the boundary b_3 is shared by all the closure approximations. This boundary is in fact a fundamental limit since it corresponds to a Dirac distribution located at $Q = \alpha$, which is the least dispersed distribution that could take place, corresponding thus to a minimum of B. As explained in Sec. 2.2.3, this boundary represents the admissible domain of the FENE-P closure approximation. It is also one of the fundamental limit of the general FENE model [6]. Moreover, the admissible domains of the FENE-L and FENE-L$_0$ models are exactly the same as shown by the envelope of the curves in Fig. 3.1.2. However, the mapping of the boundaries from the (α, β) to the (A, B)-space is not the same for both models. In fact, the boundary b_2 extends until b_3 for the FENE-LS$_0$ but stops when it crosses b_1 for the FENE-L. Also, the b_1 curves differ for both models (it is confounded with b_3 for the FENE-LS$_0$), but yet, the boundaries b_1 (FENE-L) and $b_\star$ are the same. Finally, an interesting thing is the apparition of $b_\star$ as a boundary in the (A, B)-space although it is not a boundary in the (α, β)-space.

Having now a better understanding of the admissible values for A and B, it is possible to discuss in more details the case of the natural and ghost solutions. For the FENE-L closure approximation, one can show that for the ghost solution, $\tilde{\beta} < 0$. In fact,

$$\tilde{\beta} = \frac{(9A^2 - 5B) - \sqrt{(9A^2 - 5B)9A^2}}{10B} = \frac{\sqrt{9A^2 - 5B}}{10B} \left(\sqrt{9A^2 - 5B} - \sqrt{9A^2} \right) \qquad (3.1.1)$$

with the expression inside of the parenthesis being always negative. Also, from the expression of b_1, note that $9A^2 - 5B \geq 0 \Leftrightarrow B \leq B_1$ (where B_1 corresponds to the expression of B on the curve b_1). This means that, imposing that the argument of the square root is positive is equivalent to impose that the solution cannot cross the b_1 boundary. Alternatively, one quickly understands that $\overline{\beta} \geq 0$. In order to prove that $\overline{\beta} \leq 1$, one can see that the maximum of $\overline{\beta}$ occurs when B is minimized. Knowing that the minimal value of B is $B_3 = A^2$, one well recovers that the maximum value of $\overline{\beta}$ is 1. The same kind of reasoning can be done for proving that $\overline{\alpha} \in [0, \sqrt{b}]$. The ghost solution is then unphysical whereas the natural solution is totally appropriate. The ghost solution can thus be rejected and the transformation between the (A, B) and (α, β)-space becomes a one-to-one mapping so that there is no more ambiguity in what solution choosing.

---

[1]It seems logical since this boundary corresponds to a zero extension and a Dirac located at $Q = 0$. Note that potential problems could arise on b_4 since, for $(A, B) = (0, 0)$, the value that the solution would take in the (α, β)-space is ambiguous. However, this boundary is a non-physical extreme case and not too much care should be given to it.
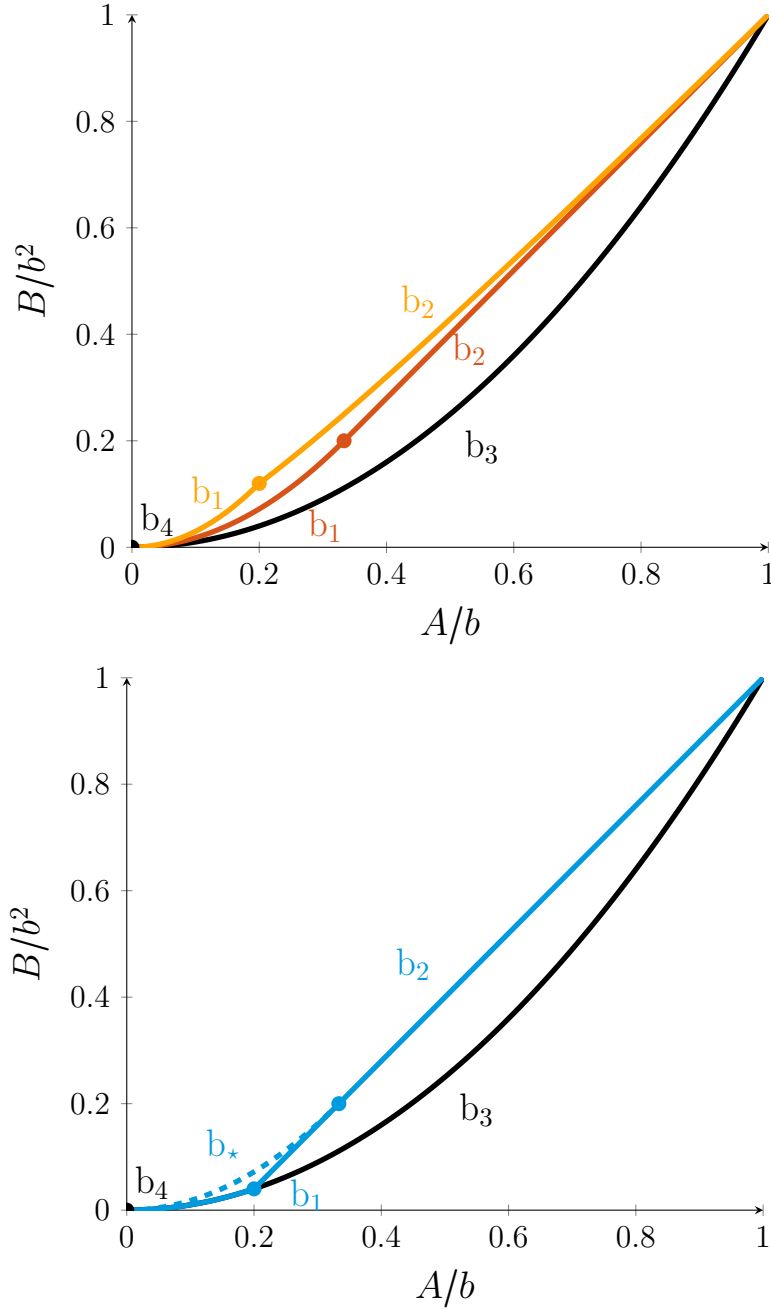
Figure 3.1.2: Comparison of the different boundaries in the (A, B)-space for each of the closure approximations. The domain of the FENE-LS$_0$ closure is presented in a separated figure as several curves are the same as for the FENE-L. The admissible domain of a model is represented by the envelope of all the curves (including the b$_\star$ boundary for the FENE-LS$_0$). FENE-L, red; FENE-LS$_1$, orange; FENE-LS$_0$, blue.

This is quite different for the FENE-LS$_0$ closure model. In fact, using again the same kind of procedure, one can show that $\tilde{\beta} \in [0, 1/(R^2 + 1)]$ and $\overline{\beta} \in [1/(R^2 + 1), 1]$[2] such that both solutions lead to appropriate values of β. However, it is not true for α since $\overline{\alpha} \in [0, \sqrt{b}]$ but some admissible values of (A, B) can yield $\tilde{\alpha} > \sqrt{b}$, such that

---

[2]The line b$_\star$ in the (α, β)-space delimits the admissible domains of the natural and ghost solutions.

only the natural solution makes sense for these values. A more detailed analysis shows that for values of (A, B) lying between the curves b_2 and b_3, the ghost solution yields $\tilde{\alpha} > \sqrt{b}$. In this region, the result is as for the FENE-L since the ambiguity is not present anymore and only the natural solution is considered. However, for values of (A, B) that lie inside of the curvilinear triangle defined by the curves b_1, b_2 and $b_\star$, both solutions exist and make sense such that the ambiguity persists.

For the FENE-LS$_0$, the fact that one couple (A, B) can potentially lead to two admissible couples $(\overline{\alpha}, \overline{\beta})$ and $(\tilde{\alpha}, \tilde{\beta})$ could have been anticipated. In fact, $\rho^c_{\alpha, \beta}$ is composed of two Dirac distributions: $(1-\beta)\delta_{\alpha/R}$ and $\beta\delta_\alpha$ and one can check that the special cases $(\beta = 0, \alpha = \alpha' R)$ and $(\beta = 1, \alpha = \alpha')$ yield the exact same distribution, that is $\rho^c_{\alpha, \beta} = \delta_{\alpha'}$. Moreover, note that these special cases correspond respectively to the boundaries b_1 and b_3, which shows why these are confounded.

In general, the fact that two admissible solutions (α, β) exist for a given (A, B) cannot be explained exclusively by the fact that the same probability distribution can be reached by different sets of parameters (α, β). The converse is however true as if different sets of (α, β) lead to the same $\rho^c_{\alpha, \beta}$, it will necessary lead to the same (A, B) and $(A^{\mathrm{sp}}, B^{\mathrm{sp}})$ by extension.

3.2 Permeability of the boundaries in pure relaxation

In order to understand the problem arising with the FENE-LS$_1$ closure approximation that was shown in Fig. 2.3.5, it is useful to try to analyze how the solution evolves in the (A, B)-space. Such a trajectory is shown in Fig. 3.2.1. As can be seen, it appears that at some point, the solution computed from the FENE-LS$_1$ model leaves its admissible domain and as it does, the numerical solution behave in a very random and unpredictable way. Note however that the solutions issued from the FENE-L and FENE-LS$_0$ models totally stay in their admissible domain (which upper bound is the dashed curve in Fig. 3.2.1).

The problem being solved numerically, such phenomena are frequent and often associated to a bad time discretization or a bad integration scheme. In fact, if the solution approaches a given boundary and that the time step is *too large*, it is possible for the solution to cross the boundary, thus leading to non-physical results[3]. However here, the solution keeps crossing the boundary at the exact same location no matter how small the time step is, which suggests that the problem does not come from a bad time discretization, but that the analytical solution itself tends to leave its admissible space.

Moreover, note that this problem appears when the imposed shear rate is zero (when the system relaxes back to equilibrium). This scenario is however a very fundamental mechanism and should not lead to any issue, such that it could illustrate a potential intrinsic problem with the model. An analytical investigation of the mathematical problem is necessary to seek whether the boundaries are permeable analytically or not. What is meant by *permeable* is the fact that when the solution tends toward a boundary from the inside of the domain, the evolution vector is oriented in such a way that the

---

[3]Such problems mainly occur with explicit time stepping methods and implicit time stepping algorithms usually remove such issues. One should keep in mind that the problem is solved numerically by considering an explicit time stepping method in this case (Runge-Kutta 4th order).
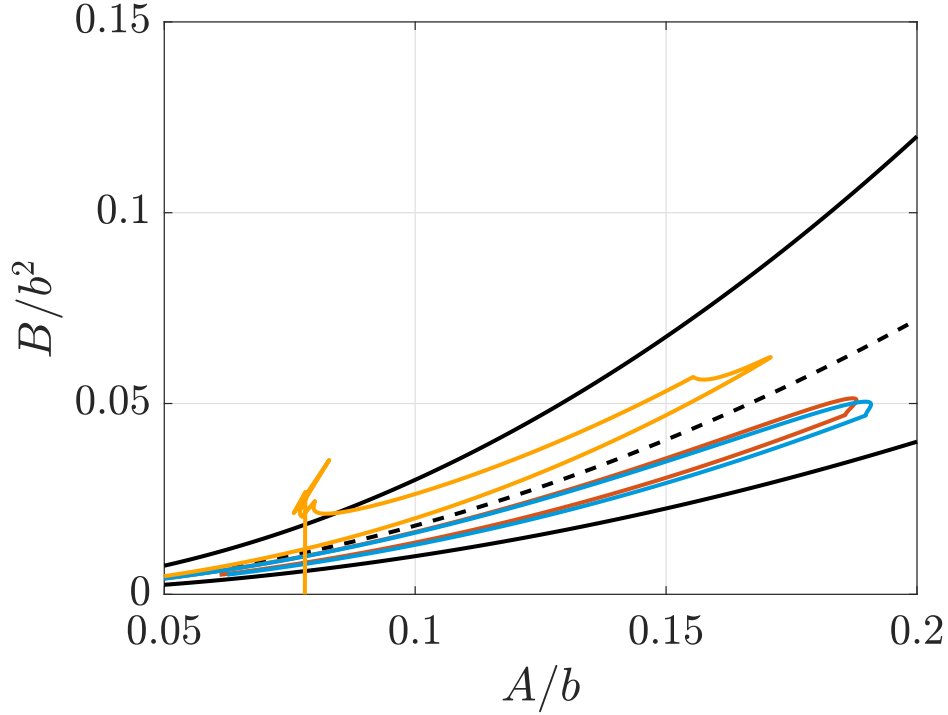
solution naturally crosses the boundary.

Figure 3.2.1: Comparison of the evolution of the solution in the (A, B)-space between the FENE-LS$_0$, FENE-LS$_1$ and FENE-L closure approximations. The parameters are the same as in Fig. 2.3.5. The plot is a zoom of the boundaries presented in Fig. 3.1.2, where the dashed curve corresponds to the boundary b$_\star$, the top continuous black curve to the boundary b$_1$ of the FENE-LS$_1$ and the bottom continuous black curve to the boundary b$_3$. FENE-L, red; FENE-LS$_0$, blue; FENE-LS$_1$, orange.

In order to understand whether it is possible or not for the evolution vector to make the solution leave its domain, it is necessary to check whether it points inward or outward of the domain. To do so, one can analyze the sign of the scalar product between e.g. the inward normal vector of the boundary curves and the evolution vector evaluated at the same boundaries, such that a negative scalar product would make the solution leave its domain.

Considering a given boundary b$_i$ and the associated quantities B_i, α_i, β_i, A_i^{sp} and B_i^{sp}, the inward normal to this boundary (in the (A, B)-space) is noted $\boldsymbol{n}_i$ and expressed as

$$\boldsymbol{n}_i(A) = \pm \frac{1}{\sqrt{1 + \left(\frac{\mathrm{d}B_i}{\mathrm{d}A}\right)^2}} \begin{pmatrix} -\frac{\mathrm{d}B_i}{\mathrm{d}A} \\ 1 \end{pmatrix} \propto^4 \pm \begin{pmatrix} -\frac{\mathrm{d}B_i}{\mathrm{d}A} \\ 1 \end{pmatrix}, \tag{3.2.1}$$

where the '+' sign has to be chosen for the lower boundaries (b$_3$) and the '−' sign has to be chosen for the upper boundaries (b$_1$ and b$_2$ for the FENE-L and FENE-LS$_1$, but b$_\star$

---

[4]Note that the normalizing function $[1 + (\mathrm{d}B_i/\mathrm{d}A)^2]^{-1/2}$ is always strictly positive and bounded (the slope of the boundaries are never infinite here), such that one can simply hide it behind a proportionality factor, since it won't influence the sign of the dot product.

and b_2 for the FENE-LS$_0$) in order to choose the inward normal. The evolution vector is noted $\boldsymbol{X}$ and is defined as

$$\boldsymbol{X} = \begin{pmatrix} \mathrm{D}A/\mathrm{D}t \\ \mathrm{D}B/\mathrm{D}t \end{pmatrix}, \tag{3.2.2}$$

with the notation $\boldsymbol{X}_i$ referring to the evolution vector evaluated at the boundary b_i.

In order to compute the expression of the evolution vector, one needs to obtain an equation for A. Taking the trace of the equation for the conformation tensor (Eq. 2.1.11) yields

$$\begin{cases} \dfrac{\mathrm{D}A}{\mathrm{D}t} - 2\dot{\gamma}_{ij}A_{ij} = \dfrac{1}{\mathrm{Wi}}\left(3 - A^{\mathrm{sp}}\right) + \dfrac{1}{\mathrm{Pe}}\dfrac{\partial^2 A}{\partial x_k \partial x_k}, \\ \dfrac{\mathrm{D}B}{\mathrm{D}t} - \dfrac{4B}{A}\dot{\gamma}_{ij}A_{ij} = \dfrac{1}{\mathrm{Wi}}\left(10A - 2B^{\mathrm{sp}}\right) + \dfrac{1}{\mathrm{Pe}}\dfrac{\partial^2 B}{\partial x_k \partial x_k}, \end{cases} \tag{3.2.3}$$

which is the general system of equations for A and B, considering the drag term as well as the center-of-mass diffusion.

Since the departure of the solution from its domain seems to happen without diffusion and even in relaxation, the stretching and the center-of-mass diffusion terms are not considered. Also, since the advective terms vanish for the two simple problems that were considered, the above system simplifies to

$$\begin{cases} \dfrac{\partial A}{\partial t} = \dfrac{1}{\mathrm{Wi}}\left(3 - A^{\mathrm{sp}}\right), \\ \dfrac{\partial B}{\partial t} = \dfrac{1}{\mathrm{Wi}}\left(10A - 2B^{\mathrm{sp}}\right). \end{cases} \tag{3.2.4}$$

In this context, the scalar product becomes

$$\begin{aligned} \boldsymbol{X}_i \cdot \boldsymbol{n}_i &= \pm \frac{1}{\mathrm{Wi}} \frac{1}{\sqrt{1 + \left(\frac{\mathrm{d}B_i}{\mathrm{d}A}\right)^2}} \left[10A - 2B_i^{\mathrm{sp}} + \frac{\mathrm{d}B_i}{\mathrm{d}A}\left(A_i^{\mathrm{sp}} - 3\right)\right] \\ &\propto \pm \left[10A - 2B_i^{\mathrm{sp}} + \frac{\mathrm{d}B_i}{\mathrm{d}A}\left(A_i^{\mathrm{sp}} - 3\right)\right]. \end{aligned} \tag{3.2.5}$$

Note that $\boldsymbol{X}_i \cdot \boldsymbol{n}_i$ generally varies along a boundary such that in order to study its sign along all the curve, it should be expressed as a function of A[5]. The major difficulty of this analysis will thus be to systematically express the closure terms A^{sp} and B^{sp} as functions of A for each of the boundary considered. Only the final conclusions are provided since it would be quite heavy to show the hole developments.

3.2.1 FENE-LS$_1$

The boundary b_3 is impermeable, as for the boundary b_2. Note however that the later is somewhat special since the norm of the evolution vector tends toward ∞, but its

---

[5]It is also possible to express the dot product as a function of α or β (mainly for the FENE-L or FENE-LS$_0$ models). Though, it is less general since the fact that the dot product is expressed as a function of α or β depends on the boundary considered. It is however still an appropriate option as it sometimes facilitates the mathematical evaluation of some terms, such it has also been used in practice for the computations.

orientation still tends to make the solution come back into its domain. It is different for the boundary b_1 since it is

$$
\begin{cases}
\text{impermeable for} \quad A \in \left[0, \dfrac{3R^2 - 7}{R^2 - 1}\right] = [0, 2], \\[4mm]
\text{permeable for} \quad A > \dfrac{3R^2 - 7}{R^2 - 1} = 2,
\end{cases}
\tag{3.2.6}
$$

considering $R^2 = 5$. An interesting remark is that B_1 is defined for $A \in [0, b/R^2]$ (see App. C), such that the length of the permeable zone (from 2 to b/R^2) depends on the value of b. In fact, if $b \leq 2R^2 = 10$ the boundary b_1 is not permeable at all. However, as b increases, the length of the permeable zone defined as the portion of b_1 between $A = 2$ and $A = b/R^2$ grows. For large extensibility parameters, the boundary b_1 is nearly totally permeable (relative to its total domain) making this model unsuitable for large b.

Note however that the limit $b = 10$ is in practice very small such that it is not suitable for the vast majority of applications. Note also that since it is possible to reach b_1 within the simple case of a constant applied shear rate (and biaxial extensions) followed by relaxation, it is very likely that it can be reached for any more complex shearing history. In fact, the ultimate goal being to apply such kind of closure approximations to turbulent flows where the evolution of the velocity gradients are chaotic and quite difficult to predict, it is likely to encounter a velocity gradient history that makes the solution leave its admissible domain.

It is difficult to precisely assess what makes the b_1 boundary of that domain permeable, but one could argue that the different mathematical simplifications made the closure approximation lose its physical consistency. The fact that this model fails in such a simple test case makes it non-applicable to more complex flows and it will thus simply not be used nor analyzed anymore in the following of this work. The focus will be on the FENE-L and the FENE-LS$_0$ closure approximations.

3.2.2 FENE-L and FENE-LS$_0$

The results are qualitatively the same for both models. In fact, all the boundaries are impermeable. Note that on the boundary b_2 the norm of the evolution vector tends toward ∞ but is again oriented toward the interior of the domain. In general, the fact that the boundary b_2 seems unreachable can be understood from the shape of $\rho^c_{\alpha,\beta}$ on that boundary. In fact, on b_2, $\alpha = \sqrt{b}$ which is the largest value it can take, so that for all three models, the radial canonical probability distribution presents a Dirac at the maximum extensibility. This means that the dumbbells do have a non-vanishing probability of reaching their maximal extension. However, one should keep in mind that for a FENE dumbbell, the force needed to extend the dumbbell to its maximal extension is infinite, or said differently, it is impossible to reach the maximal extension so that the radial probability distribution should go to 0 as Q tends to $\sqrt{b}$. For these particular canonical distribution, it corresponds to the fact that α cannot reach $\sqrt{b}$.

As already mentioned, the boundary b_3 corresponds to a single Dirac distribution located at $Q = \alpha$, which is also an extreme case. This being also an extreme case for the general FENE model, the boundary can thus naturally not be crossed. Finally, note

that since the boundaries b_1 (for the FENE-L) and $b_\star$ (for the FENE-LS$_0$) cannot be crossed, the conditions for the square roots in the expressions of α and β are always satisfied without the need of an additional constraint, in relaxation at least.

3.3 Permeability of the boundaries for arbitrary velocity gradients

In order to study more complex problems, it is possible to analyze how could the impermeable boundaries react under the action of arbitrary velocity gradients. Only neglecting the diffusion terms in Eq. 3.2.3 and keeping a general velocity gradient tensor as well as the material derivative, it yields

$$\begin{cases} \dfrac{\mathrm{D}A}{\mathrm{D}t} - 2\dot{\gamma}_{ij}A_{ij} = \dfrac{1}{\mathrm{Wi}}\left(3 - A^{\mathrm{sp}}\right), \\ \dfrac{\mathrm{D}B}{\mathrm{D}t} - \dfrac{4B}{A}\dot{\gamma}_{ij}A_{ij} = \dfrac{1}{\mathrm{Wi}}\left(10A - 2B^{\mathrm{sp}}\right). \end{cases} \tag{3.3.1}$$

In this system, the stretching term is quite similar for both equations such that the velocity gradient term can be eliminated. It yields the relation

$$\frac{\mathrm{D}B}{\mathrm{D}t} = \frac{2B}{A}\frac{\mathrm{D}A}{\mathrm{D}t} + \frac{1}{\mathrm{Wi}}\left(10A - 2B^{\mathrm{sp}} + \frac{2B}{A}\left(A^{\mathrm{sp}} - 3\right)\right) \tag{3.3.2}$$

such that for any $\dot{\boldsymbol{\gamma}}$, $\mathrm{D}B/\mathrm{D}t$ can be expressed as a function of $\mathrm{D}A/\mathrm{D}t$. In general, the dot product between the inward normal and the evolution vector writes

$$\boldsymbol{X}_i \cdot \boldsymbol{n}_i \propto \pm \left[\frac{\mathrm{D}B_i}{\mathrm{D}t} - \frac{\mathrm{d}B_i}{\mathrm{d}A}\frac{\mathrm{D}A}{\mathrm{D}t}\right] \tag{3.3.3}$$

and using the above relation (Eq. 3.3.2):

$$\boldsymbol{X}_i \cdot \boldsymbol{n}_i \propto \pm \left[\left(\frac{2B_i}{A} - \frac{\mathrm{d}B_i}{\mathrm{d}A}\right)\frac{\mathrm{D}A}{\mathrm{D}t} + \frac{1}{\mathrm{Wi}}\left(10A - 2B_i^{\mathrm{sp}} + \frac{2B_i}{A}\left(A_i^{\mathrm{sp}} - 3\right)\right)\right]. \tag{3.3.4}$$

An interesting observation is the fact that the boundaries b_3 and b_1 (for the FENE-L) or $b_\star$ (for the FENE-LS$_0$) are quadratic in A (from App. C). On these curves, one can thus write $B_i = c_i A^2$ (with c_i a multiplicative constant which may differ from one curve to another). Notice then that on these boundaries,

$$\frac{\mathrm{d}B_i}{\mathrm{d}A} = 2c_i A = \frac{2B_i}{A}, \tag{3.3.5}$$

such that the above equation simplifies to

$$\boldsymbol{X}_i \cdot \boldsymbol{n}_i \propto \pm \left[10A - 2B_i^{\mathrm{sp}} + \frac{\mathrm{d}B_i}{\mathrm{d}A}\left(A_i^{\mathrm{sp}} - 3\right)\right], \tag{3.3.6}$$

which is the exact same expression that for the relaxation case (Eq. 3.2.5). This is a very powerful result since the fact of adding an arbitrary stretching to the equations does not change the permeability properties of the considered boundaries, which are then still impermeable.

For the b_2 boundary, since the relation $B_2(A)$ is not quadratic, the same simplification does not hold such that DA/Dt does not vanish. Using the expression of DA/Dt from Eq. 3.3.1 the dot product becomes

$$\boldsymbol{X}_i \cdot \boldsymbol{n}_i \propto \pm \left[2 \left(\frac{2B_i}{A} - \frac{dB_i}{dA} \right) \dot{\gamma}_{ij} A_{ij} + \frac{1}{\text{Wi}} \left(10A - 2B_i^{\text{sp}} + \frac{dB_i}{dA} \left(A_i^{\text{sp}} - 3 \right) \right) \right]. \qquad (3.3.7)$$

Again, this is very similar to the results obtained for pure relaxation. More precisely, the first term is the stretching term whereas the second one is proportional to the relaxation term of Eq. 3.2.5. The term multiplying $\dot{\gamma}_{ij} A_{ij}$ being finite, if neither the velocity gradient nor the conformation tensor are infinite, the stretching term is bounded on b_2. However, since the relaxation term tends to ∞ on b_2, the results are exactly those of the pure relaxation (taking the limit of the solution going to b_2) no matter the velocity gradient. This means that b_2 is also impermeable whatever the action of the fluid on the polymers.

The fact that all the boundaries of the solution are impermeable is a very strong results. It proves that both the FENE-L and the FENE-LS$_0$ closure approximations are consistent and can be used for solving dilute polymer solutions for any kind of flow. Note however, that until now, the center of mass diffusion of the dumbbells was neglected. Even if this is a very reasonable assumption from a physical point of view, this term is generally artificially amplified in numerical simulations in order to stabilize the non-linear advection term. Since the ultimate goal is to solve the coupled Eulerian equations numerically, it is important to analyze the impact of the diffusion as well. This analysis is done in Chap. 4.

Finally, as already mentioned the fact that all boundaries of the FENE-L and FENE-LS$_0$ model are always impervious directly imposes the positivity of the argument of the square root in the expression of α and β. It means that, contrary to what has been exposed by Lielens *et al.* [6, 7], there is no need for an additional restriction on the values of B. The fact, that such a condition is needed in the simulations of the first article deriving the FENE-L closure approximation [6] probably comes from the suspected errors in the expression of A^{sp} and B^{sp} (as explained in Sec. 2.2.1). In fact, the same permeability analysis has been performed considering the same closure expressions as in the reference articles and the results showed that the boundary b_1 was in fact permeable for some values of A.

3.4 Interpretation of zero-dimensional flow results

Now that the properties and limits of the models are more clear, and moreover, since it has been demonstrated that the boundaries of the FENE-L and FENE-LS$_0$ are impermeable, it is interesting to analyze and understand the polymer response to simple zero-dimensional flows. Three major kinds of flow have been investigated: the simple shear, the uniaxial and the biaxial extensional flow. Note that in such cases, the equations and the numerical setup considered in Sec. 2.3 are still valid. The specific forms of the velocity gradient tensor applied to the simple shear and biaxial extensional flow configurations have already been described in Eq. 2.3.2 and 2.3.4. For the uniaxial

extensional flow, one has

$$\dot{\boldsymbol{\gamma}} = \begin{bmatrix} \dot{\varepsilon} & 0 & 0 \\ 0 & -\frac{\dot{\varepsilon}}{2} & 0 \\ 0 & 0 & -\frac{\dot{\varepsilon}}{2} \end{bmatrix}, \tag{3.4.1}$$

where $\dot{\varepsilon}$ is the elongation rate (as for the biaxial extensional flow).

Note that in order to consider more realistic polymer parameters, one chooses Wi = 50, $b = 2500$ (such parameters typically correspond to the EIT phenomenon).

3.4.1 Inception of flow followed by relaxation

(a) Simple shear flow.

(b) Simple shear flow.

(c) Biaxial extensional flow.
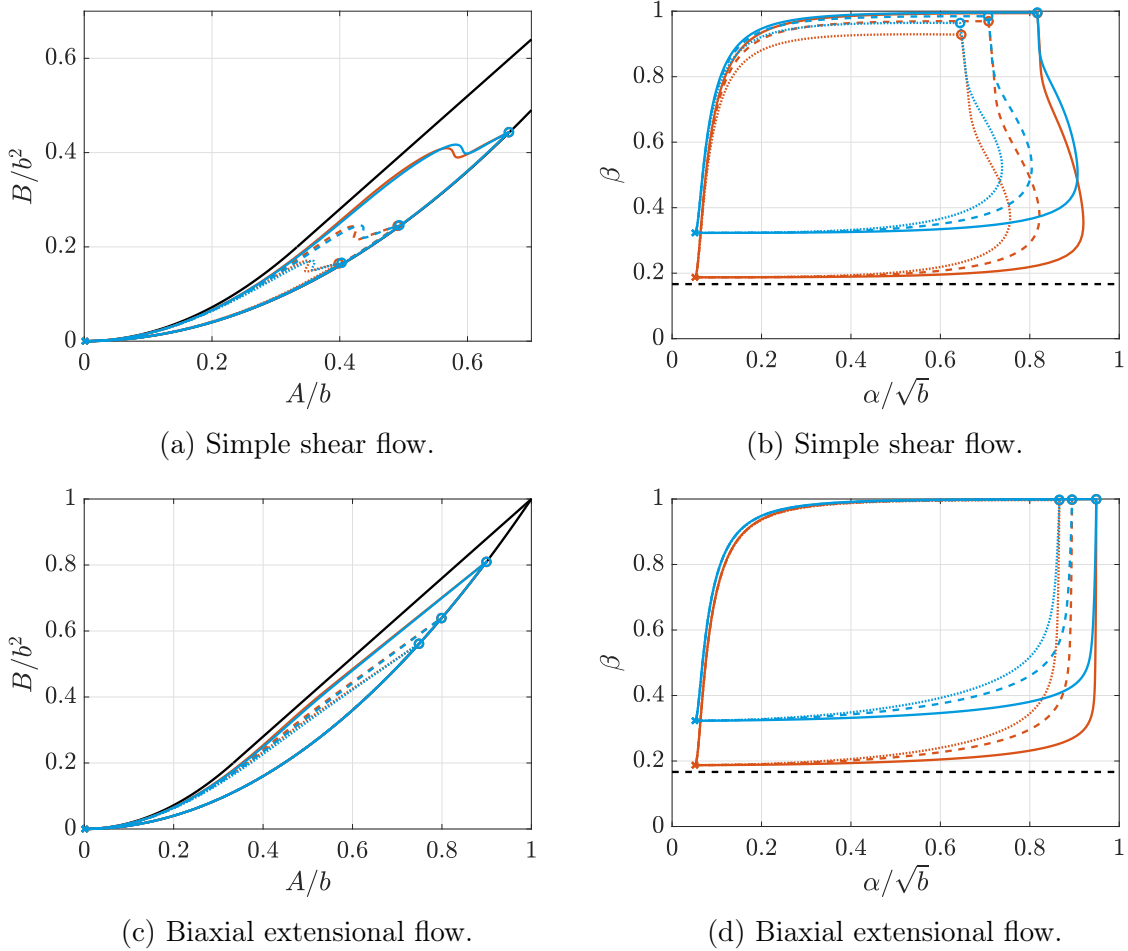
(d) Biaxial extensional flow.

Figure 3.4.1: Visualization of the polymer response when submitted to the inception of specific zero-dimensional flows followed by relaxation. The initial condition is denoted by the symbol × and the steady solution is denoted by the symbol ∘. The curves are traveled clockwise in the (A, B) representation, but anti-clockwise in the (α, β)-space. The line style refers to the flow intensity: low intensity, dotted curves; medium intensity, dashed curves; high intensity, continuous curves. Alternatively, the color refers to the constitutive model considered: FENE-LS$_0$, blue; FENE-L, red.

First, one considers a system that starts at equilibrium and that is submitted to a constant velocity gradient tensor from $t = 0$ to $t = 10$Wi and then relaxes back ($\dot{\boldsymbol{\gamma}} = \mathbf{0}$)

until $t = 20$Wi. For each kind of flow, three different velocity gradient intensities are considered. For the simple shear flow, one has $\dot{\gamma} = 1$, $\dot{\gamma} = 1.4$ and $\dot{\gamma} = 3$ and for the uniaxial and biaxial extensional flow, one has $\dot{\varepsilon} = 0.04$, $\dot{\varepsilon} = 0.05$ and $\dot{\varepsilon} = 0.1$. Note that for both extensional flows, the velocity gradient has a significantly larger impact on the polymers, such that it is important to reduce the time step of the simulation (recall that an explicit time stepping method is used). In fact, for the simple shear flow, the numerical time step is 10^{-3}Wi, whereas for the extensional flows, the time step is 10^{-4}Wi. An important remark is that no matter how large the velocity gradient is, it seems to be always possible to find a sufficiently small numerical time step in order for the solution to remain physical[6] (for these simple flows at least). Indeed, this shows that the boundaries seem impermeable, as theoretically anticipated.

Different results from the simulation are shown. The evolution of the solution in the (A, B) and (α, β)-space is presented in Fig. 3.4.1 and the evolution of some components of the polymer stress tensor are presented in Fig. 3.4.2. Since the results of both extensional flows were very similar, only the biaxial extensional flow case is presented.

Analyzing the evolution of the solution in the (A, B) or (α, β)-space, the first observation is the similarity of the FENE-L and the FENE-LS closure approximation. This is very clear in the (A, B)-space representation as both curves are barely distinguishable for the extensional flow and only slightly differ at some point before reaching their steady state value for the simple shear flow. Another difference between both models is more noticeable in the (α, β)-space representation as the solution of the FENE-LS$_0$ seems to be squeezed along β between $1/(R^2+1)$ and 1, when compared to the FENE-L. This seems however totally logical as, since only the natural solution has been chosen for the FENE-LS$_0$, its admissible domain lies between $\beta = 1/(R^2 + 1)$ and $\beta = 1$.

Another interesting remark is the fact for the simple shear flow, the steady state values of both models are different but get closer as the shear rate increases (this is well illustrated in Fig. 3.4.1b). An intuitive explanation to this phenomenon is that when the polymers are highly stretched, their radial probability density distribution tends toward a Dirac distribution (all the dumbbells inside a fluid elements have the same extension). Since the Dirac distribution is inside the canonical set of distributions Φ^c of both models, in the limit where the radial probability density distribution of the FENE model becomes a single Dirac, both models are exact. Note also that the boundary b$_3$ (which is the lower curve in the (A, B)-space and the upper boundary in the (α, β)-space) is the admissible domain of the FENE-P model, such that in the limit of large and steady shear, all the models are similar (including the FENE-P).

As already mentioned, the (α, β) representation is more suited to the physical understanding of the polymers behavior as it directly relates to the canonical radial probability distribution $\rho^c_{\alpha, \beta}$. In fact, the polymers start by extending without significantly changing the shape of $\rho^c_{\alpha, \beta}$, as β is more or less constant in the beginning. This means that some polymers start to extend but others keep a rather small length. As α more or less reaches its peak, β starts to increase, meaning that the large polymers stop extending while the smaller continue to be stretched. For the simple shear, one can see that α even decreases, such that the more extended polymers becomes slowly less extended as the less extended polymers extend. Eventually, provided that the polymers

---

[6]This was tested for simple shear flows with values of the shear rate as big as $\dot{\gamma} = 100$.

are sufficiently stretched by the flow (sufficiently high $\dot{\gamma}$), β tends toward 1, such that the radial probability distribution nearly becomes a Dirac distribution meaning that all the polymers are extended and approximately reaches the same extension. It is even simpler for the extensional flows as α monotonously grows until the solution reaches $\beta = 1$ and all the polymers are evenly extended. In fact, even for the smaller elongation rates, it seems that the steady solution lies on $\beta = 1$, but one should realize that this is obviously not true for all $\dot{\varepsilon}$ as in the limit $\dot{\varepsilon} = 0$, the equilibrium solution is recovered (very different from $\beta = 1$). The fact that all models tend to reach the b_3 boundary for steady flows points out why the FENE-P closure approximation is apparently sufficient for describing simple steady flow configurations.

In the relaxation phase, this is first α then β that decays. This means that the dumbbells all start by being less and less extended but still keep more or less the same extension between each other and only when their extension is sufficiently low, some dumbbells stop while other keep shortening, until the equilibrium radial probability distribution is reached.

Finally, it is interesting to note that the polymers seems to react in a quite similar way to three different and fundamental velocity gradient tensors.

As was already the case for the biaxial extensional flow in Fig. 3.4.1, the polymer stress curves of the FENE-L and FENE-LS$_0$ are barely distinguishable and the differences are more significant for the simple shear flow, even though the results are again very similar between both models. Note that for the normal stress difference[7], the difference between the FENE-P and the more advanced models is as expected, as the FENE-L and FENE-LS$_0$ solutions exhibit an hysteresis, whereas the FENE-P solution does not. The idea that the hysteretic behavior of the FENE cannot be reproduced by the FENE-P model originates from the results of the one-dimensional Fokker-Planck equation [5]. When generalizing such theory in a three-dimensional configurational space Ω, one should be careful as it is not true for all components of the stress tensor separately. In fact, Fig. 3.4.2b shows that the polymer shear stress obtained with the FENE-P is also not a one-to-one function of the mean square extension. The fundamental difference between the one-dimensional and the three-dimensional theories is the fact that the relationship between the stress and the conformation is now a tensorial relation: $\boldsymbol{\tau}^{\mathrm{p}} = \boldsymbol{\tau}^{\mathrm{p}}(\boldsymbol{A})$, whereas it was a simple scalar relation in the case of the one-dimensional study. Looking at the relation between one particular stress component e.g. τ_{12}^{p} and one particular conformation component e.g. A is not sufficient anymore to characterize the ability of a model to present an hysteresis.

The previous discussion for the (A, B) and (α, β) trajectories however holds for the stress tensor as the steady state values of the polymer stress (any component) seem to be quite similar for all models. Another clear observation is that the polymer stress versus mean square extension curve is very similar for all models (even for the shear stress) in relaxation after having reached the steady state solution. This could have been anticipated from Fig. 3.4.1 since as already seen, all solutions nearly follow b_3 after having reached their steady state values, such that the values of $\boldsymbol{A}$ and A^{sp} are more or less the same for all models and the same is true for the polymer stress tensor.

---

[7]Following the definition of the velocity gradient for the biaxial extensional flow, only the second normal stress difference is non zero.

As already explained several times, it is now clear that the differences between the FENE-P and the more advanced closure models occurs only in unsteady flows.

(a) Simple shear flow.

(b) Simple shear flow.
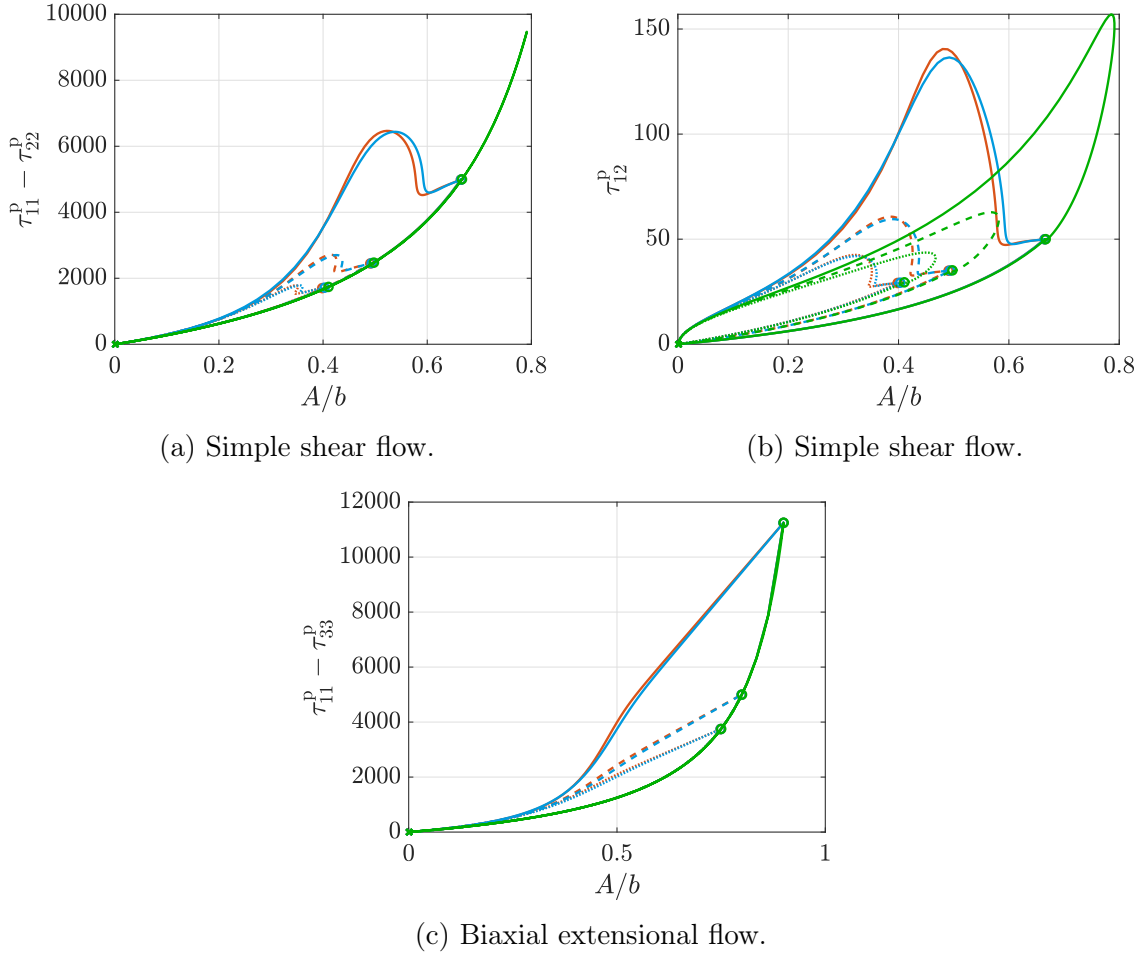
(c) Biaxial extensional flow.

Figure 3.4.2: Visualization of the polymer stress response as a function of the mean square extension when submitted to the inception of specific zero-dimensional flows followed by relaxation. The curves are traveled clockwise. The meanings of the line styles and colors corresponds to the ones of Fig. 3.4.1. The FENE-P stress response is added in green.

3.4.2 Periodic excitation

In all the previous numerical experiments, the polymer were stretched and relaxed only once and for a sufficiently long time such that the steady state solution could be reached. Even if it gives interesting insight about the physics of the system, it is quite a limited flow configuration. In fact, in real turbulent flow, the polymers are likely to be submitted to rapid velocity gradients changes without having time to reach any steady state solution. It is thus interesting to analyze the results of a time varying flow excitation.

In this case, the system is first submitted to a constant velocity gradient in order to reach a steady state solution, after which the shear or elongation rate will start to oscillate. Since the results of the extensional flows do not add any new information,

the focus is on simple shear here. From $t = 0$ to $t = 10\text{Wi}$, one imposes $\dot{\gamma} = 3$ such that the system can be considered to have reached steady state. Then the shear rate start to oscillate from $t = 10\text{Wi}$ to $t = 20\text{Wi}$ as

$$\dot{\gamma}(t) = -3\sin\left(2\pi f \frac{t}{10\text{Wi}}\right), \tag{3.4.2}$$

where f is the frequency of the oscillations. Note that since 10Wi is the time during which the system is oscillating, f is also the number of entire cycles performed.

Figure 3.4.3 shows the solutions for $f = 4$ and $f = 100$. The trajectory in the (α, β)-space illustrates that all the models again yield the same solution once the steady state value is reached as $\beta \approx 1$. This is true even for quite fast time varying shear rates ($f = 100$). The stress tensors computed from each models are also very similar between each other and it is interesting to see that the polymer shear stress reaches a limit cycle oscillation, which is then the same for all three models considered. Note that only the (α, β) representation and the shear stress versus means square extension are shown because the other figures (first normal stress difference and (A, B) trajectories) are redundant.

(a) $f = 4$.

(b) $f = 4$.

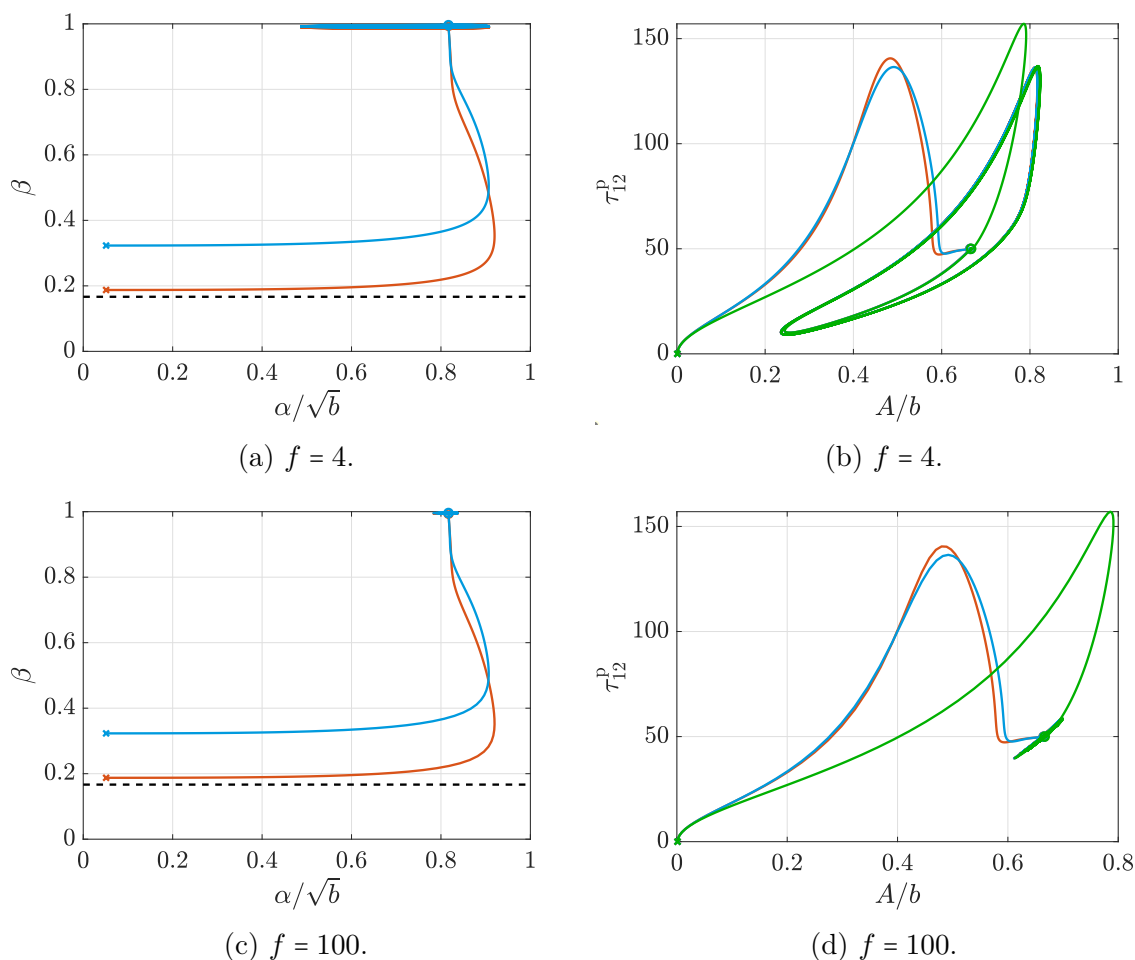(c) $f = 100$.

(d) $f = 100$.

Figure 3.4.3: Visualization of the polymer response when submitted to an oscillating simple shear flow. The curves of Fig. 3.4.3b and 3.4.3d are traveled clockwise. The meanings of the line styles and colors corresponds to the ones of Fig. 3.4.2.

It seems that once the solution reaches the boundary b_3 (FENE-P domain), it cannot significantly deviate from it. There is however an infinite amount of possible velocity gradient history and it is difficult to make an extensive study of all the possible case. A better understanding of the behavior of the different models will be made possible by considering turbulent velocity gradient histories in Sec. 5.3.

3.5 One-dimensional channel flow simulation

In order to come closer to a real channel flow configuration, a steady one-dimensional channel flow simulation is considered in this section. In fact, making the assumption that the flow variables may only vary along z (except for the pressure that may also vary along x in order to drive the flow) and considering vanishing spanwise and wall normal velocity, the unique relevant momentum equation becomes (from Eq. 1.3.15)

$$\frac{\partial u}{\partial t} = \frac{3}{\mathrm{Re}} + \frac{\varepsilon}{\mathrm{Re}} \frac{\partial^2 u}{\partial z^2} + \frac{1 - \varepsilon}{\mathrm{Re}} \frac{\partial \tau_{13}^{\mathrm{p}}}{\partial z}, \tag{3.5.1}$$

where the streamwise pressure gradient has been fixed to $-3/\mathrm{Re}$ in order to obtain a bulk velocity of 1 in the steady Newtonian limit.

One should pay attention to the fact that the wall normal coordinate is noted z and not y as often considered in the literature. As already explained, the concentration parameter is a coupling parameter between the solvent and the polymers equations. If $\varepsilon = 0$, the fluid is a polymer melt and if $\varepsilon = 1$, the equations are one-way coupled. In practical flow applications involving dilute polymer solutions, the concentration parameters is often fairly high: $\varepsilon \approx 0.9 - 1$.

From a practical point of view, in order to solve the hole system of equations (complex fluid and polymers), the velocity gradient needs to be evaluated and used in the polymers equations. In this simple one-dimensional case, the velocity gradient is computed as

$$\dot{\boldsymbol{\gamma}} = \begin{bmatrix} 0 & 0 & \dot{\gamma} \\ 0 & 0 & 0 \\ 0 & 0 & 0 \end{bmatrix}, \quad \text{with} \quad \dot{\gamma} = \frac{\partial u}{\partial z}. \tag{3.5.2}$$

Again, one should pay attention to the fact that the velocity gradient does not have the exact same shape as in Eq. 2.3.2. Also, the boundary conditions for the velocity are no-slip boundary conditions at the channel walls ($z = \pm 1$). The polymers equations do not need any boundary condition in the case where center-of-mass diffusion is neglected. However, if diffusion is considered, boundary conditions generally have to be chosen at both walls and for all the polymers variables. Instead of doing this, one rather neglects diffusion on the very edges of the channel, such that the equations are local at these points and no boundary condition is required. Note that the treatment of the boundary conditions for the polymers constitutive equations is still an open question.

Time marching is used for computing the steady solution, starting at equilibrium and considering a 4th order explicit Runge-Kutta time integration method. The different derivatives (needed for computing the shear rate, the divergence of the polymer stress tensor and the center-of-mass diffusion terms of $\boldsymbol{A}$ and B) are evaluated using finite differences, with a 4th order central scheme both for the first and second derivatives.

Finally note that 80 evenly distributed discrete points are considered along z for all the following computations.

In order to build up the complexity progressively, the solution is first computed by considering the one-way coupled equations ($\varepsilon = 1$). Also, center-of-mass diffusion is still not considered initially since, the flow being completely laminar, there is not much need for added diffusion (from a numerical point of view). In this specific case, the polymer variables depend on the wall normal coordinate, but only through the local velocity gradient. In fact, the diffusive term could make a variable at one point in space influence its neighbors and similarly, the two-way coupled system would make the polymers influence the flow through the gradient of the polymer stress which would then influence back the polymer neighbors. That being not the case at first, the problem is equivalent to a zero-dimensional simple shear problem where the applied shear rate is simply a function of the position.
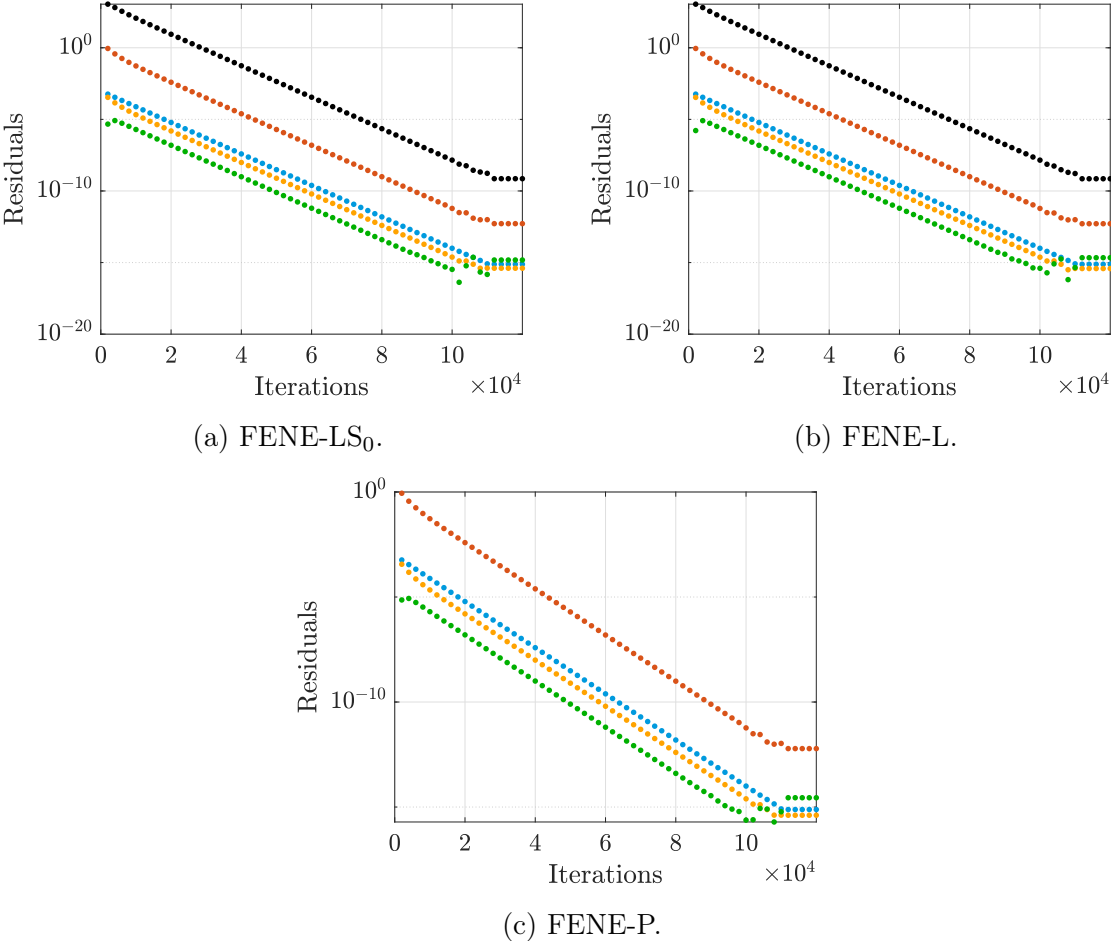

(a) FENE-LS$_0$.

(b) FENE-L.

(c) FENE-P.

Figure 3.5.1: Residuals of different relevant variables as a function of the number of iterations. B, black; A_{11}, red; A_{33}, orange; A_{13}, green; u, blue.

In order to assess the accuracy of the numerical solution, the residuals of the different variables can be computed. These are calculated as the (discrete) integrals over the channel of the evaluated time derivatives of each relevant variable (right-hand side of

each equation). The residuals are however not normalized such that the important information is the relative decay of the residual and not its absolute magnitude. The results are shown in Fig. 3.5.1. As can be seen, the solutions obtained for all models are converged as the residuals decay of at least 10 orders of magnitude for all the relevant variables, before stalling.

Figure 3.5.2 shows the profiles of different polymer quantities. The first thing to notice is the similarity of all the closure approximations. As was already explained in the previous section, all models tend to be equivalent for steady simple flow configurations and this is verified here. Then, an interesting phenomenon is the fact that the channel center is the point where the polymer solution changes the fastest contrary to the well know parabolic velocity profile of a channel flow. The fact that all the polymer variables seem to vanish at $z = 0$ can be explained by the fact that at this point, the shear rate is zero, such that the solution is exactly the equilibrium solution. To be precise, $\tau_{11}^{\mathrm{p}} - \tau_{33}^{\mathrm{p}}$ and τ_{13}^{p} both vanishes, but A and B do not exactly vanish as their equilibrium values are not 0.

(a) Mean square extension A.

(b) Radial dispersion B.

(c) First normal stress difference $\tau_{11}^{\mathrm{p}} - \tau_{33}^{\mathrm{p}}$.

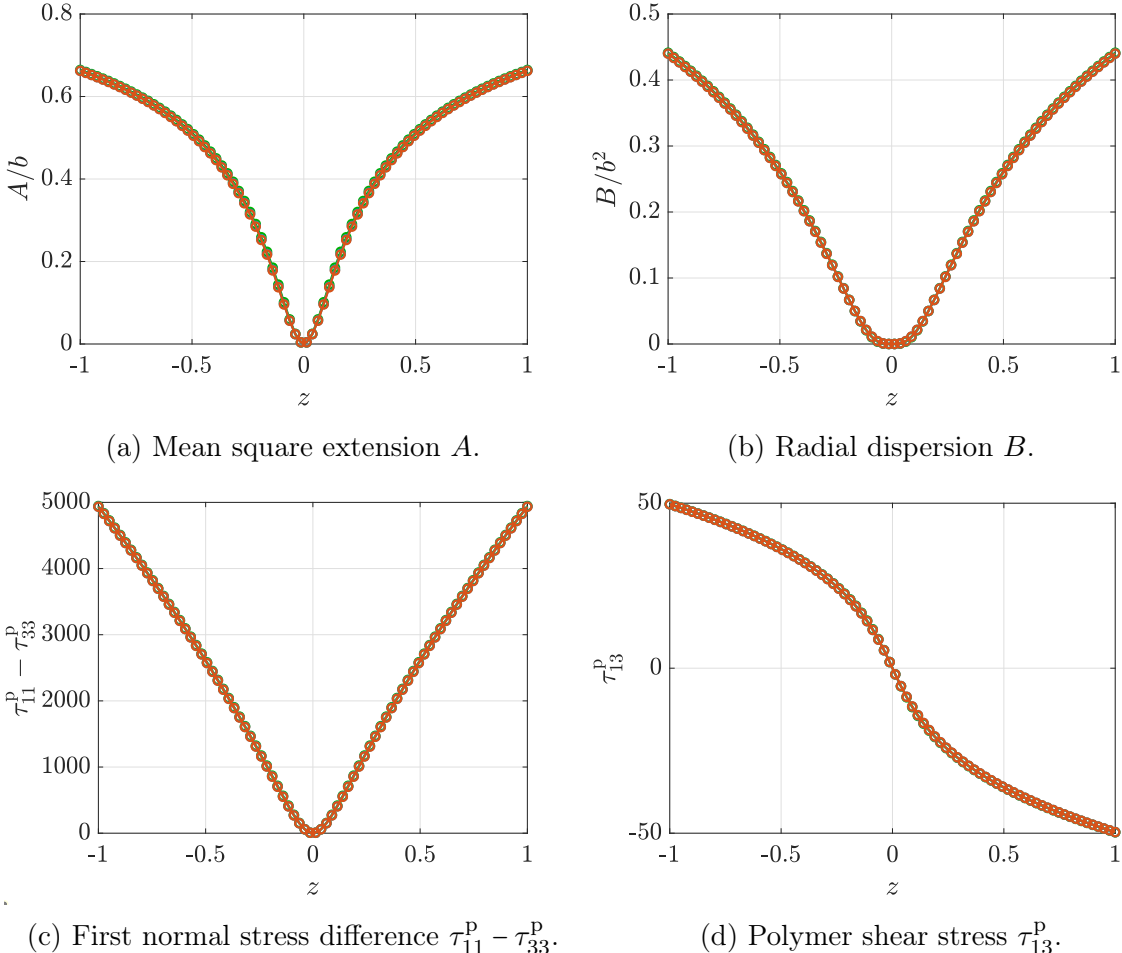(d) Polymer shear stress τ_{13}^{p}.

Figure 3.5.2: Steady solution of the one way coupled channel flow problem, where the profiles of different relevant polymer variables are shown. Each figure is composed of three curves (one for each model), but these are barely differentiable. FENE-LS$_0$, blue; FENE-L, red; FENE-P, green.

Figure 3.5.3 shows the same solutions in the (A, B) and (α, β)-space. The (A, B)-representation leads to the same conclusion as above in the sense that all models seem to approximately reach b_3, which is also the domain of the FENE-P. An interesting observation can however be made from Fig. 3.5.3b as one can see that the values of (α, β) are quite different (even at steady-state) for all models at the channel center. This could have been anticipated from the results of the previous section as the equilibrium values (α_0, β_0) of all models are quite different (such that at the channel center, (α, β) are different for all models). Note however, that only the very central points exhibits such high differences and as can be seen in Fig. 3.5.2, this does not seem to have any significant impact on the shear stress or on the polymer quantities.

One should also understand that since the A and B profiles are symmetrical, the same holds for α and β, such that each point of Fig. 3.5.3a–3.5.3b in fact represents two symmetric points of the channel.

(a) (A, B)-representation.

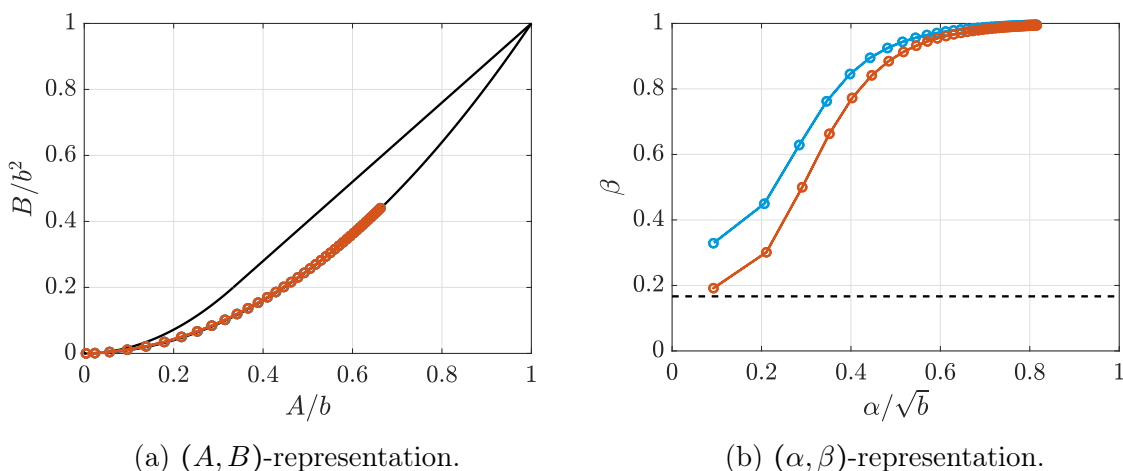(b) (α, β)-representation.

Figure 3.5.3: Steady solution of the one way coupled channel flow problem presented in the (A, B) and (α, β)-space. The curves of Fig. 3.5.3a are again barely differentiable. FENE-LS$_0$, blue; FENE-L, red.

In order to analyze the impact of the coupling on the final solution, two coupled simulations are considered, with $\varepsilon = 0.90$ and $\varepsilon = 0.95$. The impact of this *weak coupling*[8] being quite limited, it is rather the relative difference between the two-way coupled and the one-way coupled simulation that is investigated. This relative difference is computed as

$$X' = \frac{X_\varepsilon - X}{\max(X)}, \tag{3.5.3}$$

where X' is the relative difference of the solution, X is the solution computed with $\varepsilon = 1$ and X_ε denotes the solution obtained for a given concentration parameter ε. Figure 3.5.4 shows the relative differences between the FENE-L and FENE-P constitutive models only as the results are very similar for the FENE-LS$_0$.

The first thing that can be seen is that the center of the channel is left unmodified by the coupling of the equations. In fact, the differences between the one-way and two-way

---

[8]The term *weak coupling* is to be understood in the sense that the concentration parameter is quite high. It however corresponds to the typical values considered for dilute polymer solutions.

(a) Mean square extension A'.

(b) Radial dispersion B'.

(c) First normal stress difference $(\tau_{11}^{\mathrm{p}} - \tau_{33}^{\mathrm{p}})'$.

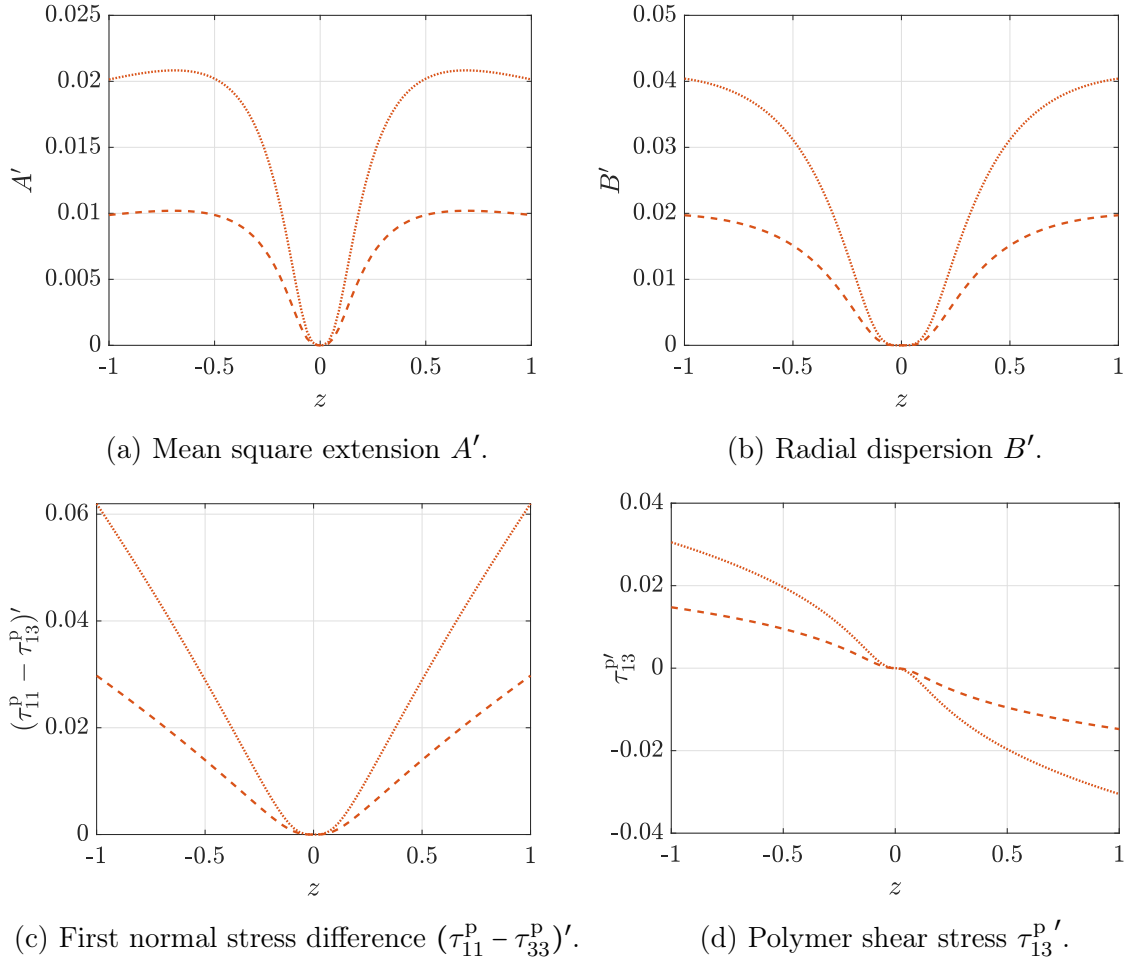(d) Polymer shear stress $\tau_{13}^{\mathrm{p}\,\prime}$.

Figure 3.5.4: Relative difference between the steady solutions of the FENE-L and the FENE-P models obtained with $\varepsilon = 0.95$ and $\varepsilon = 0.9$ and the one-way coupled solution ($\varepsilon = 1$). The discrete marker indicators $\circ$ are not shown for readability. $\varepsilon = 0.95$, dashed line; $\varepsilon = 0.9$, dotted line.

coupled equations are mainly located near the edges of the channel, but this constitutes the largest part in practice. One should notice the interesting behavior of the mean square extension A, that seems to present an overshoot near the walls. In fact, for $\varepsilon = 1$, the maximum of A is located at the wall, while for smaller concentration parameters this maximum is shifted inside of the channel. Finally, the maximum relative difference between the one-way and two-way coupled solution is about 6% (for the first normal stress difference), which is quite small.

The last complexity step of this problem is to add center-of-mass diffusion. One should recall that the influence of the diffusive terms are controlled by the Peclet number: the lower the Peclet number is, the more center-of-mass diffusion is taken into account in the equations. Typical values of the Peclet number in real flows are about 10^6. However, it is often massively decreased in practice for balancing the non-linear advective term.

In this case, diffusion can however lead to unwanted effects. In fact, as the Peclet number decreases, the solution at the channel center leaves its admissible domain at

some point, by crossing the b_1 boundary for the FENE-L or the $b_\star$ boundary for the FENE-LS$_0$. Again, note that this problematic phenomenon is not associated to a bad numerical resolution. Several different methods were in fact considered without altering the behavior of the solution: smaller time steps, finer spatial discretization, higher order derivatives evaluation, slowly decaying Peclet number (starting from the above steady solution without center-of-mass diffusion), and others. This problem is analyzed in details in the next chapter.

Chapter 4

Diffusion problem

Even if diffusion has the effect of damping the perturbations and smoothing the extrema of the variables, it seems to bring complexity in this precise case. This is quite unexpected since, as already mentioned several times, diffusion usually tends to make things more stable numerically.

It is useful to try to understand what could arise when diffusion is added. The very first effect is the smoothing (in space) of the different polymer variables. Said differently, no maximum can be created nor amplified when diffusion is added to the problem. In the (A, B)-space, it means that the solution cannot extend further to the left (resp. right) than the minimal (resp. maximal) value and the same holds for the top and the bottom. However, it is possible for a point at a specific location to be shifted to the top/bottom/left/right depending on the position of its neighbors, as long as it does not create a new maximum.

Particularizing the diffusion to the channel flow configuration, one can already anticipate what could happen at the center of the channel: the results of the previous chapter show that the curvature of A and B at the channel center are positive, such that the addition of diffusion will increase both values. This corresponds to a translation of the lower extension point to the top-right in the (A, B)-space.

This is in fact what happens in practice when diffusion is added. However, the impact of diffusion seems to be stronger on B such that the lower extension point is more shifted up than right. When center-of-mass diffusion becomes too important, or said differently, when the Peclet number becomes too small, it can have the effect of making that point cross the boundary $b_\star$ (or b_1 for the FENE-L) and thus leave its admissible space. Note also that this boundary corresponds to the zone where the argument of the square root in the expression of α and β becomes negative. In fact, when the solution crosses that boundary, α and β become complex.

Numerical experiments showed that the crossing of that boundary does not only appear when the polymers are submitted to a shear rate (e.g. when the channel flow develops), but it can also happen in relaxation. Again, the permeability of the boundaries is thus questionable and it is interesting to analyze the impact of the diffusion from an analytical point of view.

4.1 Permeability of the boundaries with diffusion

In order to study this phenomenon, the same kind of procedure than what was done for the relaxation and the stretching can be followed for the diffusion. In order to simplify the developments it will however only be done for the case of pure relaxation, as it was numerically shown that it can be sufficient for boundary permeability.

From Eq. 3.2.3, only the stretching term is thus ignored, which gives the equations

$$
\begin{cases}
\dfrac{\partial A}{\partial t} = \dfrac{1}{\mathrm{Wi}}\left(3 - A^{\mathrm{sp}}\right) + \dfrac{1}{\mathrm{Pe}}\dfrac{\partial^2 A}{\partial x_k \partial x_k}, \\[2mm]
\dfrac{\partial B}{\partial t} = \dfrac{1}{\mathrm{Wi}}\left(10A - 2B^{\mathrm{sp}}\right) + \dfrac{1}{\mathrm{Pe}}\dfrac{\partial^2 B}{\partial x_k \partial x_k}
\end{cases}
\tag{4.1.1}
$$

and considering an arbitrary boundary i, the dot product becomes

$$
\boldsymbol{X}_i \cdot \boldsymbol{n}_i \propto \pm\left[\frac{1}{\mathrm{Wi}}\left(10A - 2B_i^{\mathrm{sp}} - \frac{\mathrm{d}B_i}{\mathrm{d}A}\left(3 - A_i^{\mathrm{sp}}\right)\right) + \frac{1}{\mathrm{Pe}}\left(\frac{\partial^2 B_i}{\partial x_k \partial x_k} - \frac{\mathrm{d}B_i}{\mathrm{d}A}\frac{\partial^2 A_i}{\partial x_k \partial x_k}\right)\right].
\tag{4.1.2}
$$

One well recognizes the first term as it is the same as for pure relaxation. Also the second term is the diffusive one, such that if $\mathrm{Pe} \to +\infty$, the pure relaxation result is recovered. From the above simple and general result, it is already possible to draw two conclusions. First, if one assumes that the profiles of A and B are sufficiently smooth, their Laplacian is bounded and since the norm of $\boldsymbol{X}$ tends toward $+\infty$ at b_2 for pure relaxation, the impact of diffusion (compared to relaxation) vanishes at b_2. Diffusion will thus have no impact on the permeability of b_2. Moreover, the permeability of the other boundaries will be determined by the sign and the magnitude of the second term. However, note that more or less nothing can be said about the sign of that term since it depends on the second derivative of the solution around the point of interest, which completely depends on the specific flow configuration.

In order to better understand the reasoning, the expression of the scalar product can be particularized to a specific model and a specific boundary. The FENE-LS$_0$ closure approximation and the boundary b_3 are chosen here because of the simplicity of the expression of the relaxation term, but it could be extended to the FENE-L model and/or to the $b_1/b_\star$ boundary. In this specific case, the dot product becomes

$$
\boldsymbol{X}_i \cdot \boldsymbol{n}_i \propto \frac{4A}{\mathrm{Wi}} + \frac{1}{\mathrm{Pe}}\left(\frac{\partial^2 B}{\partial x_k \partial x_k} - 2A\frac{\partial^2 A}{\partial x_k \partial x_k}\right).
\tag{4.1.3}
$$

In order for this boundary to become permeable, the diffusive term needs to be negative and the Peclet number sufficiently low. The fact of having a negative diffusive term corresponds to having a sufficiently high curvature of A compared to the one of B. In parallel, having a low Peclet number corresponds to having a relatively large center-of-mass diffusion. However, as already said, such reasoning is not really helpful in the sense that there is no condition on the values that the second derivative may take at a given point, such that these are left unspecified.

Since the analysis in the (A, B)-space does not lead to any significantly better understanding, it could be interesting to make this analysis in the (α, β)-space. Note also that the admissible domain in this space is rectangular such that classical diffusion[1]

---

[1] *Classical diffusion* is to be understood in the sense that the diffusive term is a simple Laplacian of the variable of interest.

on α and β could not make the solution leave the space. Also it is easier to analyze whether the solution leaves the domain or not since it is sufficient to look only at the sign of $D\alpha/Dt$ or $D\beta/Dt$ (depending on the boundary) and there is no need to compute the dot product. The difficulty will therefore lie in the inversion of the system and the expression of each terms as functions of α and β.

4.2   Equations in the (α, β)-space

In order to perform the permeability analysis in the (α, β)-space, the first step is to transform the evolution equations for A and B into evolution equations for α and β. Note that in order to remain general, the stretching and center-of-mass diffusion terms are considered as well as the total derivatives.

Considering the system

$$\begin{cases} A = A(\alpha, \beta), \\ B = B(\alpha, \beta), \end{cases} \tag{4.2.1}$$

and computing the total time derivatives gives [2]

$$\begin{cases} \dfrac{DA}{Dt} = \dfrac{\partial A}{\partial \alpha}\dfrac{D\alpha}{Dt} + \dfrac{\partial A}{\partial \beta}\dfrac{D\beta}{Dt}, \\ \dfrac{DB}{Dt} = \dfrac{\partial B}{\partial \alpha}\dfrac{D\alpha}{Dt} + \dfrac{\partial B}{\partial \beta}\dfrac{D\beta}{Dt}, \end{cases} \tag{4.2.2}$$

where the quantities $\partial A/\partial \alpha$, $\partial A/\partial \beta$, $\partial B/\partial \alpha$ and $\partial B/\partial \beta$ depend on the model considered. The goal is now to inverse this system in order to express $D\alpha/Dt$ and $D\beta/Dt$ as functions of DA/Dt and DB/Dt. One may think that it should be easier to start from the expressions $\alpha = \alpha(A, B)$ and $\beta = \beta(A, B)$ so that, the system does not need to be inverted. However, this would have needed the expressions of $\partial \alpha/\partial A$, $\partial \alpha/\partial B$, $\partial \beta/\partial A$ and $\partial \beta/\partial B$ which are different depending on the type of solution chosen (natural or ghost solution). This kind of ambiguity does not appear in the above system since the expressions of Eq. 4.2.1 are uniquely defined for any pair (α, β). This choice is then made in order to stay general again[3].

The inverted system takes the form

$$\begin{cases} \dfrac{D\alpha}{Dt} = \dfrac{1}{J}\left(\dfrac{\partial B}{\partial \beta}\dfrac{DA}{Dt} - \dfrac{\partial A}{\partial \beta}\dfrac{DB}{Dt}\right), \\ \dfrac{D\beta}{Dt} = \dfrac{1}{J}\left(-\dfrac{\partial B}{\partial \alpha}\dfrac{DA}{Dt} + \dfrac{\partial A}{\partial \alpha}\dfrac{DB}{Dt}\right), \end{cases} \tag{4.2.3}$$

---

[2]Given a general function $f = f(\alpha, \beta)$, the following holds:

$$\frac{Df}{Dt} = \frac{\partial f}{\partial t} + u_k^\infty \frac{\partial f}{\partial x_k} = \frac{\partial f}{\partial \alpha}\frac{\partial \alpha}{\partial t} + \frac{\partial f}{\partial \beta}\frac{\partial \beta}{\partial t} + u_k^\infty \left(\frac{\partial f}{\partial \alpha}\frac{\partial \alpha}{\partial x_k} + \frac{\partial f}{\partial \beta}\frac{\partial \beta}{\partial x_k}\right)$$

$$= \frac{\partial f}{\partial \alpha}\left(\frac{\partial \alpha}{\partial t} + u_k^\infty \frac{\partial \alpha}{\partial x_k}\right) + \frac{\partial f}{\partial \beta}\left(\frac{\partial \beta}{\partial t} + u_k^\infty \frac{\partial \beta}{\partial x_k}\right) = \frac{\partial f}{\partial \alpha}\frac{D\alpha}{Dt} + \frac{\partial f}{\partial \beta}\frac{D\beta}{Dt}.$$

[3]Note that for the FENE-L model, one could have quite generally considered the natural solution, but it is not the case for the FENE-LS$_0$ model as explained in Sec. 3.1.

where J is the determinant of the Jacobian matrix related to the change of variables $(A, B) \rightarrow (\alpha, \beta)$. It is expressed as

$$J = \frac{\partial A}{\partial \alpha}\frac{\partial B}{\partial \beta} - \frac{\partial A}{\partial \beta}\frac{\partial B}{\partial \alpha} \tag{4.2.4}$$

and will simply be called *Jacobian* in the following. Equation 3.2.3 can be injected in the above system in order to give

$$\frac{\mathrm{D}\alpha}{\mathrm{D}t} = 2\dot{\gamma}_{ij}A_{ij}\underbrace{\left(\frac{1}{J}\left[\frac{\partial B}{\partial \beta} - \frac{2B}{A}\frac{\partial A}{\partial \beta}\right]\right)}_{\alpha^{\mathrm{d}}}$$

$$+ \frac{1}{\mathrm{Wi}}\underbrace{\left(\frac{1}{J}\left[\frac{\partial B}{\partial \beta}(3 - A^{\mathrm{sp}}) - \frac{\partial A}{\partial \beta}(10A - 2B^{\mathrm{sp}})\right]\right)}_{\alpha^{\mathrm{rel}}}$$

$$+ \frac{1}{\mathrm{Pe}}\underbrace{\left(\frac{1}{J}\left[\frac{\partial B}{\partial \beta}\frac{\partial^2 A}{\partial x_k \partial x_k} - \frac{\partial A}{\partial \beta}\frac{\partial^2 B}{\partial x_k \partial x_k}\right]\right)}_{\alpha^{\mathrm{diff}}} \tag{4.2.5}$$

where each term corresponds to a different physical meaning: α^{d} the drag force exerted by the flow, α^{rel} the spring force of the dumbbells (and the configurational diffusion) and α^{diff} the center-of-mass diffusion. The same equation can be obtained for β (with the same notations) but is not written here for readability. However, it has the same shape and one only has to replace $\partial B/\partial \beta$ by $-\partial B/\partial \alpha$ and $-\partial A/\partial \beta$ by $\partial A/\partial \alpha$ in order to write it. In the above equation, note that in order to be consistent, the different terms should be expressed as functions of α and β. However, as already mentioned, this generally depends on the model considered and leads to quite heavy expressions. This is thus kept in the above general form and the further mathematical developments are not detailed here. Only the conclusions about the permeability of the boundaries will be exposed.

Note that the Laplacian of A and B still needs to be expressed in terms of α and β by applying the chain rule twice. Considering a general function $f = f(\alpha, \beta)$, where f can either be A or B, it yields

$$\frac{\partial^2 f}{\partial x_k \partial x_k} = \frac{\partial f}{\partial \alpha}\frac{\partial^2 \alpha}{\partial x_k \partial x_k} + \frac{\partial f}{\partial \beta}\frac{\partial^2 \beta}{\partial x_k \partial x_k} + \frac{\partial^2 f}{\partial \alpha^2}\frac{\partial \alpha}{\partial x_k}\frac{\partial \alpha}{\partial x_k} + 2\frac{\partial^2 f}{\partial \alpha \partial \beta}\frac{\partial \alpha}{\partial x_k}\frac{\partial \beta}{\partial x_k} + \frac{\partial^2 f}{\partial \beta^2}\frac{\partial \beta}{\partial x_k}\frac{\partial \beta}{\partial x_k}. \tag{4.2.6}$$

As can be seen, the Laplacian of A or B does not simply transforms into the Laplacian of α and β but non linear terms appear such as the square of the gradient of α or β and the product of the gradients of α and β. This could be expected since, as was said earlier, *classical diffusion* on α and β cannot make the solution leave its admissible domain (since it is rectangular). From the observation that the solution can actually leave its domain, it seems logical that the diffusive terms in the evolution equations of α and β are not simply Laplacians.

In order to differentiate the impact of each terms, these are treated separately in Sec. 4.2.1–4.2.3.

4.2.1 Drag force

In the evolution equation of α, the drag term is always positive and bounded, but it cancels in the evolution equation of β. These results are similar for both the FENE-L and FENE-LS$_0$ closure approximation. It well underlines the role played by the drag force on the dumbbells. In fact, it has the effect of stretching the dumbbells and this manifests in the radial probability distribution through the shifting of the distribution at higher extensions. However, the shape of the canonical distribution is left unaltered by the drag force.

4.2.2 Relaxation

The expression of this term is quite complex and difficult to analyze in general. It is however possible to express it on the different boundaries as before in order to understand the role played by the relaxation on the permeability properties of the boundaries. On b$_3$, β^{rel} is negative and bounded (for both models). On b$_1$, β^{rel} is positive for both models. However it is bounded for the FENE-LS$_0$ but infinite for the FENE-L. For the FENE-L, $\alpha^{\mathrm{rel}} \to -\infty$ on b$_2$, but for the FENE-LS$_0$, $\alpha^{\mathrm{rel}} \to -\infty$ above b$_\star$ and $\alpha^{\mathrm{rel}} \to +\infty$ below b$_\star$. Since α^{d} is finite on b$_2$, its influence is negligible compared to the effect of α^{rel}.

Finally, on b$_\star$ (for the FENE-LS$_0$), β^{rel} tends toward $+\infty$ from above and toward $-\infty$ from below. This means that without considering center-of-mass diffusion, the boundary b$_\star$ is impermeable such that if a solution is initially above (resp. below) b$_\star$, it will remain above (resp. below) it. It shows that (without diffusion at least) it is totally reasonable to consider only the natural solution $(\overline{\alpha}, \overline{\beta})$ and to discard the ghost one. In fact, the boundaries of the subspace above b$_\star$ are totally impermeable. However, this is not the case for the subspace below b$_\star$ since b$_2$ is permeable over there.

It is interesting to realize that the boundary b$_\star$ plays the same role for the FENE-LS$_0$ as the boundary b$_1$ for the FENE-L. In fact, they both correspond to the same curve in the (A, B)-space and to the zone where $\overline{\beta} = \tilde{\beta}$ because the argument of the square root is 0. Also, a singularity appears in β^{rel} such that the solution tends to be repelled by this boundary. Finally, the boundary b$_2$ is impermeable above that same curve.

4.2.3 Center-of-mass diffusion

From Eq. 4.2.6, note that the $\partial^2 f / \partial \beta^2$ term (where $f = A$ or B) is 0 for both models. This comes form the specific expressions of A and B that linearly depend on β (see Eq. 2.2.2 and 2.2.6). Using this result, the diffusive terms write

$$\alpha^{\mathrm{diff}} = \frac{\partial^2 \alpha}{\partial x_k \partial x_k} + \frac{1}{J}\left(\frac{\partial B}{\partial \beta}\frac{\partial^2 A}{\partial \alpha^2} - \frac{\partial A}{\partial \beta}\frac{\partial^2 B}{\partial \alpha^2}\right)\frac{\partial \alpha}{\partial x_k}\frac{\partial \alpha}{\partial x_k} + \frac{2}{J}\left(\frac{\partial B}{\partial \beta}\frac{\partial^2 A}{\partial \alpha \partial \beta} - \frac{\partial A}{\partial \beta}\frac{\partial^2 B}{\partial \alpha \partial \beta}\right)\frac{\partial \alpha}{\partial x_k}\frac{\partial \beta}{\partial x_k},$$

$$\beta^{\mathrm{diff}} = \frac{\partial^2 \beta}{\partial x_k \partial x_k} + \frac{1}{J}\left(\frac{\partial A}{\partial \alpha}\frac{\partial^2 B}{\partial \alpha^2} - \frac{\partial B}{\partial \alpha}\frac{\partial^2 A}{\partial \alpha^2}\right)\frac{\partial \alpha}{\partial x_k}\frac{\partial \alpha}{\partial x_k} + \frac{2}{J}\left(\frac{\partial A}{\partial \alpha}\frac{\partial^2 B}{\partial \alpha \partial \beta} - \frac{\partial B}{\partial \alpha}\frac{\partial^2 A}{\partial \alpha \partial \beta}\right)\frac{\partial \alpha}{\partial x_k}\frac{\partial \beta}{\partial x_k}.$$

$$(4.2.7)$$

Notice that the first term of each equation simply becomes the Laplacian of α or β.

The goal of the following is then to compute the values of these two terms at the boundaries and see whether they can make the solution leave its admissible space or

not. However, as was already found for the same study in the (A, B)-space, the sign of α^{diff} and β^{diff} can generally depend on the values of the gradients of α and β at the boundaries. In the most general situation, the only thing that can be said is that $(\partial\alpha/\partial x_k)(\partial\alpha/\partial x_k)$ is positive since it is the square of the norm of the gradient of α. There is however a specific situation in which some other terms are restricted to some values.

Consider a general solution. If it enters in contact with a specific boundary at some point, the point (α, β) at which the solution touches the boundary is necessary an extremum (since the domain is rectangular). If that specific point is on a boundary of the spatial domain (in the $\boldsymbol{x}$-space), nothing much can be said. However, if that point is inside the spatial domain, it means that the gradient of either α or β vanishes and that the sign of the Laplacian of α or β is known. In fact, considering that the solution touches the boundary b_2, that point is at the maximum along α, such that its Laplacian is negative and its gradient vanishes. On b_1 (resp. b_3), the gradient of β vanishes and the point reaches a minimum (resp. maximum) along β, such that the Laplacian of β is positive (resp. negative). Finally, on $b_\star$ (for the FENE-LS$_0$), the gradient of β vanishes and if the solution comes from above (resp. below) $b_\star$, the Laplacian of β is positive (resp. negative). Assuming now that the above hypothesis is true (the solution enters in contact with the boundaries somewhere inside of its $\boldsymbol{x}$-space), the terms α^{diff} and β^{diff} are much simpler and a conclusion can generally be drawn.

On b_2, $\alpha^{\text{diff}} < 0$ such that the diffusion cannot make b_2 permeable. Note also that because of the singularity in the relaxation term, the diffusion cannot make b_2 permeable even if the above condition is not fulfilled (the other terms in α^{diff} being finite anyway). On b_3, $\beta^{\text{diff}} < 0$ such that the boundary stays impermeable even with diffusion. For the FENE-LS$_0$ model, $\beta^{\text{diff}} > 0$ on b_1 such that the permeability is also left unaltered by the diffusion (even if that boundary is not really interesting anymore as only the natural solution can be considered).

This is however different on the boundary b_1 for the FENE-L and the boundary $b_\star$ for the FENE-LS$_0$[4]. Since the results at these boundaries are similar, only the case of the $b_\star$ boundary is treated here. Depending on whether $b_\star$ is approached from above or from below, $\beta^{\text{diff}} \to -\infty$ or $+\infty$ respectively. This means that diffusion will have the effect of making the solution be attracted by the boundary. However, the relaxation term has the opposite effect such that the relaxation and the diffusion compete against each other to determine whether β^{diff} tends toward $+$ or $-\infty$ above $b_\star$ (but this is the opposite below $b_\star$). More concretely, there is a threshold for the gradient of α that generally depends on Pe,α and b such that if the gradient is below the threshold, the relaxation term dominates and the boundary repels the solution. However, if the center-of-mass diffusion dominates, the solution is attracted by the boundary (above the boundary, $\beta^{\text{diff}} \to -\infty$ and below the boundary, $\beta^{\text{diff}} \to +\infty$).

The issue is that on that boundary, the Jacobian J is 0, such that the system is not invertible. This means that both $D\alpha/Dt$ and $D\beta/Dt$ grow unbounded when the solution tends toward that boundary. When diffusion dominates, the solution is then attracted toward that zone, but on that precise boundary, a singularity exists and the solution diverges. This is in fact what is observed by visualizing the evolution of the

---

[4]Note once again the equivalence of these boundaries for both models.

channel flow solution in the (α, β)-space as the central point of the channel gets closer and closer to the boundary $b_\star$ (or b_1 for the FENE-L) and diverges when it enters in contact with it.

One should note that the way the diffusion has been added to the originally well-behaved system of equations was through the Fokker-Planck equation. In fact, the origin of this term is totally appropriate from a physical point of view. The fact that the diffusion seems to be artificial and lead to unexpected results probably comes from the canonical subspace approximation. In fact, as explained in Sec. 2.1, the canonical subspace is not necessarily invariant under the Fokker-Planck equation, such that a canonical probability density distribution may leave its canonical subspace depending on its specific parameterization. As shown in the original article of Lielens *et al.* on the FENE-L [6], the admissible space of the general FENE model is convex in the (A, B)-space, such that center-of-mass diffusion would probably not add any issue.

4.3   Modified diffusion

The problem underlined in the previous section makes the center-of-mass diffusion not usable in practice. This is quite an important problem since it makes the FENE-L and FENE-LS$_0$ models nearly impossible to use for EIT or MDR Eulerian simulations considering the still quite low Peclet number used nowadays. To alleviate this problem, either numerical tools should be developed in order to be able to increase the Peclet number (or said differently, to be able to accommodate a very small diffusion term) or a modified diffusion term should be considered in order for the solution not to leave it admissible space anymore. A possible way for the second solution is proposed here.

As was already mentioned several times, the fact that the solution is potentially able to leave its admissible domain comes from the fact that the diffusion is applied on A and B and that the admissible (A, B)-space is not rectangular. More precisely, this can happen because the (A, B)-domain is concave (on its upper boundary). An alternative is to apply the diffusion on α and β. In fact, the (α, β) admissible domain is rectangular such that this kind of diffusion could not make the solution cross its boundaries. However, since the problem is typically solved in the (A, B)-space, the modified diffusion in the (α, β)-space should be transformed back into the (A, B)-space.

The idea is thus to consider the α and β diffusive terms as simple Laplacians:

$$\begin{cases} \alpha^{\mathrm{diff}} = \dfrac{\partial^2 \alpha}{\partial x_k \partial x_k}, \\ \beta^{\mathrm{diff}} = \dfrac{\partial^2 \beta}{\partial x_k \partial x_k}. \end{cases} \tag{4.3.1}$$

The procedure that was used for deriving the evolution equations of α and β can be followed the other way around such that injecting back Eq. 4.2.5 (and the equivalent evolution equation for β) into Eq. 4.2.2 yields

$$\begin{cases} \dfrac{\mathrm{D}A}{\mathrm{D}t} - 2\dot{\gamma}_{ij} A_{ij} = \dfrac{1}{\mathrm{Wi}} \left(3 - A^{\mathrm{sp}} \right) + \dfrac{1}{\mathrm{Pe}} A^{\mathrm{diff}}, \\ \dfrac{\mathrm{D}B}{\mathrm{D}t} - \dfrac{4B}{A} \dot{\gamma}_{ij} A_{ij} = \dfrac{1}{\mathrm{Wi}} \left(10A - 2B^{\mathrm{sp}} \right) + \dfrac{1}{\mathrm{Pe}} B^{\mathrm{diff}}, \end{cases} \tag{4.3.2}$$

which is the same equation as Eq. 3.2.3 where the Laplacians have been replaced by more general diffusive terms that take the form

$$
\begin{cases}
A^{\text{diff}} = \dfrac{\partial A}{\partial \alpha} \dfrac{\partial^2 \alpha}{\partial x_k \partial x_k} + \dfrac{\partial A}{\partial \beta} \dfrac{\partial^2 \beta}{\partial x_k \partial x_k}, \\[2ex]
B^{\text{diff}} = \dfrac{\partial B}{\partial \alpha} \dfrac{\partial^2 \alpha}{\partial x_k \partial x_k} + \dfrac{\partial B}{\partial \beta} \dfrac{\partial^2 \beta}{\partial x_k \partial x_k}.
\end{cases}
\tag{4.3.3}
$$

As was done before, the Laplacians then need to be expressed in terms of A and B. Considering a general function $g = g(A, B)$ that could be α or β and applying the chain rule twice gives

$$
\frac{\partial^2 g}{\partial x_k \partial x_k} = \frac{\partial g}{\partial A} \frac{\partial^2 A}{\partial x_k \partial x_k} + \frac{\partial g}{\partial B} \frac{\partial^2 B}{\partial x_k \partial x_k} + \frac{\partial^2 g}{\partial A^2} \frac{\partial A}{\partial x_k} \frac{\partial A}{\partial x_k} + \frac{\partial^2 g}{\partial B^2} \frac{\partial B}{\partial x_k} \frac{\partial B}{\partial x_k} + 2 \frac{\partial^2 g}{\partial A \partial B} \frac{\partial A}{\partial x_k} \frac{\partial B}{\partial x_k}.
\tag{4.3.4}
$$

Particularizing the above expression to α or β and injecting this in Eq. 4.3.3 gives the general expressions of the modified diffusive terms for A and B. This is however not written explicitly here as the expressions are quite long and would not add any comprehension.

In order to explicitly write the full expressions of the diffusive terms, one should then compute the different partial derivatives (that are specific to each constitutive model considered): $\partial g/\partial A$, $\partial g/\partial B$, $\partial^2 g/\partial A^2$, $\partial^2 g/\partial B^2$, $\partial^2 g/\partial A \partial B$, where g again represents α or β and also $\partial f/\partial \alpha$, $\partial f/\partial \beta$ where f again represents A or B and express all these derivatives as functions of A and B. Note however that, by lack of time, the above expressions have not been computed such that the modified diffusion method has thus not been tested yet in practice.

Finally, note that there are still different ways to solve the polymers equations. In fact, the modified diffusion, as presented here, only comes into account in the equations for A and B (Eq. 4.3.2). However, this does not a priori suggest the form of the diffusive terms in the equations for A_{ij}. In order to take the modified diffusion into account, one could for example solve for the mean square extension A and all the conformation tensor components except from A_{11}, A_{22} or A_{33}, which can be computed from the two other diagonal elements and the trace. Another solution would be to solve for all the components and the mean square extension and to rescale the tensor in order to obtain the proper value of the trace. This is thus still an open question.

Chapter 5

Passive polymer response to a turbulent channel flow

The ultimate goal is to analyze the influence of the polymers on turbulence. However, only the one-way influence of the turbulence on the polymers is studied in this work. In order to do so, several particles are tracked from an Eulerian Newtonian turbulent flow simulation and at the same time, the velocity gradients that they experience over time are recorded. These velocity gradients are then introduced in the Lagrangian equations for the polymers and the polymer responses are computed without having to take into account the center-of-mass diffusion term.

In doing so, it is clear that the effects of the polymers dynamics on the turbulent coherent structures are not taken into account. Nonetheless, this procedure allows to compare rigorously the different polymer models between each other. In fact, in this case the polymers always experience the same flow conditions, whatever the model used (which wouldn't have been the case in a coupled simulation since the flow would have been altered differently by each model). Moreover, the procedure is less numerically challenging in the sense that the coupled equations sometimes need a very small time step to remain stable, which is less critical for a Newtonian simulation. One should also mention the fact that the polymers equations are thus made considerably simpler in the sense that these are transformed into ordinary differential equations in time where the velocity gradients are imposed from the Newtonian simulation. Also the non-linear advective terms vanish which makes useless the addition of spurious diffusion, so that it can safely be not considered and the problem of diffusion explained in the previous chapter is therefore bypassed.

In the end, this can be seen as a satisfactory intermediary step in considering the effect of new complex models on the physics of interest.

5.1 Turbulent Newtonian channel flow

The flow configuration considered in this case is a plane channel flow. The streamwise and spanwise directions are considered infinite by the mean of periodic boundary conditions, but still the computational domain has to be finite such that the e_x and e_y extents of the domain are respectively $\hat{L}_x$ and $\hat{L}_y$. Additionally, no-slip boundary

conditions are applied at the walls. The half channel width is $\hat{h}$ and the center of the channel corresponds to $\hat{z} = 0$, such that the walls are located at $\hat{z} = \pm\hat{h}$. A schematic of the channel is shown in Fig. 5.1.1. Finally, it is important to stress that the wall normal direction is $\boldsymbol{e_z}$ while the spanwise direction is $\boldsymbol{e_y}$.
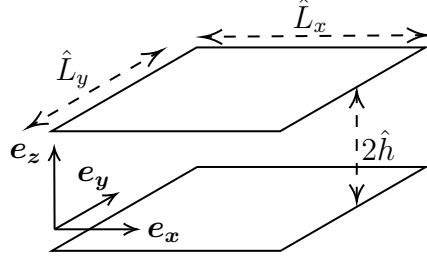

Figure 5.1.1: Channel representation.

The equations that are solved are the incompressible Navier-Stokes equations:

$$\begin{cases} \dfrac{\partial \hat{u}_i}{\partial \hat{x}_i} = 0, \\ \dfrac{\partial \hat{u}_i}{\partial \hat{t}} + \hat{u}_j \dfrac{\partial \hat{u}_i}{\partial \hat{x}_j} = -\dfrac{1}{\rho}\dfrac{\partial \hat{p}}{\partial x_i} + \nu \dfrac{\partial^2 \hat{u}_i}{\partial \hat{x}_j \partial \hat{x}_j} + \hat{f}_i, \end{cases} \tag{5.1.1}$$

where $\hat{\boldsymbol{u}}$ is the velocity, $\hat{p}$ the pressure, $\hat{\boldsymbol{f}}$ an eventual forcing term, ρ the fluid density and ν the fluid kinematic density. Another important quantity is the bulk velocity $\hat{U}_{\mathrm{b}}$ defined as

$$\hat{U}_{\mathrm{b}} = \frac{1}{2\hat{h}\hat{L}_x\hat{L}_y} \int_{-\hat{h}}^{\hat{h}} \int_0^{\hat{L}_y} \int_0^{\hat{L}_x} \hat{u}\,\mathrm{d}\hat{x}\mathrm{d}\hat{y}\mathrm{d}\hat{z}. \tag{5.1.2}$$

These equations can be non-dimensionalized be choosing a characteristic length scale $\mathcal{L}$ and velocity $\mathcal{U}$. The independent variables thus transform has:

$$\begin{cases} x_i = \dfrac{\hat{x}_i}{\mathcal{L}}, \\ t = \dfrac{\mathcal{U}}{\mathcal{L}}\hat{t}, \end{cases} \Rightarrow \begin{cases} \dfrac{\partial}{\partial \hat{x}_i} = \dfrac{1}{\mathcal{L}}\dfrac{\partial}{\partial x_i}, \\ \dfrac{\partial}{\partial \hat{t}} = \dfrac{\mathcal{U}}{\mathcal{L}}\dfrac{\partial}{\partial t}. \end{cases} \tag{5.1.3}$$

The flow variables can then be non-dimensionalized as such:

$$\begin{cases} u_i = \dfrac{\hat{u}_i}{\mathcal{U}}, \\ f_i = \dfrac{\mathcal{L}}{\mathcal{U}^2}\hat{f}_i, \\ p = \dfrac{1}{\rho\mathcal{U}^2}\hat{p}, \end{cases} \Leftrightarrow \begin{cases} \hat{u}_i = \mathcal{U}u_i, \\ \hat{f}_i = \dfrac{\mathcal{U}^2}{\mathcal{L}}f_i, \\ \hat{p} = \rho\mathcal{U}^2 p. \end{cases} \tag{5.1.4}$$

Using these expressions, the incompressible Navier-Stokes equations write

$$
\begin{cases}
\dfrac{\mathcal{U}}{\mathcal{L}}\dfrac{\partial u_i}{\partial x_i} = 0, \\[2mm]
\dfrac{\mathcal{U}^2}{\mathcal{L}}\dfrac{\partial u_i}{\partial t} + \dfrac{\mathcal{U}^2}{\mathcal{L}}u_j\dfrac{\partial u_i}{\partial x_j} = -\dfrac{\mathcal{U}^2}{\mathcal{L}}\dfrac{\partial p}{\partial x_i} + \dfrac{\nu\mathcal{U}}{\mathcal{L}^2}\dfrac{\partial^2 u_i}{\partial x_j \partial x_j} + \dfrac{\mathcal{U}^2}{\mathcal{L}}f_i,
\end{cases}
$$

$$
\Leftrightarrow
\begin{cases}
\dfrac{\partial u_i}{\partial x_i} = 0, \\[2mm]
\dfrac{\partial u_i}{\partial t} + u_j\dfrac{\partial u_i}{\partial x_j} = -\dfrac{\partial p}{\partial x_i} + \dfrac{1}{\mathrm{Re}}\dfrac{\partial^2 u_i}{\partial x_j \partial x_j} + f_i,
\end{cases}
\tag{5.1.5}
$$

where the well known Reynolds number is defined as

$$
\mathrm{Re} \equiv \frac{\mathcal{U}\mathcal{L}}{\nu}
\tag{5.1.6}
$$

and represents the ratio between inertia and viscous forces. The bulk velocity can also be non-dimensionalized as

$$
U_{\mathrm{b}} = \frac{\hat{U}_{\mathrm{b}}}{\mathcal{U}} = \frac{1}{2\hat{h}\hat{L}_x\hat{L}_y}\int_{-\hat{h}}^{\hat{h}}\int_0^{\hat{L}_y}\int_0^{\hat{L}_x} u\,\mathrm{d}\hat{x}\mathrm{d}\hat{y}\mathrm{d}\hat{z} = \frac{1}{2hL_xL_y}\int_{-h}^{h}\int_0^{L_y}\int_0^{L_x} u\,\mathrm{d}x\mathrm{d}y\mathrm{d}z, \quad (5.1.7)
$$

where the quantities $\hat{h}$, $\hat{L}_x$ and $\hat{L}_y$ have been non-dimensionalized by the characteristic length of the channel to give h, L_x and L_y respectively.

In order to drive and control a plane channel flow, there are two main choices: either the pressure gradient is fixed and the bulk velocity can be calculated from the flow solution, or the bulk velocity is fixed and the pressure gradient is tuned in order to obtain the prescribed bulk velocity. In this case, the second method is used, so that the bulk velocity is prescribed. A natural choice for the characteristic velocity is thus the bulk velocity and one also chooses the channel half width as the problem length scale. This then yields

$$
\begin{cases}
\mathrm{Re} = \mathrm{Re}_{\mathrm{b}} = \dfrac{\hat{U}_{\mathrm{b}}\hat{h}}{\nu}, \\[2mm]
h = 1, \\[2mm]
U_{\mathrm{b}} = \dfrac{1}{2L_xL_y}\int_{-1}^{1}\int_0^{L_y}\int_0^{L_x} u\,\mathrm{d}x\mathrm{d}y\mathrm{d}z = 1.
\end{cases}
\tag{5.1.8}
$$

where Re_{b} is the bulk Reynold number, which has to be fixed.

In order to drive the flow in the $\boldsymbol{e_x}$ direction, one needs to impose a pressure gradient in that direction. However, since the boundary conditions are periodic along $\boldsymbol{e_x}$, the pressure should also be periodic along $\boldsymbol{e_x}$. Moreover, if the streamwise pressure gradient is fixed, it does not let any streamwise pressure fluctuation develop. The technique is then rather to apply a streamwise body force. The body force f_i thus have the shape $f_i = f\delta_{i1}$ and its magnitude (f) is tuned in order to obtain a non-dimensional bulk velocity of 1. This is done in practice by adding an equation for the bulk velocity.

To summarize, the non-dimensional flow equations to solve are

$$\begin{cases} \dfrac{\partial u_i}{\partial x_i} = 0, \\[2mm] \dfrac{\partial u_i}{\partial t} + u_j \dfrac{\partial u_i}{\partial x_j} = -\dfrac{\partial p}{\partial x_i} + \dfrac{1}{\mathrm{Re}}\dfrac{\partial^2 u_i}{\partial x_j \partial x_j} + f\delta_{i1}, \\[2mm] \dfrac{1}{2L_x L_y} \displaystyle\int_{-1}^{1}\int_{0}^{L_y}\int_{0}^{L_x} u\,\mathrm{d}x\mathrm{d}y\mathrm{d}z = 1, \end{cases} \tag{5.1.9}$$

and the bulk Reynolds number is chosen to be $\mathrm{Re_b} = 5000$.

5.1.1 Turbulent statistics analysis

In order to verify the solution of the problem, one has to compute meaningful flow variables and check their correctness. In this case, since the goal is to develop a turbulent flow it is important to consider statistics. These will be the mean flow, the root-mean-squared (RMS) velocity fluctuations and the Reynold shear stress. These variables will be non-dimensionalized and expressed in wall units.

The friction velocity $\hat{u}_\star$ is defined as

$$\hat{u}_\star \equiv \sqrt{\frac{\hat{\tau}_\mathrm{w}}{\rho}}, \tag{5.1.10}$$

where $\hat{\tau}_\mathrm{w}$ is the wall shear stress. The wall shear stress can be related to the driving force of the flow (the forcing term here) and it is possible to show that it is related to the volume averaged body force, noted $\hat{F}$ (by doing a force balance) as

$$\hat{\tau}_\mathrm{w} = \rho \hat{h}\hat{F} = \rho \hat{U}_\mathrm{b}^2 F \tag{5.1.11}$$

and

$$\tau_\mathrm{w} = \frac{\hat{\tau}_\mathrm{w}}{\rho \hat{U}_\mathrm{b}^2} = F \tag{5.1.12}$$

naturally appears as the non-dimensionalized wall shear stress. Injecting this result in the expression of the friction velocity yields

$$\hat{u}_\star = \hat{U}_\mathrm{b}\sqrt{F} \tag{5.1.13}$$

and again

$$u_\star = \frac{\hat{u}_\star}{\hat{U}_\mathrm{b}} = \sqrt{F} \tag{5.1.14}$$

naturally appears as the non-dimensionalized friction velocity.

The wall Reynolds number can be defined as

$$\mathrm{Re}_\tau \equiv \frac{\hat{h}\hat{u}_\star}{\nu} \tag{5.1.15}$$

and using the expression of the Reynolds number:

$$\mathrm{Re}_\tau = \frac{\mathrm{Re_b}\hat{u}_\star}{\hat{U}_\mathrm{b}} = \mathrm{Re_b} u_\star. \tag{5.1.16}$$

More generally, rather than being expressed at the integral scale (scale of the channel), the flow quantities may also be expressed in wall units. A quantity expressed in wall units will generally be denoted $\cdot^+$. Here are some examples with the velocity and the wall normal coordinate:

$$
\begin{cases}
u^+ = \dfrac{\hat{u}}{\hat{u}_\star} = \dfrac{u}{u_\star}, \\[2mm]
z^+ = \dfrac{\hat{z}\hat{u}_\star}{\nu} = \mathrm{Re_b}\dfrac{\hat{z}\hat{u}_\star}{h\hat{U}_\mathrm{b}} = \mathrm{Re_b}zu_\star = z\mathrm{Re}_\tau.
\end{cases}
\tag{5.1.17}
$$

Note however that since the volume averaged non-dimensional forcing term F generally varies in time, the friction velocity and the wall Reynolds number are also functions of time. In order to express the turbulent quantities in wall units, the time average of both quantities are then used.

The average for the turbulent statistics is noted $\bar{\cdot}$ and is defined as

$$
\bar{\cdot} = \frac{1}{L_x L_y T} \int_{t_0}^{t_0+T} \int_0^{Ly} \int_0^{Lx} \cdot \ \mathrm{d}x\,\mathrm{d}y\,\mathrm{d}t,
\tag{5.1.18}
$$

where t_0 is the initial averaging time and T is the duration of the averaging window. In fact, the turbulence analyzed here is stationary and invariant under a $\boldsymbol{e_x}$ or $\boldsymbol{e_y}$ translation, which makes this average procedure well suited for the problem. An averaged turbulent quantity can then only vary along the wall normal direction. The fluctuations of a quantity are noted $\cdot'$ and defined as

$$
\cdot' = \cdot - \bar{\cdot}.
\tag{5.1.19}
$$

Finally, another important statistical operation is the root-mean-squared fluctuations of a quantity, noted $\cdot'_\mathrm{rms}$ and defined as

$$
\cdot'_\mathrm{rms} = \sqrt{\overline{(\cdot')^2}}.
\tag{5.1.20}
$$

The turbulent statistics of interest that were computed here are the mean streamwise velocity $\bar{u}$, the RMS of the velocity fluctuations u'_rms, v'_rms and w'_rms and the Reynolds shear stress $\overline{u'w'}$. Note that all these quantities are expresses in wall units such that

$$
\begin{cases}
\bar{u}^+ = \dfrac{\bar{u}}{u_\star}, \\[3mm]
\left(u'_\mathrm{rms}\right)^+ = \dfrac{u'_\mathrm{rms}}{u_\star}, \\[3mm]
\overline{u'w'}^+ = \dfrac{\overline{u'w'}}{u_\star^2}.
\end{cases}
\tag{5.1.21}
$$

Note also that in this problem, the spanwise and wall normal mean velocities, as well as the other components of the Reynold stress tensor should vanish if one considers an infinite averaging window. The duration of the averaging T being finite in practice, this is however not the case. Some of these quantities will thus be presented as well in order to assess the convergence of the turbulent statistics. The same holds for the fact that the problem is symmetrical along the channel center: the statistics of the upper and lower parts will be compared rather than being used to complete the statistics.

5.1.2 DEDALUS: a flexible spectral solver

In order to solve efficiently the Navier-Stokes equations, the DEDALUS framework is used. This is a spectral solver that aims at solving very arbitrary sets of partial differential equations (though it was originally developed for fluid flows) such that the equations are entered symbolically. It uses spectral space discretization and among other things, it can solve initial value problems. In this case, the problem reduces to a system of ordinary (coupled and non-linear) differential equations, which is solved by implicit-explicit time integration. This is written in PYTHON and parallelized using MPI. Note that the version 2 of DEDALUS was used in this project for compatibility reasons with other codes, although version 3 exists.

The power of spectral methods is their efficiency when at least two dimensions are periodic (which is the case here) and the fact that the spatial discretization does not induce any dissipation error. It also needs less grid points (or degree of freedom) in order to be accurate as long as the solution is smooth.

Different types of spectral discretization are accessible. In this case, the basis were discretized using Fourier decomposition in the periodic directions and Chebyshev polynomials decomposition in the wall normal direction. Note that thanks to the spectral decomposition of the solution, exact derivative and interpolation is possible even between two grid points. For time integration, a Runge-Kutta IMEX method has been used for implicit-explicit time stepping. More precisely, the 3rd-order 4-stages method has been considered.

5.1.3 Numerical considerations

The non-dimensional extents of the domain in the periodic directions are $L_x = \pi$ and $L_y = 1$. Also, the number of elements in each directions are $(N_x, N_y, N_z) = (128, 96, 192)$ and the non-dimensional time step is $\Delta t = 2.5 \cdot 10^{-3}$. Note that considering a non-dimensional bulk velocity of 1 and a non-dimensional channel length of π, the non-dimensional flow-through time is π.

The initial condition is the one of a laminar Poiseuille flow. However, in order to trigger turbulence faster, blowing-suction boundary conditions were initially applied at the walls for a duration of 10 non-dimensional time. It consists in imposing a non-zero wall normal velocity at the wall to add perturbations to the flow. As explained by Dubief *et al.* [3], the goal is to numerically mimic an experimental turbulence transition method. In this case, the expression of the blowing-suction boundary condition was

$$w|_{z=\pm 1} = A \sin\left(8\pi \frac{x}{L_x}\right) \sin\left(8\pi \frac{y}{L_y}\right), \tag{5.1.22}$$

with $A = 0.15$. Also note that this boundary condition was progressively activated during 3 non-dimensional time using a linear ramp before being maintained at its prescribed intensity for 7 non-dimensional time and then being stopped at once to recover the classical no-slip boundary condition.

The initial time of the turbulent simulation corresponds to the instant where the no-slip boundary condition is recovered. The simulation has been computed for 750 non-dimensional time (which corresponds to approximately 240 flow-through time) before

starting to collect any statistics, after which all the statistics were recorded with a sampling period of 10^{-2} non-dimensional time from $t = 750$ until $t = 1650$.

5.1.4   Statistics convergence

The first quantities to compute are the wall Reynold number Re_τ and the friction velocity $u_\star$. In fact, these are needed to express all the other variables in wall units, but can also be used to study the convergence of the turbulent statistics. Figure 5.1.2 shows the time evolution of the instantaneous wall Reynolds number[1] as well as its cumulative time average defined as

$$\frac{1}{t} \int_{t_0}^{t_0+t} \mathrm{Re}_\tau \left(\tilde{t} \right) \mathrm{d}\tilde{t}. \tag{5.1.23}$$

As can be seen, the wall Reynolds number fluctuates quite intensely between 274 and 310 and at the end of the averaging window, its value is $\mathrm{Re}_\tau \approx 292$, corresponding to a friction velocity of $u_\star \approx 0.058$. Figure 5.1.2 shows that the cumulative average seems to converge toward a quite steady value, such that the averaging duration $T = 900$ seems to be sufficient for computing the other statistics. Note that the averaging duration approximately corresponds to 286 flow-through time.
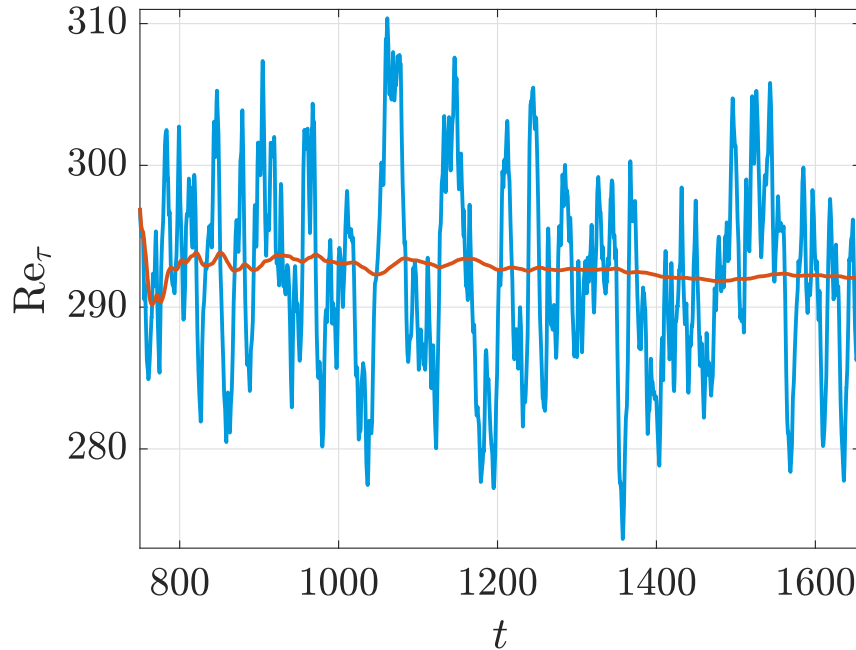

Figure 5.1.2: Evolution of the instantaneous Re_τ and its cumulative time average as a function of time between $t = 750$ and $t = 1650$.

As already explained, another way to assess the convergence of the solution is to analyze the typical variations of quantities that should vanish when considering an

---

[1]Since the wall Reynolds number and the friction velocity are directly proportional (through the Reynolds number), it is sufficient to consider only one of them.

infinite averaging window. Figure 5.1.3 shows the wall normal evolution the mean spanwise velocity. Note that both sides of the channel are shown on the same half channel. As can be seen, the spanwise mean flow fluctuates (along z) around 0 with a maximum magnitude of less than half a percent of the mean streamwise velocity. This well shows that the statistics are converged.
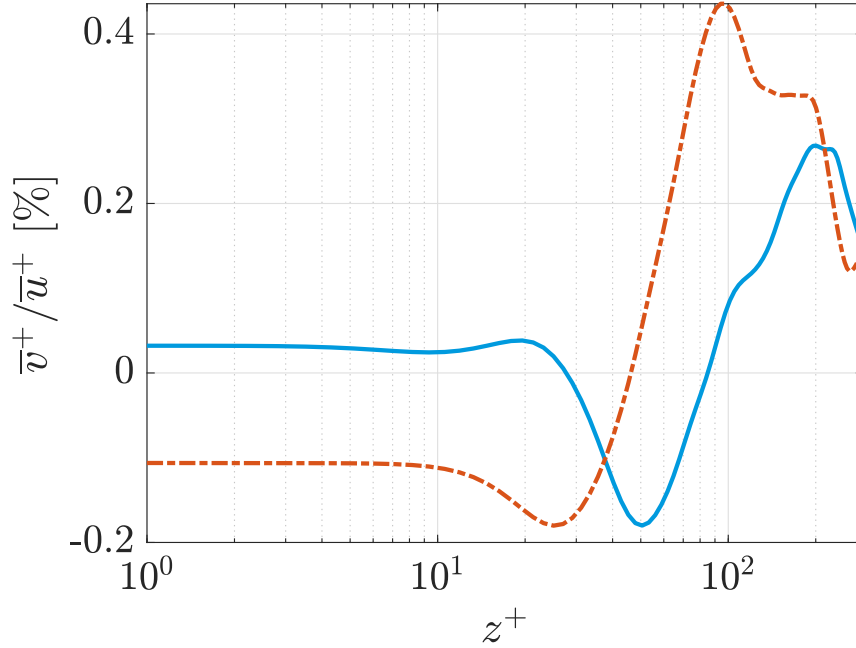

Figure 5.1.3: Mean spanwise velocity evolution in wall units relative to the mean streamwise velocity in wall units. Bottom wall, continuous curve (blue); top wall, dash-dotted curve (red).

5.1.5 Statistics verification

In order to verify the flow, the turbulence statistics are compared with the results of Dubief *et al.* [4] as the channel flow considered in this article corresponds to $\mathrm{Re}_\tau = 300$ (compared to $\mathrm{Re}_\tau = 292$ in this work).

The mean streamwise velocity profile $\overline{u}^+$ is shown in Fig. 5.1.4. The results are almost identical to the one of the article (and to the wall bounded turbulence theory) in the viscous sublayer but larger differences appear above the buffer region. The results can however still be considered as satisfactory, as the differences remain quite small. Figures 5.1.5 and 5.1.6 show the same kind of comparison for the Reynolds shear stress and the RMS of velocity fluctuations. One can also see that, again the results are quite similar with the ones obtained in the reference article. Note that for each turbulent quantity of interest the statistics of both walls are very similar, which gives again confidence in the fact that the statistics are well converged.

Small differences between the present results and the one of the article could come from several things: the wall Reynolds number of this simulation is not exactly 300, the spatial discretization of both studies are quite different (spectral decomposition here

and finite difference in the article) and the size of the domain is not exactly the same.
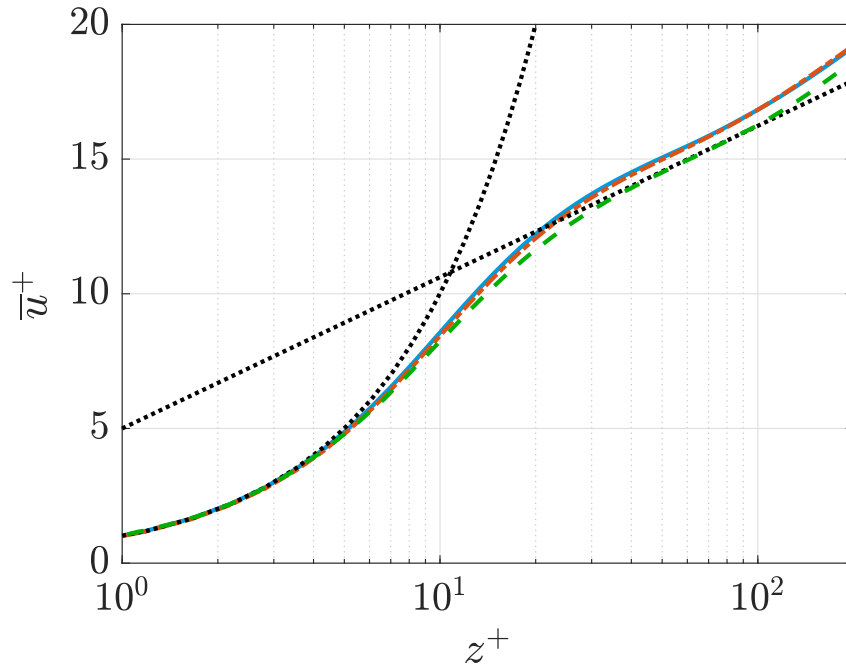

Figure 5.1.4: Logarithmic law of the wall. Comparison of the mean streamwise velocity profile in wall units with the reference article. The black dotted curves correspond to the theoretical profiles of the law of the wall (in the viscous sublayer and in the log-law region). Bottom wall, continuous curve (blue); top wall, dash-dotted curve (red); reference result, dashed curve (green).
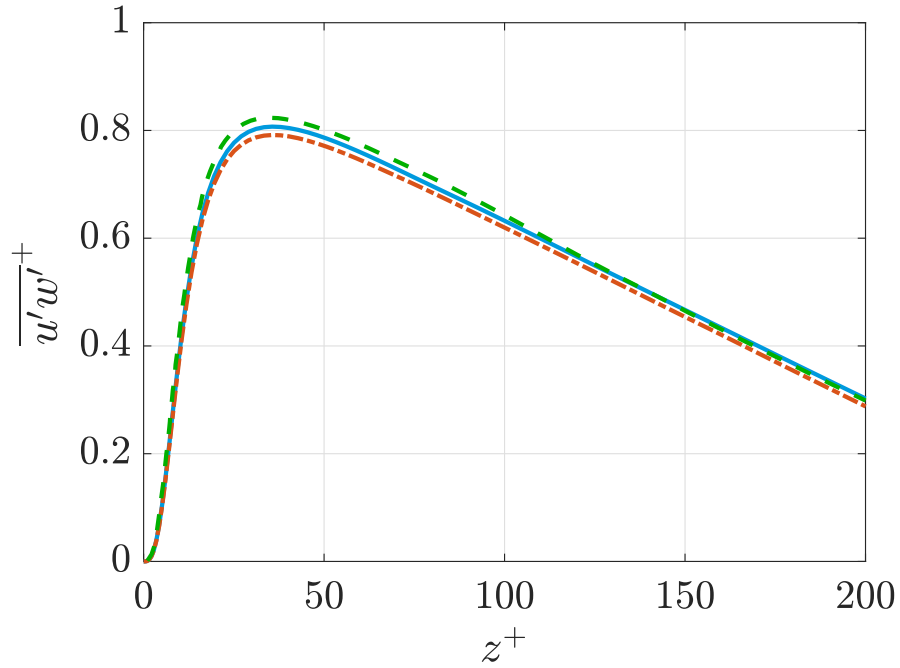
Figure 5.1.5: Comparison of the Reynolds stress profile in wall units with the literature. Bottom wall, continuous curve (blue); top wall, dash-dotted curve (red); literature result, dashed curve (green).
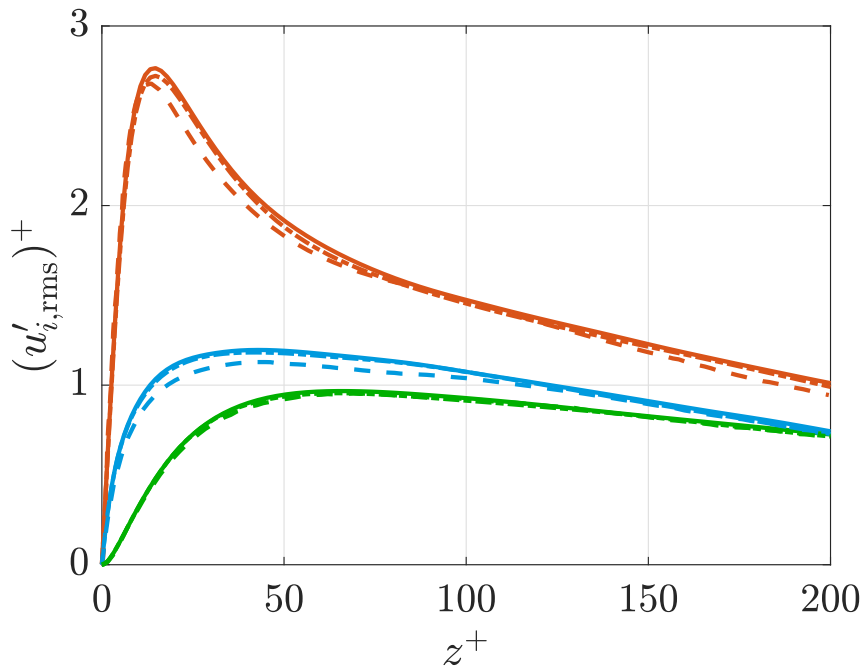

Figure 5.1.6: Comparison of the RMS velocity profiles in wall units with the literature. Bottom wall, continuous curves; top wall, dash-dotted curves; literature result, dashed curves. $(u'_{\mathrm{rms}})^+$, red; $(v'_{\mathrm{rms}})^+$, blue; $(w'_{\mathrm{rms}})^+$, green.

5.2 Particle tracking

Even if it may seem to be a straightforward process, it is useful to give some information on the way the tracking of the particles is performed in the particular context of a parallelized pseudo-spectral solver.

In order to track the position of a particle in time, the simple explicit Euler time integration method is used. In fact, at the time instant n, knowing the position of a particle, noted $\boldsymbol{x}^{(n)}$, and having a way of evaluating its velocity, noted $\boldsymbol{u}^{(n)}$, its position at the next time step will be

$$\boldsymbol{x}^{(n+1)} = \boldsymbol{x}^{(n)} + \boldsymbol{u}^{(n)} \Delta t, \tag{5.2.1}$$

where Δt is the chosen time step. In practice, the tracking is done *on the fly*, meaning that the trajectories of the particles are progressively integrated while the flow solution is computed. In this case, the time step Δt is thus the same as the Eulerian simulation. This choice (same time step and explicit Euler time integration) has been made for the sake of simplicity[2]. Finally note that since the goal is to record the history of the velocity gradients experienced by a particle, the velocity gradients tensor is also evaluated each time that the velocity of a particle is computed.

This algorithm requires to be able to have access to the flow velocity (and the velocity gradients) at any position in the domain[3]. The issue being that the velocity is commonly defined at the discrete grid points, if the particle is not exactly located at such positions, the velocity needs to be interpolated. Usually, this interpolation is done by performing a weighted average of the neighbor grid points velocities. The advantage of the spectral solver is the fact that the problem variables are numerically encoded using their spectral coefficients. This means that it is possible to analytically interpolate the velocity and its gradient at any point by considering the linear combination of the spectral modes weighted by their appropriate coefficients.

From the article of Burns *et al.* [1] about DEDALUS version 2, considering a general field f to be interpolated at the point $\boldsymbol{x} = (x, y, z)$,

$$f(x, y, z) = \sum_n \sum_{k_x} \sum_{k_y} f_{k_x, k_y, n} \phi_{k_x}(x) \phi_{k_y}(y) T_n(z), \tag{5.2.2}$$

where ϕ_{k_x} corresponds to the k_x-th Fourier mode (x-decomposition), ϕ_{k_y} corresponds to the k_y-th Fourier mode (y-decomposition) and T_n corresponds to the n-th Chebyshev mode (z-decomposition). The coefficient $f_{k_x, k_y, n}$ then corresponds to the modes ϕ_{k_x}, ϕ_{k_y} and T_n. The expressions of the different modes are

$$\begin{cases} \phi_k(x) = \exp\left(ikx\right), \\ T_n(z) = \cos\left(n \arccos\left(z\right)\right), \end{cases} \tag{5.2.3}$$

---

[2]More advanced time integration methods could be used but these are also more computationally expensive. The goal in this case was however to be able to track the position of several particles without significantly slowing the flow computation.

[3]Note that considering different time steps for the particle tracking and the flow computation would potentially require to have access to the velocity at a given point and between two time steps, which significantly increases the computation time.

where the x and y Fourier modes have the same expression. Knowing these expressions also allows to compute the gradient of f, in order to derive an analytical expression for the spatial interpolation of the gradient. Note that in practice, f represents the different velocity components (u, v and w).

This method has the advantage of being accurate, but notice that any interpolation requires to loop over the entire spectral coefficients matrix[4] in order to be *exact*. This is quite heavy in practice compared to a more classical interpolation method where the number of neighbors taken into account is quite limited. This technique possesses however another advantage since it is highly parallelizable. In fact, in DEDALUS, each processor only has access to a certain slice of the coefficient matrix. Equation 5.2.2 can then be rewritten in order to make the local sums over the spectral coefficients of each processor appear. Each processor can then compute its contribution to the global sum such that the workload is shared.

In practice, 100 particles are tracked from $t = 1650$ to $t = 1990$ and these are initially evenly distributed on a yz-plan of the channel. As an illustration, Fig. 5.2.1 shows the wall normal position of 10 particles as a function of time.
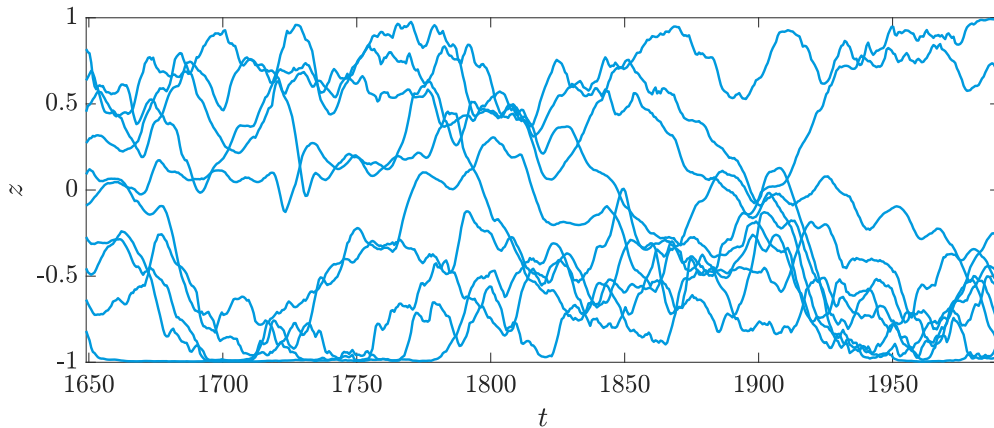

Figure 5.2.1: Evolution of the z-position of 10 particles (out of 100) as a function of time. The particles are advected by a channel flow which is described in Sec. 5.1.

5.3 Polymer response

Having access to the velocity gradient experienced by each particle, the Lagrangian equations of the polymers can be solved. One can consider the same system of equations that was used for simulating the polymer response to zero-dimensional flows (Eq. 2.3.1), where the partial time derivative is now to be understood as a Lagrangian time derivative:

$$\begin{cases} \dfrac{\mathrm{d}A_{ij}}{\mathrm{d}t} - \dot{\gamma}_{ik}A_{jk} - \dot{\gamma}_{jk}A_{ik} = \dfrac{1}{\mathrm{Wi}}\left(\delta_{ij} - \dfrac{A^{\mathrm{sp}}}{A}A_{ij}\right), \\ \dfrac{\mathrm{d}B}{\mathrm{d}t} - \dfrac{4B}{A}\dot{\gamma}_{ij}A_{ij} = \dfrac{1}{\mathrm{Wi}}\left(10A - 2B^{\mathrm{sp}}\right). \end{cases} \qquad (5.3.1)$$

---

[4]One could also consider only a fraction of the coefficient matrix and obtain an approximation of the interpolation, but this has not been done in this case.

The parameters that are chosen in this simulation are Wi = 5 and b = 3600 (these can correspond to a DR case). A natural choice for the initial conditions would be to start from equilibrium. However, the length of the simulation being quite limited compared to Weissenberg number (the simulation lasted 340 non-dimensional flow time, which corresponds to 68Wi), such initial condition makes the initial transient solution unnecessarily long. In fact, during this initial transient solution, the polymers are not already adapted to the flow and the system cannot be considered as *statistically steady*. Another better suited choice is to make the polymer start from a Newtonian one-dimensional steady channel flow solution. In that case, the initial condition of a particle depends on the shear rate which is a linear function of the initial height of the particle. Using such kind of initial condition makes the initial transient solution much shorter.

The above system is again numerically integrated using a 4th order explicit Runge-Kutta method. The time step $\Delta t = 1.25 \cdot 10^{-3}$ is chosen twice smaller that the one of the Eulerian simulation. Note also that in the Runge-Kutta algorithm, intermediary steps are performed such that the velocity gradients need to be evaluated between the different time steps. In order to do so, a linear time interpolation is performed, such that the velocity gradient at a given time is computed as a linear combination of the velocity gradient at the previous and next registered time instants.

It is however important to mention that a late error has been spotted in the implementation of the velocity gradient interpolation. In fact, some results appearing suspicious, a verification showed a significantly non-zero trace of the velocity gradients experienced by the polymers, although a divergent free velocity field was imposed in the flow equations. An in depth verification showed that the implementation of the interpolation of the velocity gradients was wrong, leading to wrong velocity gradients (even if some components are correct). By lack of time, these interpolations could unfortunately not be performed again. Having in mind that the velocity gradients experienced by the polymers can thus not be interpreted as coming from a channel flow, the polymer response is however still valid. In fact, the following results must be interpreted as a generalization of Sec. 2.3 where more general time varying velocity gradients are considered.

5.3.1 Polymer trajectories

The first comparison that can be made between the different constitutive models is to observe the time evolution of some polymer quantities by following a particle. This is of course not perfectly representative of the characteristics of the different closure approximations, but it helps visualizing how different the models can be. Note that even though the FENE-P constitutive model does not need an equation for B to compute the polymer stress, it can still be computed in order to be compared to the results of the other models. The same holds for α and β. From Sec. 2.2.3,
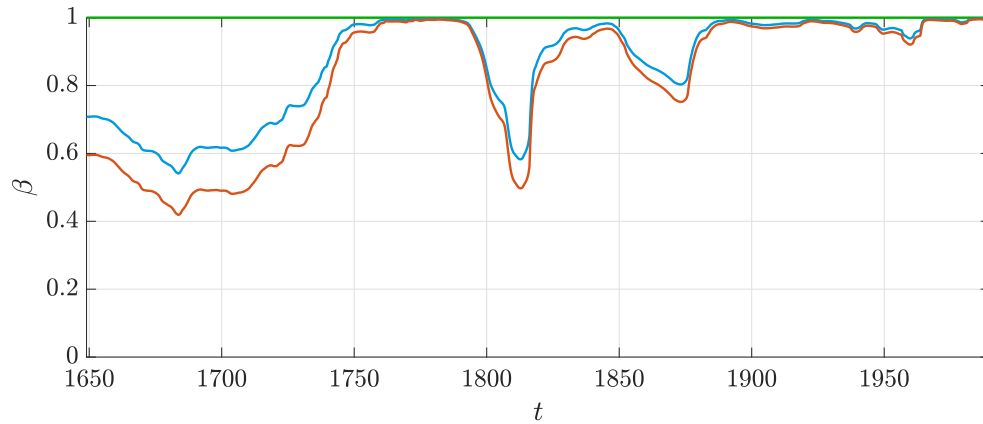
$$B = A^2, \quad \alpha^2 = A \quad \text{and} \quad \beta = 1. \tag{5.3.2}$$

(a) Mean square extension A.

(b) α.

(c) β.
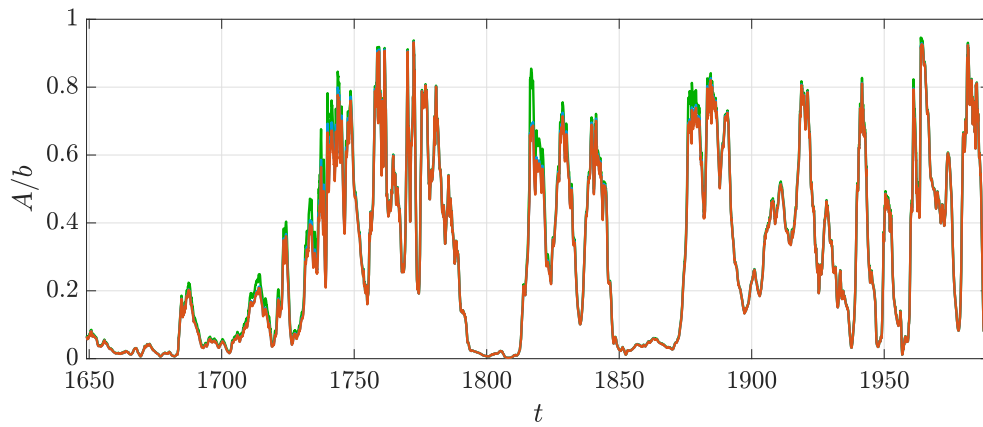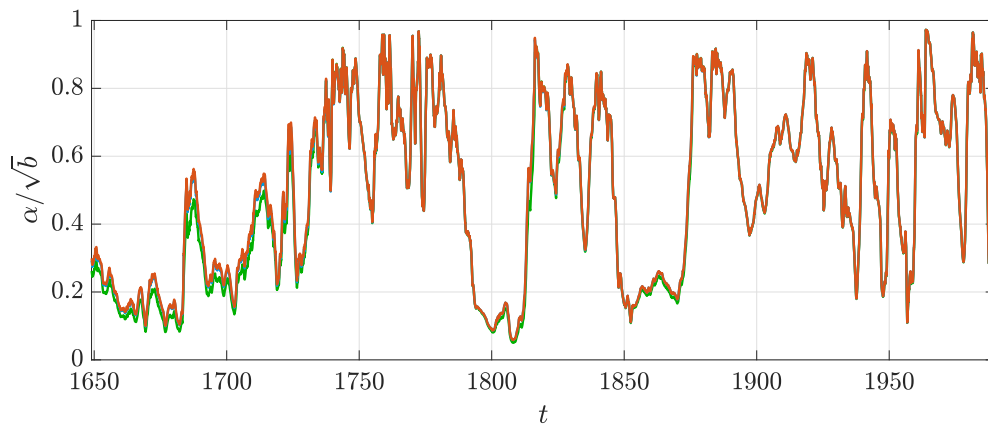
Figure 5.3.1: Time evolution of different polymer quantities related to a specific particle, being advected by the turbulent flow. Pay attention to the fact that the flow cannot be interpreted as a channel flow. FENE-L, red; FENE-LS$_0$, blue; FENE-P, green.

Figure 5.3.1 shows the time evolution of some quantities related to a specific particle. The first thing that can be seen is that the FENE-P mean square extension is generally higher that the one of the other models. One should however notice that all models

react to the flow history in a perfectly coordinated manner, such that no lag can be observed between the different responses[5] and only the amplitudes of the variations seem to differ.

Figure 5.3.1c shows the limitation of the FENE-P model in the sense that it is limited to $\beta = 1$ from the simple shape of its radial canonical distribution ρ_α^c. In fact, as can be seen by comparing Fig 5.3.1b and 5.3.1c, the differences in terms of canonical distributions mainly occur when $\beta < 1$ and these tend to behave in a similar way when $\beta \approx 1$. More precisely, a low β-parameter corresponds to the fact that the low extension polymers have a significant weight in the distribution $\rho_{\alpha,\beta}^c$, such that in order to give the same mean square extension, the FENE-P radial probability distribution should exhibits a smaller α and this is what is observed in practice.

However, the differences between the mean square extension of the different models do not seem to be only functions of the value of β as can be seen by comparing Fig. 5.3.1a and 5.3.1c. In fact, α also seems to play a role in the sense that when α is small, no significant difference can be observed for A. This can directly be explained from Eq. 2.2.2–2.2.6 as the value of A for both more advanced models decreases with decreasing β but is also directly proportional to α^2. From the expression of A for the FENE-P (Eq. 5.3.2), one understands that for small values of α, the difference of A is small (even if $\beta < 1$), but for larger values of α, β starts to play a more significant role. The largest differences of A may thus be observed for large α and small β.

As explained, this small comparison only gives insights of some more general tendencies. In order to be more rigorous, it is important to consider statistics over the different particles.

5.3.2 Correlated polymer quantities

Although not already proved, since the α-parameter can be seen as a measure of the polymers extension, it is clear that it is directly influenced by the flow. However, it is hard to gain a better comprehension of the driving phenomena in the variation of β. This represents though a fundamental difference between the FENE-P and more advanced models and it is thus interesting to understand how it can vary. As explained in Sec. 4.2.1, an interesting point is the fact that β is not directly influenced by the flow. In fact, one can generally write

$$\frac{\mathrm{d}\beta}{\mathrm{d}t} = \frac{\mathrm{d}\beta}{\mathrm{d}t}(\alpha, \beta), \tag{5.3.3}$$

where α is itself directly influenced by the velocity gradients, such that β is still indirectly linked to the flow by α.

Numerically, $\mathrm{d}\beta/\mathrm{d}t$ can be estimated using simple time finite differences. Figure 5.3.2 shows the link between $\mathrm{d}\beta/\mathrm{d}t$ and α through an histogram that has been computed over all particles and time instants with the FENE-L model (a very similar histogram have been obtained for the FENE-LS$_0$ model and is not shown). As can be seen, high positive values of $\mathrm{d}\beta/\mathrm{d}t$ are only accessible at high α and inversely, negative values of $\mathrm{d}\beta/\mathrm{d}t$

---

[5]This has been verified numerically by checking that the different maxima occur at the same time for each model.

are only accessible at low α. This can be qualitatively understood by saying that β increases when α is high and β decreases when α is low. This kind of behavior have already been encountered in Sec. 2.3 (as shown by the shape of the (α, β)-trajectory in Fig. 3.4.1b–3.4.1d) and is now generalized to more complex flows. Considering a small α-parameter (probably because the flow is weak such that the polymers are in their coiled configuration) as well as a small β-parameter, if α suddenly significantly increases, $\mathrm{d}\beta/\mathrm{d}t$ instantaneously follows α, but β takes some time to reach higher values (the typical rate of increase of β is less than 0.4 per non-dimensional flow time as can be seen in Fig. 5.3.2). In that specific case, during a small period of time, α is high while β is still relatively low. This situation thus corresponds to high differences in A between the different models (mainly between the FENE-P and the more advanced models) as explained previously. However, if α does not decreases too rapidly, β will eventually get closer to 1, such that this difference decreases again. This reasoning totally justifies why the difference between the FENE-P and the other models seems to be dictated by transient phenomena.
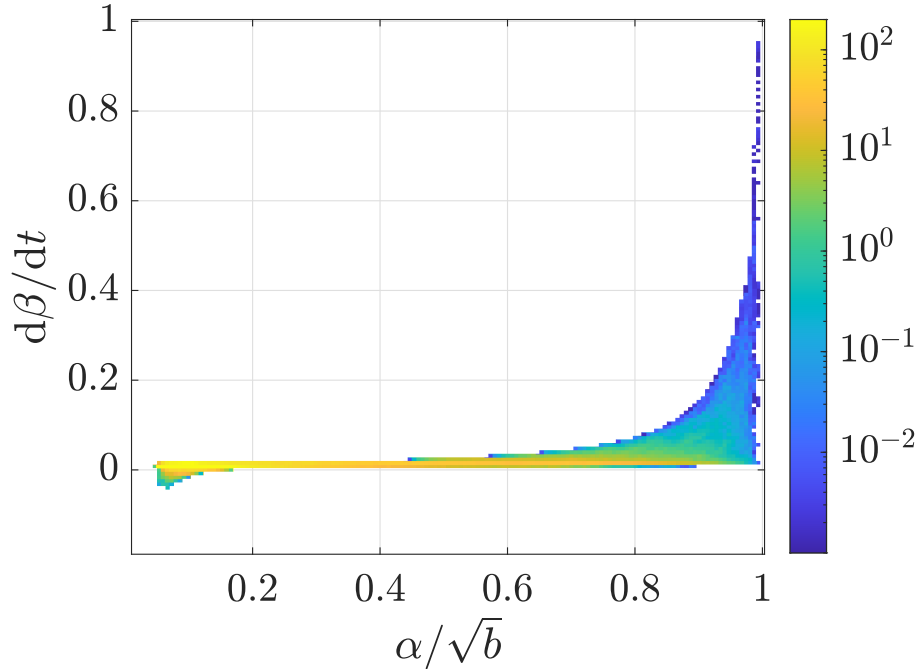

Figure 5.3.2: Histogram between α and $\mathrm{d}\beta/\mathrm{d}t$ for the FENE-L model. The number of bins along each dimension is 150. The color represents the density of samples in each bin.

In order to illustrate more precisely the mechanism that makes the FENE-P model significantly differ from the more advanced constitutive models during short periods of high dumbbells extensional rate, a small numerical experiment is set up. The goal is to isolate specific events that occur for each particle and that illustrate the present point. A low and a high threshold for α are considered: α_{L} and α_{H} respectively. The interesting events are when α has been smaller than α_{L} for a period of time larger than Δt_{L} and went then from α_{L} to α_{H} is less than Δt_{R}. Each time a particle experiences such kind of event, its polymer quantities are recorded from the time $\alpha = \alpha_{\mathrm{L}}$ until the

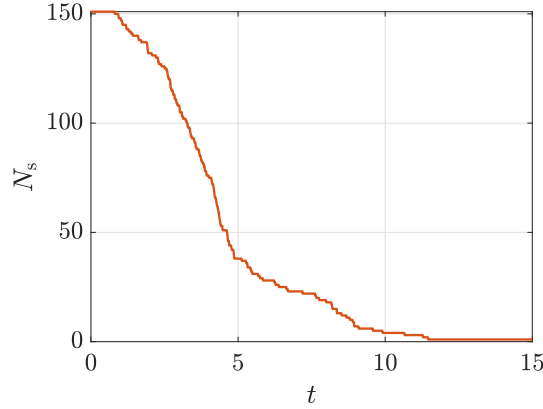time where α decreases and becomes again smaller than α_H. In this case, the different parameters were chosen as

$$\alpha_L = 0.4, \quad \alpha_H = 0.7, \quad \Delta t_L = 6 \quad \text{and} \quad \Delta t_R = 4. \tag{5.3.4}$$
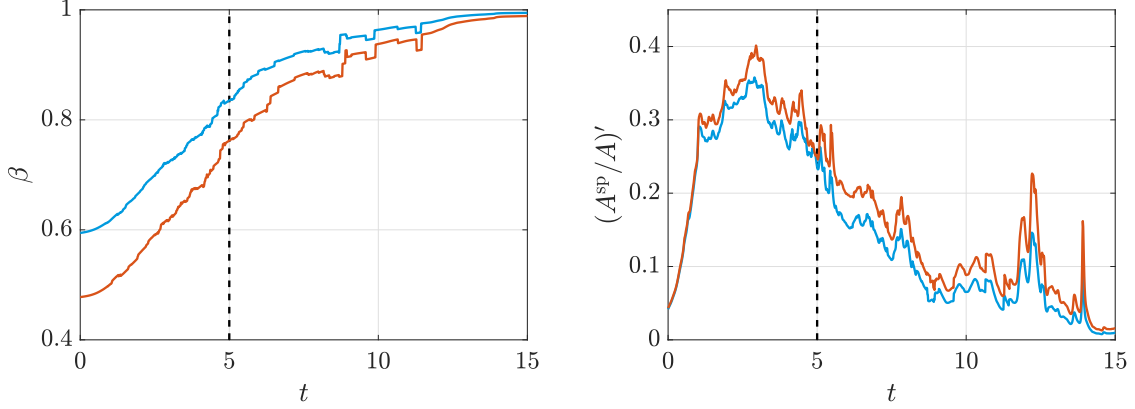
(a) β-parameter.

(b) Scalar measure of the stress $(A^{\text{sp}}/A)'$.

(c) Number of samples N_s.

Figure 5.3.3: Time evolution of the ensemble average of β and $(A^{\text{sp}}/A)'$. These ensemble averages are performed over specific events corresponding to sudden high increases of the α-parameter. The precise characteristics of such events are described in Eq. 5.3.4. Figure 5.3.3c shows the evolution of the number of samples available as a function of time. The black dashed line in Fig. 5.3.3a–5.3.3b shows the Weissenberg number. FENE-L, red; FENE-LS$_0$, blue.

During the recording times, for each time instant (starting when $\alpha = \alpha_L$ for each event), the mean of the quantities of interest are computed in order to build some kind of averaged evolution of the polymer variables. The quantities that were investigated are the β-parameter and A^{sp}/A. In fact, the latter is the scalar proportionality factor between the conformation tensor and the polymer stress tensor and it can be seen as some scalar measure of the stress. More precisely, this is the relative difference between that term and the corresponding term for the FENE-P model that is considered (the objective being to analyze the differences between the models). From Sec. 2.2.3, the

term A^{sp}/A for the FENE-P model is $(1 - A/b)^{-1}$. The relative difference then writes

$$\left(\frac{A^{\mathrm{sp}}}{A}\right)' = \left(\frac{A^{\mathrm{sp}}}{A} - \frac{1}{1 - A/b}\right)(1 - A/b) = A^{\mathrm{sp}}\frac{1 - A/b}{A} - 1. \qquad (5.3.5)$$

Figure 5.3.3 shows the results of these ensemble averaged responses. As can be seen, the number of samples is quite limited, resulting in poorly converged statistics. Error bars or standard deviations are however not shown for readability. One also understands from Fig. 5.3.3c that for the number of samples quickly decreases such that the ends of the responses have to be interpreted carefully. Nevertheless, the conclusion is still very clear as β increases toward 1 in a characteristic time of about Wi. The scalar measure of the stress reaches a peak during the rise of β (as β is still quite small but α is already high) and decreases to 0 as β gets closer to 1. Naturally, A and B also follows the same kind of tendency as in Fig. 5.3.3b and are not shown. Such really illustrate from where the differences between the FENE-P and the more complex closure approximations come.

5.3.3 Impact of the flow

Knowing that the differences between the models occur at high sudden increases of α does not explain to which typical flow event such phenomena are associated. In fact, it is interesting to try to understand when α suddenly increases. A significant limitation here is the lack of interpretation of the velocity gradients, since these are not deviatoric and cannot be considered as coming from a turbulent channel flow.

An interesting topological reasoning allows to decompose the influence of the velocity gradients on the dumbbells through the eigenvalues of the velocity gradients. This analysis is however mainly limited to deviatoric velocity gradients, which is not the case here. The influence of the velocity gradients on the stretching of the polymers can still be evaluated through the strain rate tensor $E_{ij} = (\dot{\gamma}_{ij} + \dot{\gamma}_{ji})/2$, being the symmetric part of the velocity gradients tensor. More precisely, one can build a scalar quantity representing some kind of norm of the strain rate: $|\boldsymbol{E}| = \sqrt{E_{ij}E_{ij}}$. The correlation between the rate of increase of α, $\mathrm{d}\alpha/\mathrm{d}t$ (computed using time finite differences) and the norm of $\boldsymbol{E}$ can be visualized through the use of an histogram.

As can be seen in Fig. 5.3.4, the minimum of $\mathrm{d}\alpha/\mathrm{d}t$ can be achieved for relatively small $|\boldsymbol{E}|$ and the maximum of $\mathrm{d}\alpha/\mathrm{d}t$ can be achieved for bigger $|\boldsymbol{E}|$. However, one quickly understands that such flow scalar quantity is not sufficient for explaining correctly the high dumbbells extension rate. It is however difficult to find better correlations for such general velocity gradients history.
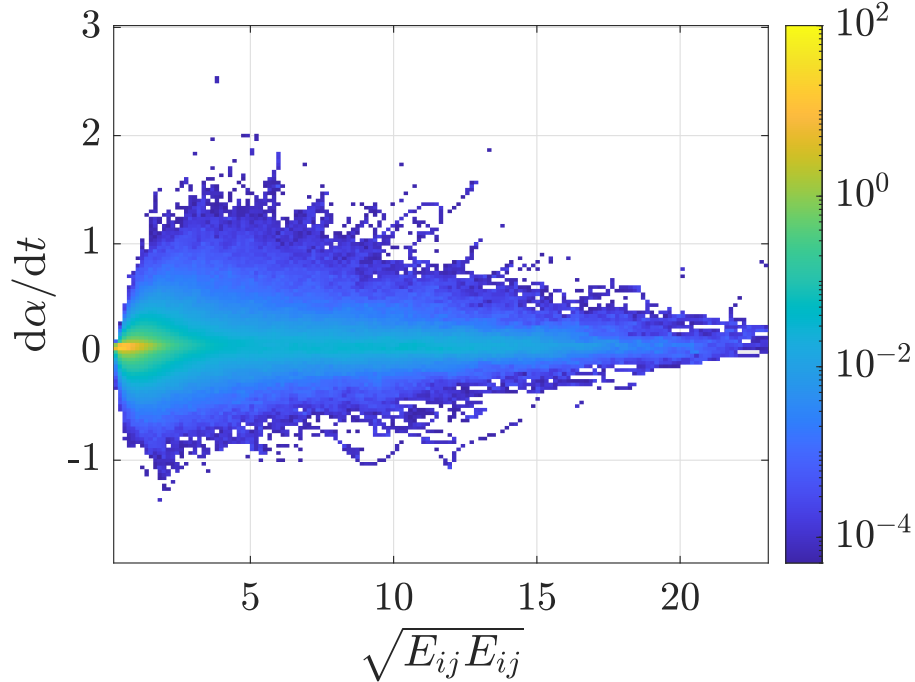
Figure 5.3.4: Histogram between $\sqrt{E_{ij}E_{ij}}$ and $\mathrm{d}\alpha/\mathrm{d}t$ for the FENE-L model. The number of bins along each dimension is 150. The color represents the density of samples in each bin.

5.3.4 Drag reduction

The drag reduction mechanism directly comes from the interaction of the polymers with the near wall coherent structures of wall bounded turbulent flows, such as high-low speed streaks, quasi-streamwise vortices and hairpin vortices. All of these structures are somewhat characterized by coherent vortices. In practice, the polymers thus play a special role in such regions and it is then interesting to seek whether differences between the FENE-P and more elaborated models arises near these structures.

As shown by Dubief and Delcayre [2], a useful and accurate vortex identification parameter is the Q-criterion. It is defined as

$$Q = \frac{1}{2}\left(\Omega_{ij}\Omega_{ij} - E_{ij}E_{ij}\right) = -\frac{1}{2}\dot{\gamma}_{ij}\dot{\gamma}_{ji}, \tag{5.3.6}$$

with $\Omega_{ij} = \frac{1}{2}\left(\dot{\gamma}_{ij} - \dot{\gamma}_{ji}\right)$ the anti-symmetric part of the velocity gradient tensor $\dot{\boldsymbol{\gamma}}$. Note that the Q criterion is the second invariant of the velocity gradient tensor. From the above expression, one understands that it can be seen as a measure of the rotation rate compared to the strain rate, so that it seems in fact to be a good vortex identification criteria.

In parallel, an interesting polymer quantity is the polymer elastic potential e_{p}. Since polymer drag reduction mainly comes from the interaction of the polymers and the near wall vortices, it seems logical that some energy is being exchanged between the flow and the polymers. As explained by Sid [9], the elastic potential energy of a Lagrangian polymer varies through energy exchanges with the kinetic energy of the flow, noted

e_k and through dissipation originating from the drag of the solvent on the dumbbells beads. The first contribution is well known and quite general, but the second one is harder to derive and generalize to more advanced closure approximations such as the FENE-L or FENE-LS$_0$. Only the first contribution is thus considered here as it is also the one that is conserved (in the hole system). The rate of energy transfer from the flow kinetic energy e_k to the polymer elastic potential energy e_p is expressed as

$$P_{k,p} \propto \tau_{ij}^p S_{ij}. \tag{5.3.7}$$

In practice, this term should be multiplied by a factor depending on the concentration parameter ε. The system being however one-way coupled in this case (by construction), only the varying term is considered.

The goal is then to compare the correlation of Q and the above rate of energy transfer $P_{k,p}$ for each model. If significant differences occur between the results of the FENE-P and the other more advanced models, it is likely that such models could be more accurate (or at least bring differences) for simulating polymer drag reduction. However, as already explained several times, one cannot generally interpret the present velocity gradients as coming from a channel flow. It is thus not possible in practice to analyze the polymer response near turbulent coherent structures of a channel flow. The correlation between Q and $P_{k,p}$ is thus not studied here.

However, it is still interesting to understand how can $P_{k,p}$ be correlated to polymer quantities. Figure 5.3.5 shows the correlation between $P_{k,p}$ and $d\alpha/dt$ again by the mean of an histogram. As can be seen, negative values of $P_{k,p}$ exclusively yields negative values of $d\alpha/dt$. The correlation is less strong for positive values of $P_{k,p}$, but one notices that the peak of $d\alpha/dt$ is associated to positive values of $P_{k,p}$. The sudden increases of α are thus linked to energy transfers from the flow to the polymers (as was expected) and since the main differences between the models mainly occurs during such events, it is likely that the use of the FENE-L or FENE-LS$_0$ models for simulating DR could yield different results than the ones that can be obtained with the simpler FENE-P model.
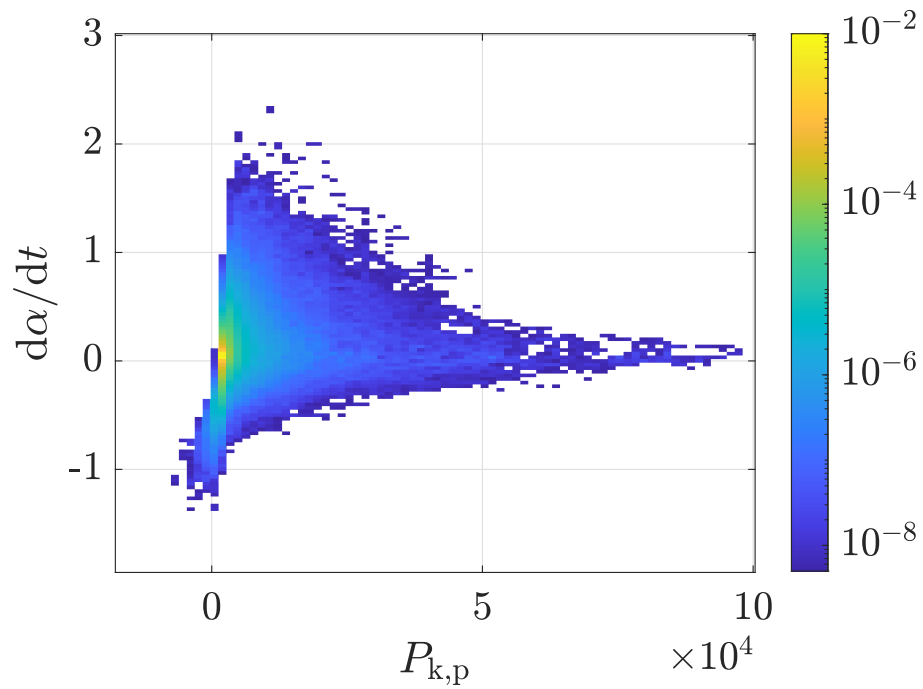
Figure 5.3.5: Histogram between $P_{\mathrm{k,p}}$ and $\mathrm{d}\alpha/\mathrm{d}t$ for the FENE-L model. The number of bins along each dimension is 150. The color represents the density of samples in each bin.

Conclusion

A detailed analysis permitted to show that the FENE-LS model proposed by Lielens *et al.* [7] (called FENE-LS$_1$ here) is not appropriate as the model equations can make the system leave its admissible domain. However, a modified more rigorous version of the FENE-LS (called FENE-LS$_0$ here) has shown consistent results and appears to be a good alternative to the FENE-LS. Moreover, it has been shown that the original expression of the FENE-L model [6, 7] presents a suspected error that has a profound impact on the model behavior. In fact, the corrected model appears to be self-consistent (as the FENE-LS$_0$) in the sense that its equations cannot make the system leave its admissible space.

Small verification and simple flow cases helped understanding the general behavior of the different models considered. It illustrated once again the similarity between the different closure approximations at steady state and for high extensions. A better investigation of the canonical radial probability density distribution $\rho^c_{\alpha,\beta}$ helped to better understand the system physically, mainly through the (α, β)-space representation.

Although the opposite effect is usually observed, the addition of artificial center-of-mass diffusion appeared to bring complexity in this case. In fact, although rigorous for a general FENE distribution, spatial diffusion can make a canonical distribution leave its restricted admissible space, resulting in unwanted effects. In order be able to tolerate significant amounts of diffusion (although not representative of the reality), a modified diffusion technique has been suggested, but has not already been tested in practice.

Being not able to run a full coupled Eulerian simulation with the more advanced models, the impact of the turbulence on the different polymer models was analyzed by imposing the velocity gradients experienced by tracked particles from an Eulerian Newtonian turbulent channel flow in the polymers equations. An error has however lately been spotted in the interpolation of the velocity gradient, making the interpretation of the results as the polymer response to a turbulent channel flow inaccurate. The computed polymer response could nevertheless be interpreted as the one of a general and unknown flow and still permitted to gain a better comprehension of the differences between the FENE-P and the more advanced models. More concretely, it has been shown that the FENE-P yielded different result each time that the dumbbells were suddenly submitted to a large stretching after a significantly long time of being in a lower extension configuration. Such differences could have an impact on the simulation results of turbulent flows such as DR or MDR.

Acknowledgments

I would truly like to thank Professor Vincent E. Terrapon, my advisor, for his great help during the advancement of this work. He spent a considerable amount of time, trying to help me to understand the results, discussing what were the best options and answering loads of questions. It was a pleasure to see my advisor being as enthusiastic as me when making progress but he also supported me a lot when the results were not convincing and that radically different approaches needed to be used, which can sometimes be demoralizing.

I would also like to thank Dr Yves Dubief for his help through the different numerical codes that helped me to understand the functioning of DEDALUS.

Finally, I would like to thank my family, my friends and my girlfriend that expressed their support for the accomplishment of this work.

Appendix A

Polymer time scale non-dimensionalization

Considering a polymer time scale rather than a flow time scale for non dimensionalizing the equations yields

$$t = \frac{\hat{t}}{\lambda^{\mathrm{p}}} \quad \Rightarrow \quad \frac{\partial}{\partial \hat{t}} = \frac{1}{\lambda^{\mathrm{p}}} \frac{\partial}{\partial t} \tag{A.0.1}$$

and

$$\hat{\dot{\gamma}}_{ij} = \frac{1}{\lambda^{\mathrm{p}}} \dot{\gamma}_{ij}, \tag{A.0.2}$$

width λ^{p} a polymer characteristic time scale. Rearranging the terms, the Fokker-Planck equation (Eq. 1.2.17) then becomes

$$\frac{\partial \psi}{\partial t} + \frac{\lambda^{\mathrm{p}} \mathcal{U}}{\mathcal{L}} u_k \frac{\partial \psi}{\partial x_k} + \frac{\partial}{\partial Q_i} \left(\dot{\gamma}_{ij} Q_j \psi \right) - \frac{d \lambda^{\mathrm{p}}}{\mathcal{L}^2} \frac{\partial^2 \psi}{\partial x_k \partial x_k} - \frac{D \lambda^{\mathrm{p}}}{\mathcal{Q}^2} \frac{\partial^2 \psi}{\partial Q_k \partial Q_k} - \frac{\lambda^{\mathrm{p}}}{2 \lambda_{\mathrm{H}}} \frac{\partial}{\partial Q_i} \left(\mathcal{H}(Q) Q_i \psi \right) = 0, \tag{A.0.3}$$

where the last term naturally suggests the Rouse relaxation time as the polymer time scale. Notice the apparition of the Weissenberg number in front of the advective term as $\mathrm{Wi} = \lambda^{\mathrm{p}} \mathcal{U}/\mathcal{L}$. Considering $\lambda^{\mathrm{p}} = \lambda_{\mathrm{H}}$ and from the expression of the Peclet number ($\mathrm{Pe} = \mathcal{U}\mathcal{L}/\lambda^{\mathrm{p}}$), the following transformation holds:

$$\frac{d \lambda^{\mathrm{p}}}{\mathcal{L}^2} = \frac{d}{\mathcal{U}\mathcal{L}} \frac{\lambda^{\mathrm{p}} \mathcal{U}}{\mathcal{L}} = \frac{\mathrm{Wi}}{\mathrm{Pe}}. \tag{A.0.4}$$

Using Eq. 1.2.11,

$$\frac{D \lambda^{\mathrm{p}}}{\mathcal{Q}^2} = \frac{k_{\mathrm{B}} T}{2 H \mathcal{Q}^2} \tag{A.0.5}$$

and considering the same expression of the polymer length scale as before:

$$\mathcal{Q}^2 = \frac{k_{\mathrm{B}} T}{H} = \frac{\langle \hat{Q}^2 \rangle_0}{3}, \tag{A.0.6}$$

the above expressions become

$$\frac{D \lambda^{\mathrm{p}}}{\mathcal{Q}^2} = \frac{1}{2}. \tag{A.0.7}$$

The Fokker-Planck equation non-dimensionalized with the polymer time scale thus writes

$$\frac{\partial\psi}{\partial t}+\text{Wi}\,u_k\frac{\partial\psi}{\partial x_k}+\frac{\partial}{\partial Q_i}\left(\dot{\gamma}_{ij}Q_j\psi\right)-\frac{\text{Wi}}{\text{Pe}}\frac{\partial^2\psi}{\partial x_k\partial x_k}-\frac{1}{2}\frac{\partial^2\psi}{\partial Q_k\partial Q_k}-\frac{1}{2}\frac{\partial}{\partial Q_i}\left(\mathcal{H}(Q)Q_i\psi\right)=0 \quad\text{(A.0.8)}$$

which is the form used in the work of Lielens *et al.* [7] where the total derivative is written explicitly and the diffusive term is considered.

In order to compare results coming from the two different kind of non-dimensionalization, it is interesting to be able make the link between these two. This link is constituted by the Weissenberg number as it represents the ratio between the polymer and the flow time scale: $\text{Wi} = \lambda^{\text{p}}/\lambda^{\text{f}}$.

Denoting $(\cdot)_{\text{p}}$ and $(\cdot)_{\text{f}}$ as quantities non-dimensionalized by the polymer or flow characteristic time respectively, the following holds:

$$\begin{cases} t_{\text{f}} = \dfrac{\hat{t}}{\lambda^{\text{f}}} = \dfrac{\hat{t}}{\lambda^{\text{p}}}\dfrac{\lambda^{\text{p}}}{\lambda^{\text{f}}} = t_{\text{p}}\text{Wi}, \\[3mm] \dot{\gamma}_{\text{f}} = \lambda^{\text{f}}\hat{\dot{\gamma}} = \lambda^{\text{p}}\hat{\dot{\gamma}}\dfrac{\lambda^{\text{f}}}{\lambda^{\text{p}}} = \dfrac{\dot{\gamma}_{\text{p}}}{\text{Wi}}. \end{cases} \quad\text{(A.0.9)}$$

Appendix B

Differences with the closure expressions of the reference article

In order to compute A^{sp} and B^{sp}, the following definite integrals have to be computed

$$
\begin{cases}
A^{\text{sp}} = \beta \int_0^{\sqrt{b}} \frac{Q^2}{1 - Q^2/b} \delta_\alpha(Q) \mathrm{d}Q + \frac{1-\beta}{\alpha} \int_0^{\alpha} \frac{Q^2}{1 - Q^2/b} \mathrm{d}Q, \\
B^{\text{sp}} = \beta \int_0^{\sqrt{b}} \frac{Q^4}{1 - Q^2/b} \delta_\alpha(Q) \mathrm{d}Q + \frac{1-\beta}{\alpha} \int_0^{\alpha} \frac{Q^4}{1 - Q^2/b} \mathrm{d}Q.
\end{cases}
\tag{B.0.1}
$$

The integrals that involves the Dirac distribution are straightforward to compute but the others are not so trivial. One can however check that the expressions

$$
\begin{cases}
\int_0^{Q} \frac{\tilde{Q}^2}{1 - \tilde{Q}^2/b} \mathrm{d}\tilde{Q} = \frac{b^{3/2}}{2} \ln\left(\frac{\sqrt{b} + Q}{\sqrt{b} - Q} \right) - bQ, \\
\int_0^{Q} \frac{\tilde{Q}^4}{1 - \tilde{Q}^2/b} \mathrm{d}\tilde{Q} = \frac{b^{5/2}}{2} \ln\left(\frac{\sqrt{b} + Q}{\sqrt{b} - Q} \right) - b^2 Q - \frac{Q^3 b}{3},
\end{cases}
\tag{B.0.2}
$$

are correct by differentiating the right-hand sides. Evaluating then these at $Q = \alpha$ and injecting them in the above expression yields the closure expressions that were exposed in this work:

$$
\begin{cases}
A^{\text{sp}} \approx \frac{\beta \alpha^2}{1 - \alpha^2/b} + (1 - \beta) b \left(\frac{\sqrt{b}}{2\alpha} \ln\left(\frac{\sqrt{b} + \alpha}{\sqrt{b} - \alpha} \right) - 1 \right), \\
B^{\text{sp}} \approx \frac{\beta \alpha^4}{1 - \alpha^2/b} + (1 - \beta) b^2 \left(\frac{\sqrt{b}}{2\alpha} \ln\left(\frac{\sqrt{b} + \alpha}{\sqrt{b} - \alpha} \right) - 1 - \frac{\alpha^2}{3b} \right).
\end{cases}
\tag{B.0.3}
$$

In both articles of Lielens, deriving the FENE-L closure approximation in a one-dimensional [6] or three-dimensional [7] space, the closure expression found for A^{sp} and B^{sp} seem however to differ as they are expressed as

$$
\begin{cases}
A^{\text{sp}} \approx \frac{\beta \alpha^2}{1 - \alpha^2/b} + (1 - \beta) b \left(\frac{\sqrt{b}}{\alpha} \ln\left(\frac{\sqrt{b} + \alpha}{\sqrt{b} - \alpha} \right) - 1 \right), \\
B^{\text{sp}} \approx \frac{\beta \alpha^4}{1 - \alpha^2/b} + (1 - \beta) b^2 \left(\frac{\sqrt{b}}{\alpha} \ln\left(\frac{\sqrt{b} + \alpha}{\sqrt{b} - \alpha} \right) - 1 - \frac{\alpha}{3\sqrt{b}} \right).
\end{cases}
\tag{B.0.4}
$$

Notice that factor 2 difference before the natural logarithm and the difference with the last term of B^{sp}. Note also that for the developments in the one-dimensional space [6], the expression of A^{sp} should be multiplied by 2 and the expression of B^{sp} should be multiplied by 4, but this does not change the observed problem.

Appendix C

Boundaries in the (A, B)-space

Below are listed the expression of the boundaries of the different models as graphically represented in Fig. 3.1.2:

$$
\text{FENE-L} \quad
\begin{cases}
\mathrm{b}_1 \equiv B = \dfrac{9A^2}{5}, & A \in [0, b/3], \\[2mm]
\mathrm{b}_2 \equiv B = \dfrac{b^2}{5}\left(6\dfrac{A}{b} - 1\right), & A \in [b/3, b], \\[2mm]
\mathrm{b}_3 \equiv B = A^2, & A \in [0, b], \\[2mm]
\mathrm{b}_4 \equiv B = 0, & A = 0,
\end{cases}
$$

$$
\text{FENE-LS}_0 \quad
\begin{cases}
\mathrm{b}_1 \equiv B = A^2, & A \in [0, b/R^2], \\[2mm]
\mathrm{b}_2 \equiv B = \dfrac{b^2}{R^2}\left((R^2 + 1)\dfrac{A}{b} - 1\right), & A \in [b/R^2, b], \\[2mm]
\mathrm{b}_3 \equiv B = A^2, & A \in [0, b], \\[2mm]
\mathrm{b}_4 \equiv B = 0, & A = 0, \\[2mm]
\mathrm{b}_\star \equiv B = \dfrac{(R^2 + 1)^2}{4R^2} A^2, & A \in [0, 2b/(R^2 + 1)],
\end{cases}
\qquad \text{(C.0.1)}
$$

$$
\text{FENE-LS}_1 \quad
\begin{cases}
\mathrm{b}_1 \equiv B = \dfrac{R^2 + 1}{2} A^2, & A \in [0, b/R^2], \\[2mm]
\mathrm{b}_2 \equiv B = \dfrac{R^2 + 1}{1 + \frac{A}{b}R^2} A^2, & A \in [b/R^2, b], \\[2mm]
\mathrm{b}_3 \equiv B = A^2, & A \in [0, b], \\[2mm]
\mathrm{b}_4 \equiv B = 0, & A = 0.
\end{cases}
$$

Bibliography

[1] Keaton J Burns, Geoffrey M Vasil, Jeffrey S Oishi, Daniel Lecoanet, and Benjamin P Brown. DEDALUS: A flexible framework for numerical simulations with spectral methods. *Physical Review Research*, 2(2):023068, 2020.

[2] Yves Dubief and Franck Delcayre. On coherent-vortex identification in turbulence. *Journal of turbulence*, 1(1):011, 2000.

[3] Yves Dubief, Vincent E Terrapon, and Julio Soria. On the mechanism of elasto-inertial turbulence. *Physics of Fluids*, 25(11):110817, 2013.

[4] Yves Dubief, Vincent E Terrapon, Christopher M White, Eric SG Shaqfeh, Parviz Moin, and Sanjiva K Lele. New answers on the interaction between polymers and vortices in turbulent flows. *Flow, turbulence and combustion*, 74:311–329, 2005.

[5] Roland Keunings. On the Peterlin approximation for finitely extensible dumbbells. *Journal of non-newtonian fluid mechanics*, 68(1):85–100, 1997.

[6] Gregory Lielens, Pierre Halin, Ingrid Jaumain, Roland Keunings, and Vincent Legat. New closure approximations for the kinetic theory of finitely extensible dumbbells. *Journal of non-newtonian fluid mechanics*, 76(1-3):249–279, 1998.

[7] Gregory Lielens, Roland Keunings, and Vincent Legat. The FENE-L and FENE-LS closure approximations to the kinetic theory of finitely extensible dumbbells. *Journal of non-newtonian fluid mechanics*, 87(2-3):179–196, 1999.

[8] Hans Christian Öttinger. A model of dilute polymer solutions with hydrodynamic interaction and finite extensibility. I. basic equations and series expansions. *Journal of non-newtonian fluid mechanics*, 26(2):207–246, 1987.

[9] Samir Sid. *Numerical Investigation of Multi-physics Turbulent Flows involving Weakly Diffusive Quantities*. PhD thesis, ULiège-Université de Liège [Gembloux Agro-Bio Tech], Liège, Belgium, 2022.